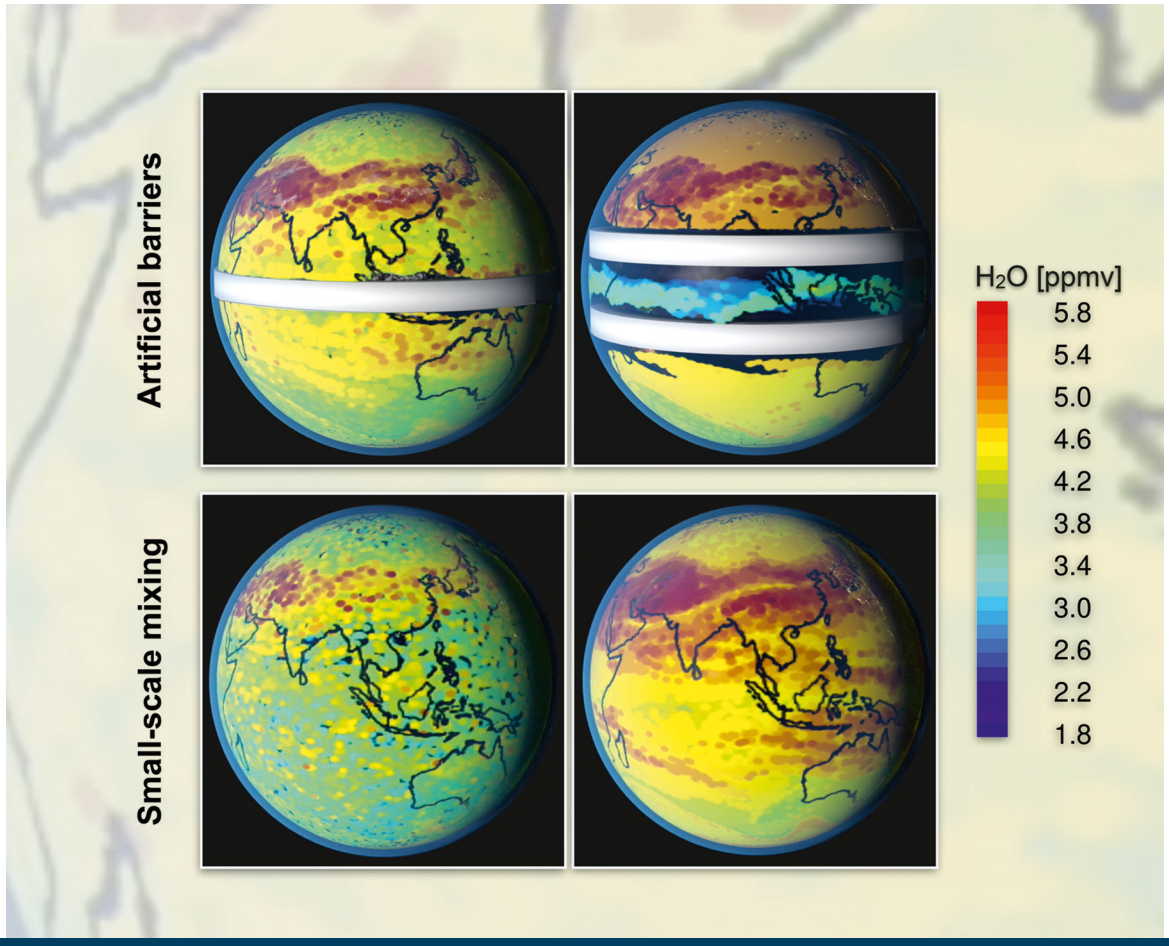

Lagrangian Simulation of Stratospheric Water Vapour: Impact of Large-Scale Circulation and Small-Scale Transport Processes

Liubov Poshyvailo

Energie & Umwelt / Energy & Environment
Band / Volume 503
ISBN 978-3-95806-488-1

Mitglied der Helmholtz-Gemeinschaft

JÜLICH
Forschungszentrum

BERGISCHE UNIVERSITÄT WUPPERTAL

JÜLICH Forschungszentrum

Lagrangian Simulation of Stratospheric Water Vapour: Impact of Large-Scale Circulation and Small-Scale Transport Processes

Dissertation

zur Erlangung des Grades
Doktor der Naturwissenschaften (Dr. rer. nat.) im Fach Physik

vorgelegt der

Bergischen Universität Wuppertal
Fakultät für Mathematik und Naturwissenschaften
Institut für Atmosphären- und Umweltforschung

von

Liubov Poshyvailo

Wuppertal, 11. Februar 2020

The PhD thesis can be quoted as follows:

urn:nbn:de:hbz:468-20200907-104252-6
[http://nbn-resolving.de/urn/resolver.pl?urn=urn%3Anbn%3Ade%3Ahbz%3A468-20200907-104252-6]

DOI: 10.25926/9mcs-tm42
[https://doi.org/10.25926/9mcs-tm42

Forschungszentrum Jülich GmbH
Institut für Energie- und Klimaforschung
Stratosphäre (IEK-7)

Lagrangian Simulation of Stratospheric Water Vapour: Impact of Large-Scale Circulation and Small-Scale Transport Processes

Liubov Poshyvailo

Schriften des Forschungszentrums Jülich
Reihe Energie & Umwelt / Energy & Environment Band / Volume 503

ISSN 1866-1793 ISBN 978-3-95806-488-1

Bibliografische Information der Deutschen Nationalbibliothek.
Die Deutsche Nationalbibliothek verzeichnet diese Publikation in der
Deutschen Nationalbibliografie; detaillierte Bibliografische Daten
sind im Internet über http://dnb.d-nb.de abrufbar.

Herausgeber und Vertrieb:	Forschungszentrum Jülich GmbH Zentralbibliothek, Verlag 52425 Jülich Tel.: +49 2461 61-5368 Fax: +49 2461 61-6103 zb-publikation@fz-juelich.de www.fz-juelich.de/zb
Umschlaggestaltung:	Grafische Medien, Forschungszentrum Jülich GmbH
Druck:	Grafische Medien, Forschungszentrum Jülich GmbH
Copyright:	Forschungszentrum Jülich 2020

Schriften des Forschungszentrums Jülich
Reihe Energie & Umwelt / Energy & Environment, Band / Volume 503

D 468 (Diss. Wuppertal, Univ., 2020)

ISSN 1866-1793
ISBN 978-3-95806-488-1

Vollständig frei verfügbar über das Publikationsportal des Forschungszentrums Jülich (JuSER)
unter www.fz-juelich.de/zb/openaccess.

Abstract

The atmospheric global circulation, also referred to as the Brewer-Dobson circulation, controls the composition of the upper troposphere and lower stratosphere (UTLS). The UTLS trace gas composition, in turn, crucially affects climate. In particular, UTLS water vapour (H_2O) plays a significant role in the global radiation budget. Therefore, a realistic representation of H_2O and Brewer-Dobson circulation, is critical for accurate model predictions of future climate and circulation changes.

This thesis is structured in two main parts: focussing on the (i) effect of model uncertainties (due to tropical tropopause temperature, horizontal transport and small-scale mixing) on stratospheric H_2O, and on the (ii) uncertainties in estimating Brewer-Dobson circulation trends from the observed H_2O trends.

The results presented here are based largely on stratospheric H_2O studies with the Chemical Lagrangian Model of the Stratosphere (CLaMS). Firstly, to investigate the robustness of simulated H_2O with respect to different meteorological datasets, we examine CLaMS driven by the ERA-Interim reanalysis from the European Centre of Medium-Range Weather Forecasts, and the Japanese 55-year Reanalysis (JRA-55). Secondly, to assess the effects of horizontal transport, we carry out CLaMS simulations, with transport barriers, along latitude circles: at the equator, at 15° N/S and at 35° N/S. To investigate the sensitivity of simulated H_2O regarding small-scale atmospheric mixing, we vary the strength of parametrized small-scale mixing in CLaMS. Finally, to assess the reliability of estimated long-term Brewer-Dobson circulation changes from stratospheric H_2O, we apply different methods of calculating mean age of air trends involving two approximations: instantaneous entry mixing ratio propagation, and a constant correlation between mean age of air and the fractional release factor of methane. The latter assumption essentially means assuming a constant correlation between the mean age of air and the mixing ratio of long-lived trace gases.

The results of this thesis show significant differences in simulated stratospheric H_2O (about 0.5 ppmv) due to uncertainties in the tropical tropopause temperatures between the two reanalysis datasets, JRA-55 and ERA-Interim. The JRA-55 based simulation is significantly moister, when compared to ERA-Interim, due to a warmer tropical tropopause of approximately 2 K. Moreover, through introducing artificial transport barriers in CLaMS, we suppress certain horizontal transport pathways. These transport experiments demonstrate that the Northern Hemisphere subtropics have a strong moistening effect on global stratospheric H_2O. Interhemispheric exchange shows only a very weak effect on stratospheric H_2O. Small-scale mixing mainly increases troposphere-stratosphere exchange, causing an enhancement of stratospheric H_2O, particularly, along the subtropical jets in the summer hemisphere and in the Northern hemispheric monsoon regions. In particular, the Asian and American monsoon systems, during boreal summer, turn out as regions especially sensitive to changes in small-scale mixing.

The estimated mean age of air trends from stratospheric H_2O changes, in general, are strongly determined by the assumed approximations. Depending on the investigated region of the stratosphere, and the considered period, the error of estimated mean age of air trends can be large. Interestingly, depending on the period, the effects from both approximations can also be opposite, and may even cancel out.

The results of this thesis provide new insights into the leading processes that control stratospheric H_2O and its trends, and are therefore relevant for improving climate model predictions. Furthermore, the results of this work can be used for evaluating the uncertainties of estimated stratospheric circulation changes from global satellite measurements.

Acknowledgements

First of all, I want to thank Prof. Dr. Martin Riese, P.D. Dr. Rolf Müller and Prof. Dr. Felix Plöger for offering me the opportunity to work on my Ph.D. thesis at IEK-7, Forschungszentrum Jülich. Many thanks to Prof. Dr. Michael Volk from Bergische Universität Wuppertal, who agreed to be my Doctoral Advisor. Without the trust and support from all of you, the completion of this thesis would not be possible. I am also very thankful to every person listed below: a whole lot of my current knowledge and experience came from all of you; thank you for the invested time and effort!

In particular, I am thankful to Prof. Dr. Felix Plöger, who was my scientific advisor during the Ph.D. It was a new challenge for me – studying the new topic after my M.Sc., as well as for him – having me as his first Ph.D. supervisee. As result, due to common effort, great work has been produced; it was a pleasure for me to work with Prof. Dr. Felix Plöger and to learn from his experience. I am also very grateful to my Ph.D. supervisor, P.D. Dr. Rolf Müller, for amazing support and useful advices, both in my scientific and personal questions. It seemed for me that he always had solution for even the most complex situations. Besides, thanks to P.D. Dr. Rolf Müller for the inspiring scientific discussions.

In addition, thanks to Dr. Gebhard Günther and Nicole Thomas for support in technical questions during my work with CLaMS. A special gratitude goes to Jülich Supercomputing Center (JSC) for the possibility to perform simulation on the supercomputer JURECA under the VSR project ID JICG11; especially, to the JSC support team, in particular, Dr. Alexandre Strube (JSC) and Dr. Jens-Uwe Grooß (IEK-7). Also, thanks to Prof. Dr. Felix Plöger, P.D. Dr. Rolf Müller, and Dr. Alexandre Strube for proofreading this thesis.

This work has been made possible with the following funding: the German Ministry of Education and Research under grant no. 01LG1222A (ROMIC-TRIP), and the Helmholtz Young Investigators Group A-SPECi ("Assessment of stratospheric processes and their effects on climate variability").

I am also very thankful to P.D. Dr. Paul Konopka, Dr. Johannes Laube, Dr. Jens-Uwe Grooß, Dr. Mengchu Tao, and Dr. Aurelien Podglajen for fruitful scientific discussions. Moreover, thanks to P.D. Dr. Paul Konopka for interesting talks about Ukrainian culture; it always gave me very warm feelings about my own country. Further, I am thankful to the whole team of IEK-7 with its leader Prof. Dr. Martin Riese. It was a pleasure to interact with all of you, to share lunches and relaxing coffee breaks. A special place in this list goes to Dr. Xiaolu Yan – the best office mate I have ever had until now, and even more: she became my good friend.

Here, I want to thank HITEC Helmholtz Graduate School HITEC graduate school. I am glad to have been part of it throughout my Ph.D. Many of the courses and training proposed by HITEC have been very useful for my career. Moreover, I got the opportunity to participate in the "HITEC Go" program, which gave me the unforgettable experience of working together with my external mentor, Prof. Dr. Stephan Fueglistaler, from Princeton University (Department of Geosciences). I am very grateful to Prof. Dr. Stephan Fueglistaler for sharing part of his experience with me, and for being, and remaining to be, my scientific motivator and coach. Special thanks goes to Dr. William Randel from the Atmospheric Chemistry Observations and Modeling Lab at National Center for Atmospheric Research (NCAR), who is very well known atmospheric scientist, and with whom I met just at the beginning of my Ph.D.: thank you for

your advice and encouragement! For the additional motivation and great help in defining the future steps of my career, I am grateful to Andrea Bosten (career consultant and couch at the Career Center of Forschungszentrum Jülich) and Orest Shupeniuk (speaker-psychologist and media expert).

My Ph.D. stay in Jülich would not have been possible without my M.Sc. supervisor; I am thankful to Dr. Svyatoslav Kondrat, who gave me the opportunity to write my Master thesis in IBG-1 (Forschungszentrum Jülich), and introduced me to Jülich, to German culture and to the international scientific community. I am also very grateful to my Alma Mater National University of "Kyiv-Mohyla Academy", which supported my idea of writing my M.Sc. thesis abroad; that had a definite impact on my scientific career. Additionally, I am thankful to my B.Sc. supervisor, Dr. Volodymyr Korolovych, who had shown me the Harvard University and the Massachusetts Institute of Technology complimentary to the main part of the "HITEC Go" program.

I want to thank as well the European Geosciences Union, giving me the possibility to participate in their General Assemblies yearly, and to be connected to the world community of atmospheric scientists; in particular, I am thankful for the Roland Schlich Travel Support, which I got in 2019.

Huge thanks to the Council for the Lindau Nobel Laureate Meetings and the Foundation Lindau Nobel Laureate Meetings, for the opportunity to participate in the 69th Lindau Nobel Laureate Meeting dedicated to Physics. Particularly, I am thankful to my sponsors for this meeting: Mars Incorporated and Foundation Lindau Nobel Laureate Meetings/Joachim Sorger Fund. The large thanks goes to Frank Mars, Board Director and Vice President of Sustainable Solutions in Mars Incorporated, for the inspiring and motivating discussions about world science, and coral reefs issue, in particular. Moreover, I am very thankful to get to know Dr. Sylvia Earle, a marine biologist, explorer, author, lecturer, former chief scientist of National Oceanic and Atmospheric Administrations (NOAA), founder of three ocean organisations – Deep Ocean Exploration and Research, Mission Blue and SEAlliance; it was a pleasure to discuss with her the current state of climate science. Furthermore, she became for me a good example of a successful and most inspiring female climate scientist. Special thanks goes to Prof. Dr. William Moerner from Stanford University, who became a Nobel Laureate in Chemistry in 2014; it was a pleasure to interact with Prof. Dr. William Moerner during the Lindau Nobel Laureate Meetings, and the notes and advices which he gave me became the motto of my current scientific path!

At this point I want to thank my school teachers in chemistry, Lidia Ryzhenko, and physics, Zinaida Hres', for arousing my interest to Nature Sciences.

The highest gratitude goes to my family, who gave me wings to explore this world, and the passion to learn. I am grateful to my parents, Yuriy and Svitlana Poshyvailo, who were and are always there for me, and gave me huge encouragement in all my endeavours; special thanks to my sister, Oksana, for her unwavering support; and thanks to Alexandre, who already became a part of the family, for the care, understanding, and support from day to day. I am thankful to my grandparents, Liubov and Mykola Poshyvailo, who gave me, since my childhood, a lot of support and confidence in my search for knowledge. Last but not least, I want to thank my uncle, Prof. Dr. Oles Poshyvailo, who motivated me to become a scientist, and still continues doing so, over and over, for further achievements and large ideas.

Contents

Chapter 1

Introduction and motivation

Stratospheric water vapour (H_2O) plays a critical role in global radiation, as it cools the stratosphere and warms the troposphere (e.g., Forster and Shine, 1999, 2002; Shindell, 2001; Maycock et al., 2011; Nowack et al., 2015). In particular, changes in H_2O mixing ratios in the upper troposphere and lower stratosphere (UTLS) may cause significant effects on climate variability (Solomon et al., 2010; Riese et al., 2012; Maycock et al., 2013; Nowack et al., 2017). Therefore, the reliability of climate model predictions is significantly affected by the representation of processes controlling the distribution of stratospheric H_2O. However, these processes, are poorly understood and quantified hitherto. Moreover, accurate measurements of the variability and trends of H_2O in the UTLS are sparse (Hegglin et al., 2014; Müller et al., 2016). These factors make the representation of stratospheric H_2O a major uncertainty factor for global climate model predictions (Gettelman et al., 2010; Randel and Jensen, 2013).

A critical region controlling stratospheric H_2O is the tropical tropopause layer (TTL). The TTL includes the region of extremely low temperatures around the cold-point tropopause, where the moist tropospheric air is freeze-dried to stratospheric values (Brewer, 1949). Consequently, the tropical cold-point temperatures control the amount of H_2O entering the stratosphere (e.g., Wang et al., 2015; Kim and Alexander, 2015; Randel and Park, 2019). H_2O is transported from the troposphere through the TTL into the stratosphere by complex transport processes, involving large-scale upwelling and horizontal advection, linked to the residual mean mass circulation (often referred to as Brewer-Dobson circulation, BDC), as well as small-scale vertical and horizontal mixing processes (e.g., due to convection or turbulence).

The BDC is a global mass circulation (meridional overturning circulation or diabatic circulation), in which tropospheric air enters the stratosphere in the tropics, and then moves upwards and polewards, before descending in the middle and high latitudes. The chemical source of H_2O in the middle and higher stratosphere is, mainly, the oxidation of methane (CH_4) by $O(^1D)$, OH, and Cl radicals (e.g., Röckmann et al., 2004). Importantly, H_2O has the largest greenhouse effect by absorbing and emitting infrared (IR) radiation on a range of wavelengths broader than any other greenhouse gas (e.g., Easterbrook, 2016). Thus, UTLS H_2O is involved in important climate feedback mechanisms, and plays a key role in climate change (e.g., Solomon et al., 2010).

As a reliable representation of stratospheric H_2O plays an important role in reducing the uncertainties in global climate model predictions, it is crucial to investigate the response of simulated stratospheric H_2O on changing various critical controlling factors in the models. The simulated stratospheric H_2O is strongly sensitive to TTL temperatures, large-scale horizontal transport and small-scale mixing.

The current generation climate models shows evidence for a speed up of the BDC, mainly as a response to an increase in greenhouse gases (e.g., Butchart et al., 2010; Garcia and Randel, 2008; Bunzel and Schmidt, 2013; WMO, 2018). Changes in the BDC, in turn, may induce important feedback mechanisms on climate. The BDC, however, can not be measured directly. Ergo, it is necessary to infer BDC trends from changes in trace gas distributions, such as H_2O. A commonly used quantity to describe the speed of the BDC is the mean age of air (AoA), the average transit time of air since entering the stratosphere. It is a complicated task to accurately determine the AoA from trace gas distributions. Consequently, the concepts of (I) an instantaneous propagation of stratospheric entry mixing ratio, and (II) stationarity of the correlation between AoA and the fractional release factor, are often used as the approximations (e.g., Schoeberl et al., 2000, 2005; Hegglin et al., 2014). There is a strong need to evaluate the effects of such approximations on the estimated AoA trend.

The aim of this thesis is to explain and solve the aforementioned scientific problems. The thesis consists of two main parts: (i) focusing on the processes controlling the stratospheric H_2O distribution (such as, TTL temperature, horizontal transport and small-scale mixing), and (ii) methods to use stratospheric H_2O trends for deducing BDC trends. The methodology is based on sensitivity studies with the Chemical Lagrangian Model of the Stratosphere (CLaMS, McKenna et al., 2002a,b).

The following questions about the uncertainties of modelled stratospheric H_2O mixing ratios, and the accuracy of estimated AoA trends from stratospheric H_2O changes are considered:

- How robust is simulated stratospheric H_2O with respect to different TTL temperatures in current meteorological datasets?
- How large is the effect of horizontal transport on stratospheric H_2O?
- How sensitive is stratospheric H_2O to atmospheric small-scale mixing?
- How reliable are estimated AoA trends from stratospheric H_2O changes?

Outline

This thesis consists of five chapters. The introduction presents an overview of the scientific background (Chapt. 2), introducing the structure of the atmosphere; particularly, UTLS region and the relevant processes. The mechanisms controlling stratospheric H_2O and the methods for observing and modelling of stratospheric H_2O are discussed in Chapt. 2 as well.

The methodology is described in detail in Chapt. 3. Each of the following chapters starts with a brief introductory paragraph. Thereafter, the research strategy and methodology are described. The chapters end with the conclusions answering the above raised questions.

In Chapt. 4, the uncertainties of simulated stratospheric H_2O with respect to the model representations of different processes (e.g., TTL temperatures, horizontal transport and small-scale

mixing) are investigated. A number of sensitivity simulations using CLaMS (McKenna et al., 2002a,b) in its 3D-version (Konopka et al., 2004; Pommrich et al., 2014) is carried out. CLaMS driven by ERA-Interim reanalysis (Dee et al., 2011) is considered as a reference. To investigate the uncertainties of stratospheric H_2O, the sensitivity simulations with CLaMS are analysed through their comparison to the ERA-Interim based reference simulation, and the effects of TTL temperatures, horizontal transport and small-scale mixing on stratospheric H_2O are estimated. This chapter is based on the following published paper:

- *Poshyvailo, L., Müller, R., Konopka, P., Günther, G., Riese, M., Podglajen, A., and Ploeger, F.: Sensitivities of modelled water vapour in the lower stratosphere: temperature uncertainty, effects of horizontal transport and small-scale mixing, Atmospheric Chemistry and Physics, 18, 8505-8527, https://doi.org/10.5194/acp-18-8505-2018, 2018.*

Chapt. 5 focuses on the method of deducing BDC trends from stratospheric H_2O trends, and evaluates the effects of commonly used approximations of (I) an instantaneous propagation of stratospheric entry mixing ratio, and (II) stationarity of the correlation between AoA and the fractional release factor of mathane. To evaluate the effects of the approximations on estimated AoA trends, the resulting AoA trends from the sensitivity experiments are compared to the reference CLaMS AoA trend. Based on such comparisons, conclusions regarding the reliability and applicability of approximations I and II in estimating AoA trends from stratospheric H_2O changes are made.

Finally, the summary and conclusions of the entire thesis are presented in Chapt. 6.

Chapter 2

Scientific background

2.1 Structure of the atmosphere

The Earth's atmosphere is a gaseous shell surrounding our planet, held together by the Earth's gravitational force. There are many dynamical, physical and chemical processes occurring there. Among other things, the Earth's atmosphere is a medium for energy transfer between the sun and the planetary surface, as well as between different regions of the Earth, including land and oceans. The processes of maintaining the energy equilibrium determine the climate of our planet. The atmosphere contains the elements necessary for life: oxygen (O_2), and the ozone layer (as a result of atmospheric reactions of O_2), which shields Earth's surface from harmful ultraviolet (UV) radiation. Thus, the Earth's atmosphere provides conditions for life to flourish, and moreover, it is a protector for living creatures against the radiation (Salby, 1996).

Relevant atmospheric processes occur on different spatial scales, starting from the microscopic (e.g., evaporation, condensation, cloud formation, precipitation), small- (e.g., localised vertical and horizontal wind motions), and medium- (e.g., cyclones, anticyclones, hurricanes, typhoons, tornadoes, thunderstorms, fronts), to large-scale processes, like the atmospheric general circulation. The radiative processes include transfer of incoming solar radiation through the atmosphere to the surface, the surface's heating, emission of outgoing IR radiation, and absorption of IR radiation by atmospheric gases and particles. Microphysical processes include evaporation and condensation of atmospheric H_2O into clouds. Through cohesion larger cloud droplets can be created, causing precipitation. Chemical processes transform and produce atmospheric gases, which can form atmospheric particles under certain conditions.

The Earth's atmosphere is a complex mixture of different gases. The main gases are nitrogen (N_2, about 78 % by volume), O_2 (about 21 % by volume), argon (Ar, about 0.9 % by volume), H_2O (from 0.01 % to 4 % by volume), and in even smaller amounts are carbon dioxide (CO_2), methane (CH_4) and many others.

Radical chemical species are very reactive, and control the ability of the atmosphere to oxidise chemical compounds into water-soluble gases, which are subsequently removed by precipitation (e.g., Schlager et al., 2012). The most prominent oxidising compound is the highly reactive hydroxyl radical (OH) (e.g., Brasseur et al., 2003). Halogen-containing stratospheric gases can be divided into two groups: halogen source gases and reactive halogen gases. Halo-

gen source gases, like chlorine- and bromine-containing gases (e.g., $CFCl_3$ (CFC-11), CF_2Cl_2 (CFC-12), $CBrF_3$) cause ozone depletion (WMO, 2018). When halogen source gases reach the stratosphere, they are chemically converted into reactive halogen gases through ultraviolet sunlight and other chemical reactions. Some other primary emitted gases, such as carbon tetrachloride (CCl_4), or photochemically-produced trace gases[1] are toxic, and may impact human health (Ramanathan et al., 1985; Schlager et al., 2012).

The lifetime of the atmospheric species varies from seconds up to more than a thousand years. An example of a very long-lived species is CO_2, which stays in the atmosphere for millennia (Archer and Brovkin, 2008). On a shorter time scale, of around 250 years, there is notable evidence of the change of atmospheric composition caused by human activity, produced by fossil fuel combustion and biomass burning (e.g., CO_2, SO_2, NO_x, hydrocarbons), traffic (e.g., CO_2, NO_x, CO), agriculture (CH_4, N_2O, NH_3), volcanoes (SO_2, halogens), vegetation (volatile organic carbon compounds), gas and oil production (volatile organic compounds, CH_4) (Schumann, 2012). Most of the long-lived trace gases are important greenhouse gases and have large effects on the atmosphere's radiation budget.

The increase of greenhouse gas concentrations is observed to cause global warming (Stocker et al., 2013; Blunden and Arndt, 2017; Solomon et al., 2010). Greenhouse gases cause warming of the troposphere and cooling of the stratosphere and induce further circulation changes, like a poleward shift of the tropospheric jet stream, which in turn causes climate change (Gerber et al., 2012; Kushner et al., 2001; Yin, 2005).

Interestingly, atmospheric H_2O has the largest greenhouse effect, as it emits and absorbs IR radiation on a broader range of wavelengths than any other greenhouse gases (e.g., Easterbrook, 2016). Consequently, atmospheric H_2O is involved in important climate feedback mechanisms. As atmospheric temperatures increase (caused by higher CO_2 concentrations), the resulting humidity increases as well (Dessler et al., 2013; Solomon et al., 2010). In addition, H_2O traps energy before it can escape to space, leading to additional warming. The entire stratospheric H_2O is mainly defined by the processes in the tropical upper troposphere and lower stratosphere (UTLS; e.g., Held and Soden, 2000; Solomon et al., 2010). UTLS H_2O is largely influenced by the BDC. Also, small-scale processes (e.g., microphysics of clouds, mixing) impact UTLS H_2O. Due to the interaction between the large-scale and small-scale processes, it is a challenging task to interpret the processes controlling UTLS H_2O (Fueglistaler et al., 2009; Dessler and Zelinka, 2015).

The Earth's atmosphere constitutes a fluid system, and can be considered as a mass of moving molecules. The solution of fluid dynamics problems usually involves the calculation of velocity, pressure, density and temperature as functions of space and time. Typically, the structure of the atmosphere can be considered as well in terms of pressure, density, and temperature. In the following, the vertical structure of the atmosphere is considered in more detail.

In the atmosphere, both pressure and density have the highest values at the surface, and decrease exponentially with height. This is caused by the gravitational force of the Earth and air compressibility. The pressure at the surface is around 10^5 Pa, and decreases to 10 % of this value at the altitude of about 15 km. Further, pressure decreases by one order of magnitude for

[1] **Trace gas** is a gas which makes up less than 1 % by volume of the Earth's atmosphere. All gases belong to the trace gases, except N_2 and O_2.

each additional 15 km. The mean density of atmospheric air decreases at about the same rate, by one order of magnitude for each 15 km of height, starting from about 1.2 kg m^{-3} at the surface. Above 100 km, pressure and density also decrease exponentially, although the rate is different, and it varies gradually with altitude. The transition layer near an altitude of about 100 km is caused by differences in the processes controlling the stratification of mass and the composition of air. Thus, the region below 100 km is well-mixed, and turbulent air motions dominate diffusive transport and is known as the *homosphere*. Between 100 km and approximately 500 km, diffusive transport dominates: this region is called *heterosphere*. Higher up, above 500 km, the air is so rarefied, that the molecules can leave the atmosphere and escape into space; this region is known as the *exosphere* (Salby, 1996).

The wide variety of the Earth's atmospheric composition causes a complex behaviour in the temperature profile. As a result of the inclination of the Earth's rotational axis, the tropics receive more heat from the solar radiation than the polar regions in average. Based on the thermal structure of the atmosphere, it is natural to divide the atmosphere in four layers. They are named *troposphere*, *stratosphere*, *mesosphere*, and *thermosphere*.

The *troposphere* (*tropos* means *turning, changing*) is a layer of the atmosphere, from the surface, up to about 10-15 km (the boundary depends on the latitude and season). It is also called sometimes the "lower atmosphere". In the troposphere, the temperature decreases with height with an almost constant lapse rate of

$$\Gamma = -\frac{\partial T}{\partial z} = -6.5\,\text{K/km}, \tag{2.1}$$

where T is temperature, and z is height. By definition, the environmental lapse rate (Γ) is the rate of temperature decrease with height (Willett and Sanders, 1959).

The troposphere contains approximately 80 % of the atmosphere's mass. The air in the troposphere is relatively well-mixed. The upper boundary of the troposphere is called the *tropopause*, and it is characterised by the first temperature minimum, and a sharp change in the lapse rate (Hoinka, 1997). This first atmospheric temperature minimum is referred to the *cold-point tropopause* (e.g., Andrews et al., 1987; Randel and Jensen, 2013). The World Meteorological Organisation defines the tropopause as "the lowest level, where the lapse rate decrease to 2 K/km or less, and the averaged lapse level within this level and the next 2 km layer should not exceed 2 K/km" (Holton et al., 1995). In the tropics, the region from the top of main convective outflow ($\approx$ 12-14 km) up to altitudes of the highest level convection can reach ($\approx$ 18 km) is a transition from convective to radiative regimes, and is termed the *tropical tropopause layer (TTL)* (Randel and Jensen, 2013; Fueglistaler et al., 2009).

The region between the tropopause, up to an altitude of approximately 85 km is usually named the *middle atmosphere*. Hoskins (1991); Holton et al. (1995) defined the terms "underworld", "middleworld" and "overworld" for the regions between the troposphere and the stratosphere. Such division requires the concept of *potential temperature*. Note that potential temperature (θ) is defined as the temperature that a parcel of dry air at pressure p and temperature T would have if it was compressed adiabatically to a standard surface pressure p_s (usually taken to be 1000 hPa):

$$\theta = T(p_s/p)^{R/c_p}, \tag{2.2}$$

where R is the gas constant for dry air ($R = 287\,J\,kg^{-1}\,K^{-1}$), and c_p is specific heat of dry air at a constant pressure ($c_p = 1004\,J\,K^{-1}\,kg^{-1}$) (e.g., Holton, 2004). The potential temperature is an important concept, as it represents a line of thermodynamic equilibrium for dry air in which there is no exchange of energy with the environment through radiative absorption or emission, or through turbulent mixing. All parcels lying along a constant θ surface are in local thermodynamic equilibrium (Salby, 1996).

In Hoskins (1991) the "middleworld" is defined as a region, where the isentropes cross the tropopause. Note, that an isentropic surface is a surface in space of constant potential temperature. The atmospheric layer above the tropopause is named as *stratosphere* (*strato* means *layered*). Here the temperature increases with height, what inhibits vertical mixing. Moreover, the stratosphere is rich in ozone. Ozone heating from the absorption of solar UV radiation, causes the temperature increase in the stratosphere. The upper boundary of the stratosphere is around 50 km, and is called the *stratopause*, where the atmospheric temperature again reaches its maximum (Salby, 1996).

Holton et al. (1995) proposed a separation into "underworld" and "overworld". "Underworld" is the part of the atmosphere where the isentropes lie completely in the troposphere and "overworld" is above the potential temperature of 380 K (approximately 100 hPa), where the entire isentropes lie in the stratosphere. In the tropics the level of 380 K lies just at the tropical tropopause in the annual mean, near the 100 hPa pressure level (Holton et al., 1995). The term "lowermost stratosphere" refers to the region between the tropopause and the 380 K isentropic surface (Holton et al., 1995; Schoeberl, 2004).

The *stratopause* (around the potential temperature of 2000 K or 1 hPa or 50 km) separates the stratosphere and the mesosphere (*meso* means *in between*). The temperature again decreases with altitude above the stratopause, caused by the absorption of solar radiation by the rarefied atmosphere and the strong radiative cooling by CO_2 thermal emission into space. Such a radiative cooling strongly depends on the rate of the excitation and the relaxation of CO2 molecules caused by collisions (Allen et al., 1979). The transition surface at around 85 km (approximately 0.01 hPa) is called the *mesopause*, situated at the second temperature minimum (Salby, 1996).

Above the mesopause, the temperature increases constantly in the *thermosphere*. This part of the atmosphere sometimes is called the "upper atmosphere". In the thermosphere, solar radiation ionises the molecules of air, producing plasma of free electrons and ions, which interact with the Earth's electric and magnetic fields. Above the mesopause, solar activity plays an important role, whereas below its effect is less significant. In the thermosphere, air becomes so rarefied that it cannot be treated as a continuous fluid anymore (Andrews et al., 1987; Wallace and Hobbs, 2006).

2.2 Upper troposphere and stratosphere (UTLS)

The work of this thesis is focused on the UTLS processes and their influence on the stratospheric H_2O. The controlling processes, such as evaporation, condensation, transport and production by CH_4 are responsible for H_2O distribution in the UTLS, and cause its high variability (see Sect. 2.3, 2.4 for the details).

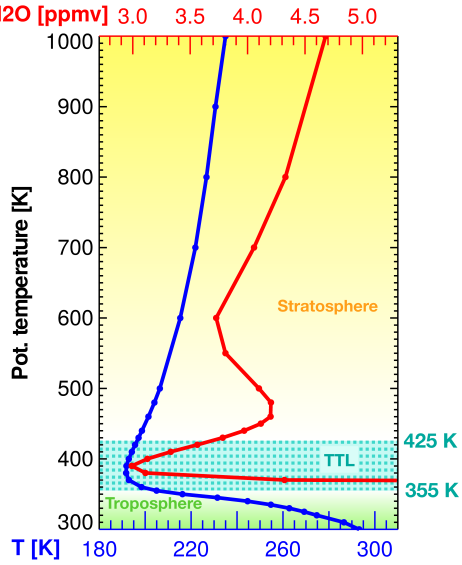

Figure 2.1: Temperature (blue line, [K]) and the H_2O mixing ratio (red line, [ppmv]) profile for the boreal winter season (DJF) climatologies (2004-2013 years) for the tropical region (20°S-20°N). The TTL is shown with the light blue area, whereas below, the troposphere is shown in green, and above, the stratosphere is shown in yellow colours. Note, that the temperature values are taken from ERA-Interim reanalysis, and the H_2O mixing ratios are from CLaMS simulation driven by ERA-Interim reanalysis.

Figure 2.1 presents temperature and H_2O mixing ratio vertical profiles for the boreal winter averaged through the tropics, between 20° S-20° N. Here, the TTL is shown with a bottom at the potential temperature of 355 K (or pressure 150 hPa, or altitude 14 km) and a top at 425 K (70 hPa, 18.5 km) following the definition of Fueglistaler et al. (2009). In Fig. 2.1, the minimum temperature in the TTL is around 190 K. At the same altitude, H_2O values reach the minimal mixing ratio of 3 ppmv[2], whereas in the troposphere, H_2O has much higher values. This H_2O minimum around 190 K is caused by the dehydration due to freezing in the TTL. Thus, the H_2O mixing ratio in the TTL is mainly controlled by the cold-point temperatures. The second minimum of lower magnitude appears around 600 K, indicating the presence of the low winter H_2O mixing ratios from the previous year in the stratosphere (the signal is known as the "H_2O

[2]**ppmv (parts per million by volume)** refers to a certain volume of a substance dissolved in one million parts per volume of other substances and is a unit of the quantity of the mixing ratio. In atmospheric chemistry, the abbreviations ppm (parts per million) and the term mixing ratio are used to denote a mole fraction in dry air (Calvert, 1990). Adding "v" is often used to separate molar and mass mixing ratio. Thus, a mole fraction of 300 ppm, is nearly equivalent to 300 ppmv, and exactly equal for an ideal gas. In the other words, for instance, 380 ppmv of CO_2 means that in the considered volume for every one million moles of dry air there are 380 moles of CO_2.

tape recorder"). Above this altitude, H_2O increases again in the middle and high stratosphere as a consequence of CH_4 oxidation and H_2O upward transport (see Sect. 2.4).

It is also important to mention that the temperature profile has a complicated structure at different latitudes and thus, influences H_2O behaviour differently, depending on the regions. An example is shown in Fig. 2.2 for winter (DJF) and summer (JJA) periods. The tropopause temperatures can reach values of around 190 K. These low temperatures cause the remarkable dryness of the stratosphere, because the moist tropospheric air moving upward needs to pass through this "cold trap" (Wallace and Hobbs, 2006). In the stratosphere, the temperatures are

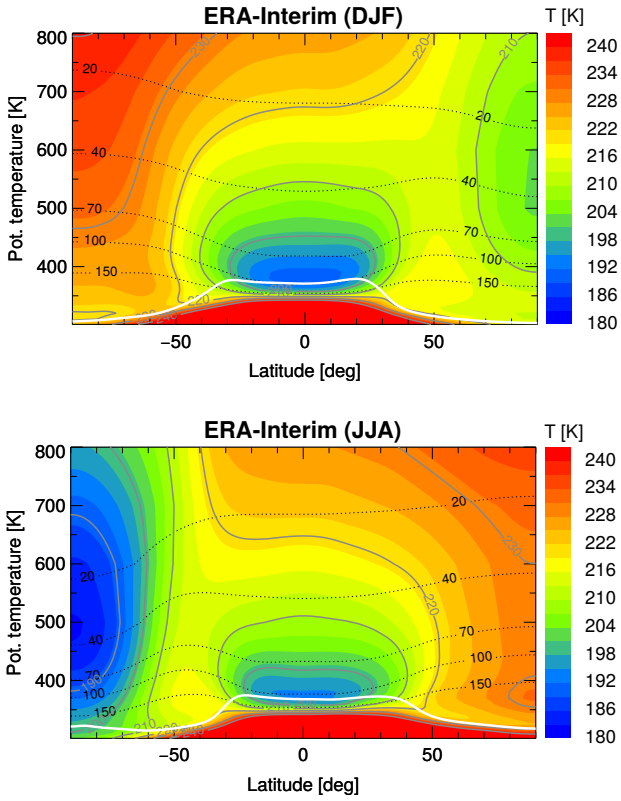

Figure 2.2: Zonally averaged temperatures (T, [K]) over 2004-2013 years from ERA-Interim for winter (DJF) and summer (JJA) periods. Dark violet contours show temperatures from 210 K to 280 K with the interval of 10 K. Black dotted lines are pressure levels (20, 40, 70, 100, 150 hPa). White lines around 100 hPa show the tropopause. Note that temperatures and pressure are from ERA-Interim reanalysis.

warmest over the summer pole, and decrease to colder values over the winter pole. The largest temperature impact on the stratospheric H_2O distribution is caused by the tropical tropopause and polar winter regions, where ice particle formation and sedimentation are the major control processes (shown with blue areas of low temperatures in Fig. 2.2).

The picture of zonally averaged zonal winds is presented in Fig. 2.3. The positive values of the zonal winds here represent westerly (west-to-east) winds, and the negative values represent easterly (east-to-west) winds. At the surface, zonal winds usually are comparatively weak. The vertical shear of the zonal wind is proportional to the meridional gradient of temperature

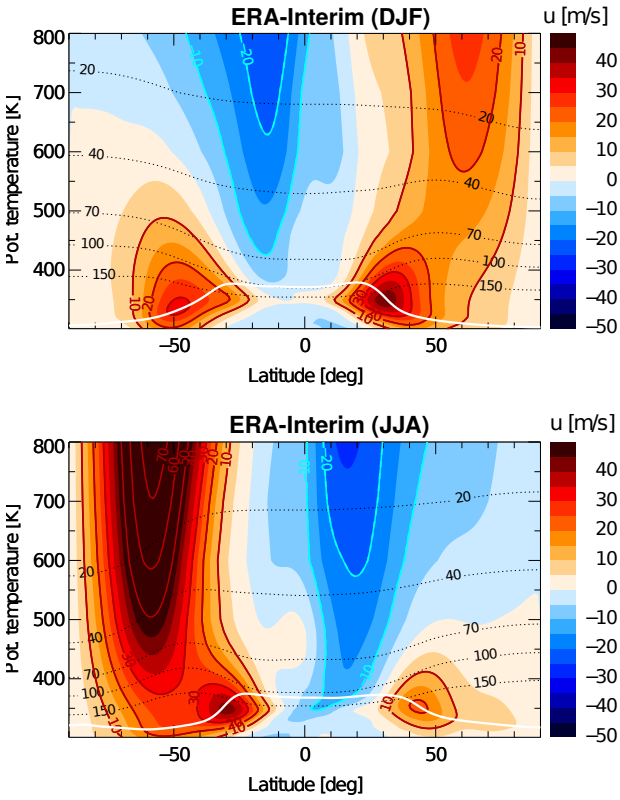

Figure 2.3: Zonally averaged zonal winds (u, [m/s]) over 2004-2013 years from ERA-Interim for winter (DJF) and summer (JJA) periods. Dark red lines show zonal winds from 10 m/s to 70 m/s with the interval of 10 m/s, blue lines represent the negative zonal winds respectively. Black dotted lines are pressure levels (20, 40, 70, 100, 150 hPa). White lines around 100 hPa represent tropopause. Note that velocities and pressure are derived from ERA-Interim reanalysis.

and inversely proportional to the Coriolis parameter (thermal wind balance). The temperature gradient is directed equatorward in most of the troposphere, and causes westerly wind shear. As the tropospheric temperature gradient is stronger in the subtropics (Fig. 2.2), the strongest westerly shear is also expected here. These zonal wind maxima refer to the tropospheric jet streams. Westerly winds increase with height in the high latitude stratosphere. The strongest westerly winds reach the lower mesosphere, and are associated with the polar night jet. The maximum speed of the jet streams is in the upper stratosphere, at around 10-30 hPa, which is between approximately 650 and 850 K at the potential temperature coordinates (e.g., Grotjahn, 2015).

2.3 UTLS processes

The UTLS region is situated at ± 5 km around the tropopause. As a reminder, the tropopause is from around 6 km (or approximately 300 K, or 400 hPa) at the poles to approximately 17 km (or approximately 400 K, or 70 hPa) at the equator. The UTLS is a crucial region for defining climate and weather on Earth (Gettelman et al., 2011). The UTLS features different radiative (e.g., photolysis, radiative heating), dynamical (e.g., forcing and propagation of Rossby or planetary waves[3], BDC, stratospheric-tropospheric exchange), and chemical (e.g., short- and long-time-scale) processes.

Figure 2.4 shows a scheme of the UTLS structure and the major processes occurring there. The main stratospheric transport is caused by the meridional overturning circulation (the residual circulation) and mixing, which together form the BDC (discussed in detailed below in Sect. 2.3.2). Quasi-horizontal extratropical mixing is prohibited by the subtropical transport barrier and by the winter-time polar vortex barrier. As a result, there is a significant contrast in the mixing ratio of chemical trace species between the extratropical lowermost stratosphere and the tropical upper troposphere. Mixing is most intense in the winter time "surf zone"[4] (McIntyre and Palmer, 1984), and it is relatively weak in the summer time in the extratropical regions. The largest diabatic ascent and descent (circulation) occurs in the tropics and in the polar vortices respectively (Eyring et al., 2005). Both mixing and the residual circulation are largely driven by momentum deposition (wave drag) from planetary waves. The propagation of planetary waves from the troposphere into the stratosphere can only be possible when westerly winds prevail, and thus, the BDC is stronger in the winter hemisphere.

The extratropical UTLS (Ex-UTLS) is a region of the extratropics that is influenced by the stratosphere from above, as well as by the troposphere from below, and also from the deep tropics via quasi-horizontal transport. The Ex-UTLS connects the troposphere and stratosphere through chemical mechanisms, dynamical processes (such as coupling between the stratospheric circulation and tropospheric wave patterns), and radiative processes via clouds and radiatively active gases (Gettelman et al., 2011). Through the BDC, chemical species are transported glob-

[3] **Rossby waves**, also known as **planetary waves**, naturally occur in rotating fluids. Within the Earth's ocean and atmosphere, these waves form as a result of the rotation of the planet influenced by the Coriolis force and pressure gradient (e.g., Rossby, 1939; Platzman, 1968; Dickinson, 1978; Hori et al., 2018).

[4] **Surf zone** is a main region of wave breaking, where the strongest quasi-horizontal mixing and irreversible tracer transport take place (McIntyre and Palmer, 1984).

ally (Andrews et al., 1987). Air entering the stratosphere in the tropics returns to the troposphere in the extratropics with a time scale of several years (Rosenlof, 1995). Hence, the troposphere and stratosphere are strongly coupled. Such stratosphere-troposphere exchange is important for understanding the changes of chemical species in the UTLS, which in turn influence radiative forcing (Pan et al., 1997).

The correct representation of the physical processes in the stratosphere is a complex task for climate models (Eyring et al., 2005). Below, we consider in more details the major processes controlling UTLS and stratospheric H_2O behaviour, such as TTL transport and the BDC.

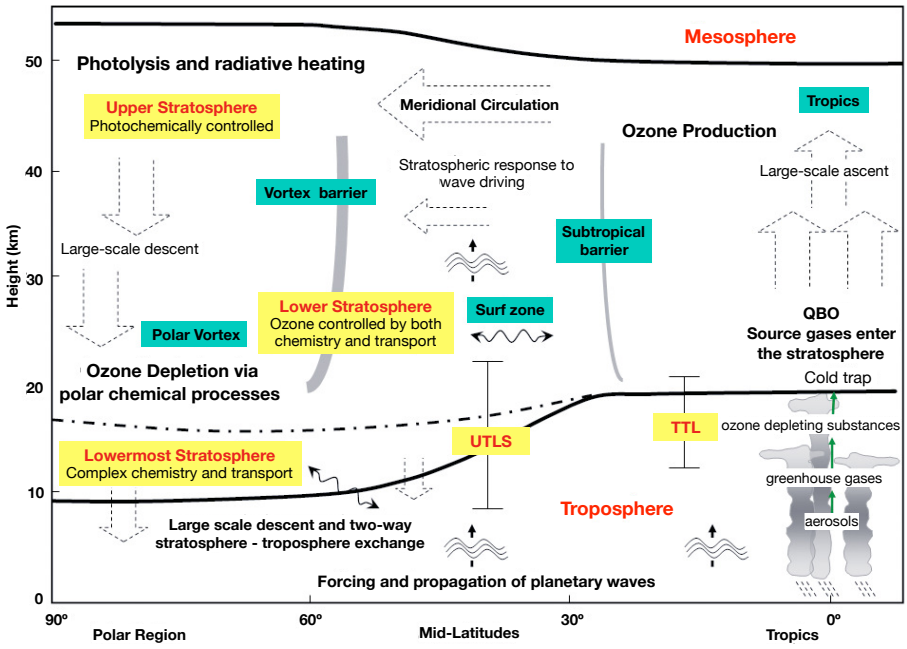

Figure 2.4: Schematic diagram of the main UTLS regions and processes, shown at one hemisphere (similar processes occur at the Southern and Northern hemispheres). Broad arrows denote BDC, and wavy arrows denote transport along isentropic surfaces. The average position of the tropopause is shown by the lower thick-black line, and the average position of the stratopause is shown by the upper thick-black line; the level of 380 K isentropic surface is presented by the thick-black dot-dashed line. The vertical bars denote the range of the UTLS and TTL. (The figure is adapted from Eyring et al., 2005)

2.3.1 Transport in the tropical tropopause layer (TTL)

The TTL has physical and chemical characteristics midway between the troposphere and stratosphere. Transport processes in the TTL are rather complex, involving large-scale upwelling and horizontal advection linked to the residual mean mass circulation, large-scale horizontal and small-scale vertical mixing processes, and deep convection. The mixing processes are particularly important during boreal summer, when mass transport related to the residual circulation is weak (Randel and Jensen, 2013; Ploeger et al., 2015b,a). Further, we look in detail at the TTL processes influencing stratospheric H_2O behaviour.

Figure 2.5 shows a zonal mean H_2O distribution during winter (DJF) within the TTL region and the dominant transport processes highlighted. The TTL is a region of a mean upward transport, and it acts as a "gate to the stratosphere" for trace species and pollution with sources in the troposphere (Fueglistaler et al., 2009). The lower TTL and the region below it, are characterised by strong convection over tropical continents and the western Pacific Ocean. Deep convection[5] drives the general circulation of the tropical troposphere, and controls transport of energy, H_2O, and other trace gases (Randel and Jensen, 2013). The solid green line in the tropics near 380 K (Fig. 2.5) shows the cold-point with tropopause temperatures reaching values of around 190 K. H_2O is freeze-dried here to the lowest mixing ratio values of approximately 2.7 ppmv. In winter, the minimum of the H_2O distribution is situated almost at the same position as the lowest TTL temperatures, as the lowest temperatures define the stratospheric entry values of H_2O. Dark yellow contours here represent the zonal average zonal winds, and the wriggled red lines highlight two-way isentropic transport between the TTL and extratropics. Rapid transport from the tropics to middle latitudes occurs mostly above the subtropical jets in both hemispheres, within the tropically controlled transition region (Rosenlof et al., 1997). Such horizontal transport between the TTL and middle latitudes is strongly influenced by the Asian monsoon anticyclone and other subtropical circulation systems (e.g., Bannister et al., 2004; James et al., 2008; Wright et al., 2011; Randel and Jensen, 2013). Furthermore, vertical mixing has also been shown to affect trace gas transport in the tropical lower stratosphere (LS) (Mote et al., 1998; Glanville and Birner, 2017). In addition, ice microphysics in the TTL affect H_2O. And because H_2O is radiatively active, TTL processes affect the Earth's climate (Eyring et al., 2005; Riese et al., 2012).

In summary, the TTL processes, such as the interplay between large- and small-scale circulation patterns, deep convection, clouds and radiation, define stratospheric H_2O. The TTL

[5] In general, **convection** is a heat transfer due to the bulk movement of molecules within fluids, and can be explained within an energy transfer concept. There are some types of convections, depending on the driving mechanism: **free convection**, when the motion caused only by density differences within the fluid (or air parcels, APs); and **forced convection**, when the motion induced by mechanical forces such as deflection by a large-scale surface irregularity, turbulent flow caused by friction at the boundary of a fluid, or motion caused by any applied pressure gradient. Atmospheric convection is nearly always turbulent. There are also shallow and deep types of atmospheric convection. **Deep convection** requires the volume of air to be lifted to a level where it is able to realize considerable positive (with virtual temperature greater than the environment) buoyancy over a significant depth. The vertical ascent raises the APs from the lower atmosphere above to 500 hPa (or approximately 310 K, or 6 km), and sometimes it can even penetrate the tropopause. Deep convection generally involves the vertical ascent of warm moist air and, ultimately, it dries the atmosphere and causes precipitation. **Shallow convection** has cloud top close to the top of the planetary boundary layer (varies between 1.5 to 5 km); and it moistens and cools the atmosphere (Randel and Park, 2006; Hegglin et al., 2004; Russo et al., 2011; Yano and Plant, 2012; Basha et al., 2019).

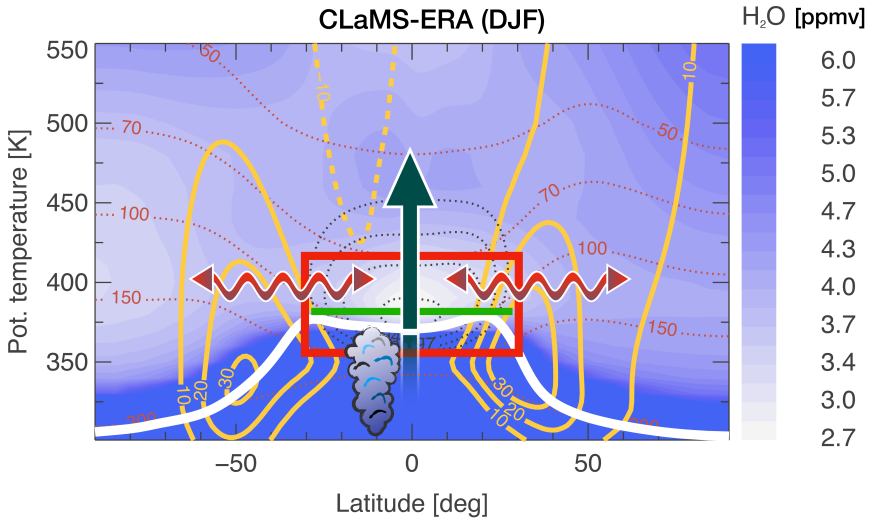

Figure 2.5: Zonal mean H_2O distribution for winter (DJF) period from CLaMS simulations, driven by ERA-Interim reanalysis, with a schematic of the TTL and related transport processes. Data shown are for 2004-2013 climatologies. The TTL is indicated with the red box, the white line is the thermal tropopause, the solid green line near 380 K shows the cold-point tropopause (all meteorological data are from ERA-Interim reanalysis). The upward arrow across the tropical tropopause indicates the large-scale upwelling associated with the BDC. The cloud in the troposphere represents deep convection. Black dotted contours show temperatures (191, 194, 197, 200 K), dark yellow contours are zonal winds (10, 20, 30 m/s), and red dotted lines are pressure levels (in hPa).

influences the entire global upper atmosphere (through temperatures and composition), as it is characterized by a large-scale mean upward circulation. The circulation is dynamically driven by large- and small-scale waves originating in the extratropics and the tropics, propagating upward into the stratosphere, and dissipating there. This wave drag induces a poleward motion in the lower stratosphere and mean upwelling within the TTL, forming the tropical component of the mean overturning circulation in the stratosphere (Randel and Jensen, 2013).

2.3.2 Brewer-Dobson circulation (BDC)

The expression “Brewer-Dobson circulation” was used for the first time in the paper of Newell (1963). This term describes a global transport circulation (meridional overturning circulation or diabatic circulation), in which tropospheric air enters the stratosphere in the tropics and then moves upward and poleward before descending in the middle and high latitudes. Such ideas were proposed by Dobson G. and Brewer A., based on observations of total ozone and stratospheric

H_2O (Dobson and Harrison, 1926; Dobson et al., 1929; Dobson, 1956; Brewer, 1949). The BDC is a global-scale phenomena observed in the Earth's atmosphere (Butchart, 2014).

The first estimation of the stratospheric meridional circulation was made by Murgatroyd and Singleton (1961) from diabatic forcing (based on diabatic heating rates). Later, Andrews and McIntyre (1978) demonstrated the advantages of using the Lagrangian-mean flow when compared to simple Eulerian-mean. Dunkerton (1978) derived a dynamically consistent picture of the mean-transport streamlines for the stratosphere and mesosphere, which is considered as the basic concept of the BDC.

Strong interest in investigating the BDC was raised as a result of the development of stratosphere-resolving general circulation models (GCMs) (Pawson et al., 2000; Samadi et al., 2010) and chemistry-climate models (CCMs) (Eyring et al., 2005), as well as the developments in observations and reanalysis (Seviour et al., 2012), and theoretical research (Plumb, 2002; Waugh and Hall, 2002). From these stratosphere-resolving GCMs and CCMs there is an evidence for a speeding up of the BDC, mainly as a response to an increase in greenhouse gases (Butchart et al., 2010; Garcia and Randel, 2008; Bunzel and Schmidt, 2013; Butchart, 2014; Oberländer-Hayn et al., 2016; Garfinkel et al., 2017; Šácha et al., 2019). Depending on the considered greenhouse gas scenario, models predict an increase in the upwelling mass flux in the tropical LS of about 2.0-3.2 % per decade (Holton et al., 1995). But, it is difficult to observe the speed-up of the BDC (Engel et al., 2009; Stiller et al., 2012; Seviour et al., 2012). However, Stiller et al. (2012) found an ageing of the stratospheric air from the observed sulphur hexafluoride (SF_6) datasets from Michelson Interferometer for Passive Atmospheric Sounding (MIPAS) measurements. The results of Stiller et al. (2012) also suggest an overall increase of the tropical upwelling together with the mixing barriers weakening, especially in the Northern Hemisphere (NH).

"Age of stratospheric air" is usually defined as the transit time[6] of the AP to a particular location in the stratosphere. The "mean age of stratospheric air" is the average transport time of the air from the tropospheric source region to a given place in the stratosphere (Garcia et al., 2011; Engel et al., 2017). The mean age of air (AoA, Hall and Plumb, 1994) is a useful transport diagnostic for accessing changes of the BDC. AoA can be validated from measurements of long-lived species (e.g., SF_6, CO_2), with linearly increasing concentration in the troposphere (Waugh and Hall, 2002). Due to atmospheric mixing processes, there is no single age for a stratospheric AP anymore, but instead a full transit time distribution, termed the "age spectrum" (Butchart, 2014; Waugh and Hall, 2002). The age spectrum allows to get more detailed information about the trace gases transport. AoA is defined as the first momentum of the age spectrum.

Often, BDC is called as "diabatic circulation", as it is associated with the diabatic processes of radiative heating and upward motion across the isentropes in the tropics and with the radiative cooling and downward motion across the isentropes in the extratropics. But the BDC circulation is not forced by radiative heating: it is a non-local response for the wave-driven pumping action (Holton, 2003). Such waves propagate from their sources in the troposphere towards the stratosphere. The underlying mechanism of the poleward mass flow in the middle and upper winter stratosphere is the "extratropical pump" (Holton et al., 1995), also known as the "Rossby-wave

[6] **Transit time** is a travel time between the initial point (taken at the stratospheric entry point around the TTL or at the surface) and the sampling volume.

pump" (Plumb, 2002). Planetary-scale Rossby waves can only propagate westward, and they decelerate the westerly flow when breaking. To conserve angular momentum, the air is pushed poleward, causing meridional flow. This, in turn, sucks up air in the tropics and pushes it down in the middle and high latitudes due to mass conservation. Some studies refer to tropical upwelling as "gyroscopic pumping", since the mechanism for the poleward flow involves a westward force with the poleward movements due to the Earth's rapid rotation (McIntyre and Norton, 2000). Other studies suggest that tropical upwelling is linked to equatorial waves forced by tropical deep convection (Boehm and Lee, 2003; Norton, 2006).

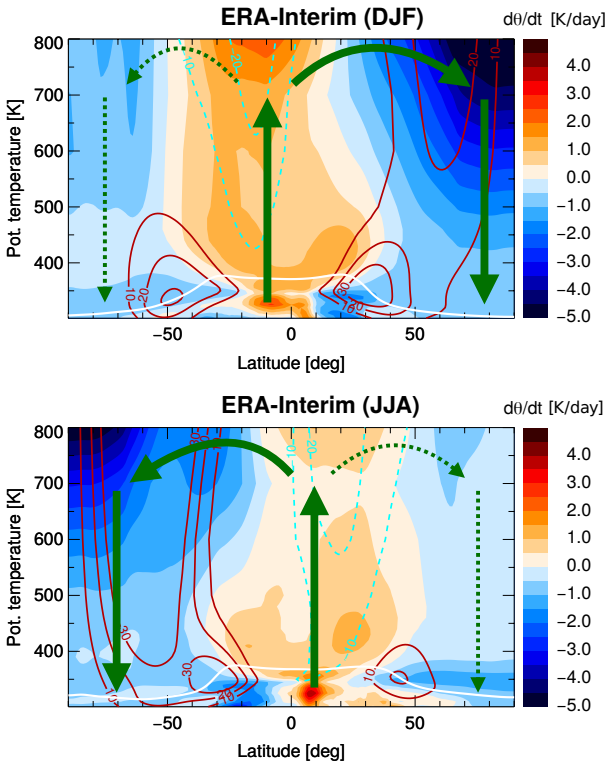

Figure 2.6: Zonally averaged diabatic heating rate distribution (in K/day) from climatologies for 2004-2013 from ERA-Interim for winter (DJF) and summer (JJA) periods. Dark red lines show zonal winds from 10 m/s to 30 m/s with an interval of 10 m/s, while blue dashed lines represent the negative zonal winds respectively. The white line is the tropopause. The green broad arrows highlight the main deep branches of BDC, whereas dashed arrows illustrate weaker circulation in the summer hemisphere. All data shown are taken from ERA-Interim reanalysis.

Plumb (2002) showed that the stratospheric BDC can be divided into two branches: a deep branch driven by planetary waves, and a shallow branch driven by synoptic and planetary scale waves. This study motivated Birner and Bönisch (2011) to derive the objective ways to separate these two circulation branches by studying BDC trajectories. Accordingly, the single-cell poleward transport in the winter hemisphere that extends into the middle and upper stratosphere has become known as the "deep branch" of the BDC. Faster "shallow branches" of the BDC, which do not propagate to high altitudes and extend only up to about 60° N/S, are observed in both hemispheres throughout the year.

Another way to define the BDC structure is through the transport across isentropic surfaces. The diabatic heating rate (Q) is related to the cross-isentropic vertical velocity by the relation of $Q \equiv d\theta/dt$, and therefore is a measure for cross-isentropic motion in the atmosphere (e.g., Holton, 2004). Figure 2.6 presents the diabatic heating rate distribution and highlights the main branches of the BDC, where the diabatic heating rate mainly increases in the tropics (ascent) and decreases in the polar regions (descent). The directions of the air movements are shown with the green arrows. Through the tropics, the upwelling air masses propagate to the higher levels of the stratosphere, with further descend in the middle and high latitudes. Solid green arrows represent the main upwelling and downwelling in the winter hemisphere, when compared with weaker circulation in the summer hemisphere (dashed arrows). Such motion is caused by breaking of the planetary waves in the middle stratosphere. The upwelling is stronger in the winter hemisphere than in the summer hemisphere. The region of the main upwelling is shifted to the summer hemisphere by approximately 10° of latitude.

Notably, the tropical stratosphere which is to some degree isolated from the extratropics (see Fig. 2.6) is termed as the "tropical pipe" (Plumb, 1996). Plumb (1996) assumed that mixing into the tropical pipe region is negligible compared with the effects of upwelling and sinks. In this way, the APs within the tropical pipe are advected upward without being influenced by the mid-latitude air. Later, Neu and Plumb (1999) extended the tropical pipe model to the "leaky pipe" model of stratospheric transport, including detrainment[7] of the air from the surf zone into the tropics. In this leaky pipe model it is allowed that the air mixes from the mid-latitudes into the tropics (Ray et al., 2010). Such representation of the atmosphere, using the leaky pipe model, is also consistent with observations in the tropical stratosphere (Volk et al., 1996; Mote et al., 1998). For instance, Volk et al. (1996) showed based on airborne in situ observations, that entrainment[8] of mid-latitude air into the tropics in the LS is significant.

2.4 Stratospheric water vapour (H_2O)

The key processes that control the stratospheric H_2O distribution are dehydration (caused by low temperatures at the TTL and the poles), transport due to the BDC and convection, CH_4 oxidation. As the impact of these processes is still not fully understood, there are the difficulties in predicting H_2O trends. Moreover, studying H_2O at the entry to stratosphere (near the TTL)

[7] **Detrainment** is a transfer of air from an organized air current to the surrounding atmosphere. It is an opposite to entrainment (AMS, a).

[8] **Entrainment** is the mixing of environmental air into a pre-existing organized air current so that the environmental air becomes part of the current (AMS, b).

is challenging due to the interaction between the large- (e.g., BDC, Hadley and Walker circulations[9]), middle- (e.g., convection), and small-scale processes (e.g., microphysics of clouds).

The processes controlling stratospheric H_2O (shown in Fig. 2.5) are the focus of this thesis and will be discussed in details.

2.4.1 Sources of stratospheric H_2O: transport and dehydration

A critical region controlling stratospheric entry H_2O is the TTL (Fueglistaler et al., 2009). The concentration of H_2O in the troposphere is high (up to 10^4 ppmv), and it is transported by the BDC upward through the TTL into the stratosphere (Palchetti et al., 2008; Harries, 2015; Kindel et al., 2015). The TTL includes the region of very low temperatures, where the moist tropospheric air is freeze-dried (dehydrated), to the low stratospheric H_2O mixing ratios (Brewer, 1949). As a result, the tropical cold-point temperatures control the amount of H_2O which enters the stratosphere (e.g., Wang et al., 2015; Kim and Alexander, 2015). Thus, after passing the "tropopause cold trap", the air entering the the stratosphere is extremely dry, with H_2O mixing ratios around 3 ppmv. The efficient dehydration occurs as a result of the slow upward and large-scale horizontal motion of air in the region, where the nucleation and sedimentation of ice crystals take place (Holton and Gettelman, 2001).

The annual cycle of TTL temperatures (minimum in boreal winter, maximum in summer) is imprinted on stratospheric entry H_2O mixing ratios, forming the signal known as "tape recorder" (Mote et al., 1995, 1996; Randel and Jensen, 2013). An example of the modelled H_2O tape recorder is shown in Fig. 2.7 at the potential temperature level of 390 K, which coincides with the tropopause layer at the tropical latitudes. Figure 2.7 demonstrates the transport of air from the TTL to the middle and high latitudes, denoted with black arrows at the plot. Around 20° S-20° N, where the cold-point tropical tropopause is situated, the air is dehydrated stronger during the boreal winter season. The summer maximum of tropical H_2O mixing ratios has been argued to be related, to some degree, to the subtropical monsoon circulations, like the Asian monsoon. Above the TTL, H_2O behaves mainly as a tracer, and the tape recorder signal imprinted at the cold-point tropopause ascends deep into the tropical stratosphere (Mote et al., 1996). However, the strength of this effect and the detailed processes involved (e.g., deep convection, large-scale upwelling) are a matter of debate.

Stratospheric H_2O is determined, to the first order approximation, by the large-scale temperature field through the Clausius-Clapeyron relation, which indicates that saturation H_2O pressure decreases approximately exponentially with decreasing temperature (e.g., Fueglistaler et al., 2004; Fueglistaler et al., 2005). The tropical stratospheric entry H_2O mixing ratios can be simulated by the advection through the large-scale temperature field and instantaneous freezing, often

[9]It is convenient to decompose the large-scale tropical circulation into **Hadley** and **Walker circulations**. The Hadley circulation is the mean meridional overturning circulation, whereas the Walker circulation is the longitudinal overturning circulation (Gastineau et al., 2009). Hadley circulation covers the tropical Pacific and the global tropics. This circulation consists of a rising branch, concentrated in a narrow zone, generally north of the equator, known as the intertropical convergence zone, and sinking motion, with increasingly strong surface easterlies, both north and south of the intertropical convergence zone (Chang and Zebiak, 2015). Walker circulation is caused by the sharp contrast in sea surface temperature across the tropical Pacific Ocean, and covers east-west atmospheric circulation cells along the equatorial belt (Lau and Yang, 2015).

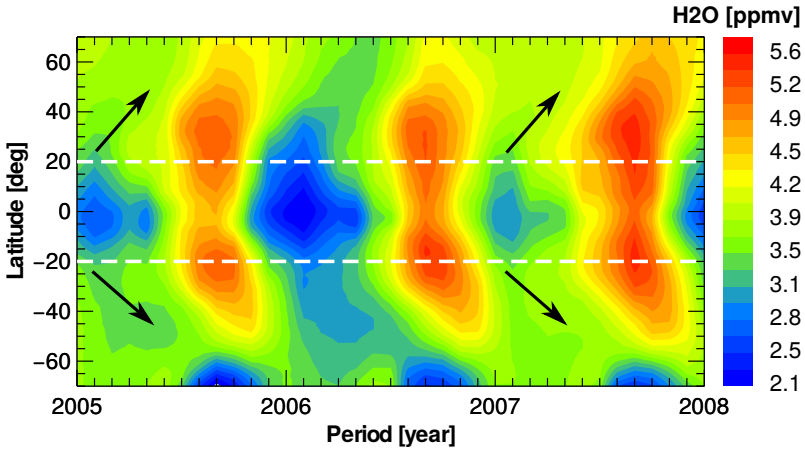

Figure 2.7: Horizontal tape recorder of H_2O in the LS at the potential temperature level of 390 K for the years from 2005 to 2008. Tropical region, 20° S-20° N, is shown with the dashed white lines. The black arrows present the horizontal transport from the TTL to higher latitudes. Shown data are from CLaMS simulations, driven by ERA-Interim reanalysis.

described as the "advection-condensation" paradigm cloud models (Pierrehumbert and Rocca, 1998; Fueglistaler and Haynes, 2005). However, based on trajectory studies driven by the reanalysis of European Centre of Medium-Range Weather Forecasts (ECMWF), Liu et al. (2011) showed that such results are sensitive to the temperature and vertical velocity fields.

The freezing is sensitive, not just to the large-scale TTL temperatures, but also to microphysical processes controlling the ice crystal number densities, particle size distribution, and fall speed. There are several studies focusing on the modelling of detailed cloud microphysical processes (e.g., Jensen and Pfister, 2004; Jensen et al., 2005, 2012). Other recent papers have examined the effect of cloud microphysical processes on the humidity of the TTL and stratosphere, using cloud models of varying complexity (e.g., Ueyama et al., 2015; Schoeberl et al., 2014).

Sublimation of ice, injected by deep convection, has also been argued to be an important factor for the H_2O budget of the tropical LS (e.g., Avery et al., 2017; Jensen and Pfister, 2004). Convection affects the transport of water and ice and influences the temperatures over the convective region which, in turn, affects dehydration (e.g., Fueglistaler et al., 2009). The predominant impact of convection has been shown to moisten the TTL by up to 0.7 ppmv at 100 hPa level (approximately 390 K), and even more below this level (e.g., Ueyama et al., 2014, 2015). Similarly, Schoeberl et al. (2014) argued that an increase of convection increases stratospheric H_2O and tropical cirrus clouds around the cold-point tropopause. At high levels in the TTL above the cold point up, there is the evidence of deep convection with a very weak moistening effect (e.g., Schiller et al., 2009).

2.4.2 Methane (CH_4) oxidation as a source of stratospheric H_2O

The oxidation of CH_4 and hydrogen (H_2) constitutes a chemical source of stratospheric H_2O in the middle and high stratosphere (e.g., LeTexier et al., 1988; Rohs et al., 2006; Röckmann et al., 2004). Three main components, H_2O, CH_4, and molecular hydrogen (H_2), enter the stratosphere from the troposphere. H_2O in the troposphere is continuously supplied from the surface by circulation. CH_4 is largely originated by anaerobic reactions, and H_2 comes from biomass burning and other natural sources at the surface. The mean globally averaged CH_4 mixing ratio near the stratospheric entry is around 1.7 ppmv, whereas H_2O enters the stratosphere with around 3-5 ppmv (lower values in winter, and higher ones in summer). H_2 at the entry to the stratosphere is around 0.5 ppmv (Dessler et al., 1994; Harries, 2015).

In the middle stratosphere, CH_4 is oxidized by OH and the excited oxygen atom $O(^1D)$, with a minor contribution from chlorine (Cl), forming the methyl radical CH_3:

$$CH_4 + O(^1D) \longrightarrow CH_3 + OH \tag{2.3}$$

$$CH_4 + OH \longrightarrow CH_3 + H_2O \tag{2.4}$$

$$CH_4 + Cl \longrightarrow CH_3 + HCl \tag{2.5}$$

Then, CH_3 in the middle stratosphere can be converted to the formaldehyde, CH_2O:

$$CH_3 + O_2 \longrightarrow CH_3O_2 \tag{2.6}$$

$$CH_3O_2 + NO \longrightarrow CH_3O + NO_2 \tag{2.7}$$

$$CH_3O + O_2 \longrightarrow CH_2O + HO_2 \tag{2.8}$$

Formaldehyde, CH_2O, may be photolysed, forming H_2 (Röth and Ehhalt, 2015) or may react with OH:

$$CH_2O + h\nu \longrightarrow CO + H_2 \tag{2.9}$$

$$CH_2O + h\nu \longrightarrow CHO + H \tag{2.10}$$

$$CH_2O + OH \longrightarrow CHO + H_2O \tag{2.11}$$

Additionally, in the middle and upper stratosphere the oxidation of molecular H_2 takes place, which is a source of H_2O (LeTexier et al., 1988; Dessler et al., 1994):

$$H_2 + O(^1D) \longrightarrow H + OH \tag{2.12}$$

$$H_2 + OH \longrightarrow H + H_2O \tag{2.13}$$

As a result of the CH_4 and H_2 oxidation, stratospheric H_2O increases with height. Whereas CH_4 mixing ratio decreases with height, and H_2 mixing ratio is kept almost constant because reactions which add and delete H_2 occur at similar rates. As a net result of the oxidation processes, each CH_4 molecule is converted into approximately two H_2O molecules. This also implies that H_2 production from CH_4 oxidation is balanced by H_2 oxidation.

It was shown from the satellite and balloon observations that the quantity of total hydrogen, ψ, defined as a sum of a principal components of the hydrogen budget (Harries, 2015), is constant with height through the most of the stratosphere.

$$\psi = H_2O + 2CH_4 + H_2. \tag{2.14}$$

The rough values of ψ are around 6.5-8.0 ppmv in the stratosphere (Harries, 2015; Dessler et al., 1994). H_2 has the smallest impact on ψ with the fraction of approximately 10 % in the stratosphere. Moreover, the mixing ratio of H_2 is usually uniform below the stratopause and equal to about 0.5 ppmv. Consequently, ψ is often taken as approximated (will be referred hereafter as HH):

$$HH = H_2O + 2CH_4. \tag{2.15}$$

HH is almost unchanged by transport in the stratosphere, and can be considered approximately constant (e.g., Jones et al., 1986; Dessler et al., 1994; Mote et al., 1998; Randel et al., 1998).

Note, that in recent study of Frank et al. (2018) was stated that the ratio between oxidised CH_4 and produced H_2O is not always 2. In this way, a yield of 2 overestimates the production of H_2O in the LS, which should be around 1.5-1.7 instead; and underestimates in the upper stratosphere and lower mesosphere, where true calculated values are above 2.2 (Frank et al., 2018).

2.4.3 Observations and modelling of stratospheric H_2O

There are various measurement techniques of in situ stratospheric H_2O: frost point hygrometer (e.g., Roulleau and Poc, 1978; Hurst et al., 2011; Hall et al., 2016); capacitance hygrometer (e.g., Neis et al., 2015); photofragment fluorescence spectrometer (e.g., Zöger et al., 1999; Weinstock et al., 2009); IR absorption spectrometer (e.g., Webster et al., 1994); chemical ionization mass spectrometer (e.g., Viggiano, 1993; Kaufmann et al., 2016). Some of those instruments, depending on the inlet configuration, measure the sum of the liquid water together with ice and its gaseous phase (referred to as "total water content"; e.g., Afchine et al., 2018).

The datasets of stratospheric H_2O can also be retrieved from the long-term global satellite observations, such as SAGE II (Satellite Aerosol and Gas Experiment, period of 1984-2005; e.g., McCormick, 1987; Chu et al., 1993; Rind et al., 1993; Thomason et al., 1997); HALOE (Halogen Occultation Experiment, 1991-2005; e.g., Russell III, 1991; Russell III et al., 1993); MIPAS Envisat (Michelson Interferometer for Passive Atmospheric Sounding, 2002-2012; e.g., von Clarmann and Stiller, 2003; Raspollini et al., 2006; Fischer et al., 2008); ACE-FTS (Atmospheric Chemistry Experiment-Fourier Transform Spectrometer, 2004-2012; e.g., Bernath et al., 2005; Bernath, 2017), Aura MLS (Microwave Limb Sounder, 2004-present; e.g., Waters et al., 1999, 2004, 2006). There are still uncertainties caused by different precisions, containing systematic errors from the instruments, or differences in the vertical resolution of measurements (Rollins et al., 2014; Smith, 2015). Particularly regarding long-term trends, analysis of UTLS stratospheric H_2O observations is challenging (Müller et al., 2016).

Satellite observations suggest that the horizontal transport from low latitudes affects the H_2O distribution in middle and high latitudes (Rosenlof et al., 1997; Pan et al., 1997; Randel et al.,

2001). Similarly, in situ H_2O observations in the LS NH suggest poleward transport of humid tropical air, especially, during the late summer and autumn seasons (e.g., Hoor et al., 2010; Vogel et al., 2016; Müller et al., 2018; Rolf et al., 2018). Additionally, model simulations confirm that almost the entire annual cycle of H_2O mixing ratios in the NH Ex-UTLS above about 360 K (with the maximum H_2O mixing ratios during summer and fall) is caused by horizontal transport from low latitudes, mainly from the Asian monsoon (Ploeger et al., 2013).

Based on satellite data and forward trajectory models, Dessler et al. (2013, 2014) point out that H_2O variability in the stratosphere can be explained largely by the quasi-biennial oscillation (QBO; e.g., Baldwin et al., 2001), the strength of the BDC, and the temperature of the TTL. Moreover, volcanic eruptions influence stratospheric H_2O entry, as volcanoes inject sulphur dioxide (SO_2) into the TTL, which is chemically converted to H_2SO_4 with further formation of diluted sulphuric acid droplets (H_2SO_4/H_2O). Stratospheric aerosols, composed largely from H_2SO_4/H_2O, reflect effectively the incoming solar energy back to space, causing the radiative cooling effect globally (Solomon et al., 2011). Thus, volcanic eruptions affect TTL temperatures and the amount of H_2O entering the stratosphere. Giorgetta and Bengtsson (1999), using a general GCM also found that volcanic eruptions, QBO and El Niño-Southern Oscillation (ENSO; e.g., Dessler and Wong, 2009; Butler and Polvani, 2011) can produce low-frequency variability in H_2O in the tropical stratosphere.

Schoeberl et al. (2013) investigated the H_2O distribution in the UTLS with a forward trajectory calculation model. It was found that the major UTLS H_2O supply areas were located in East Asia, the Tropical West Pacific (TWP) and Central/South America. The driest APs originated in the TWP region, move upward and dehydrate in the TWP cold upper troposphere. The wettest APs were originated at the edges of the TWP in the summer American and Asian monsoons.

Based on model simulations, Riese et al. (2012) showed the importance of small-scale mixing for the stratospheric H_2O. Thus, tiny changes in small-scale mixing, also related to deformations in the large-scale flow, can cause strong effects on the LS H_2O distribution. Consequently, uncertainties in the representation of small-scale mixing and diffusive transport in models may cause substantial uncertainties in the simulated stratospheric H_2O.

2.4.4 Stratospheric H_2O trends

There is evidence for decadal variability in the UTLS H_2O, but a long-term trend in the stratospheric H_2O entry is not evident during the past three decades (Dessler et al., 2014). The set of UTLS H_2O profiles obtained from the NOAA (National Oceanic and Atmospheric Administration) frost point hygrometer observations in Boulder, Colorado (situated at 40.0° N, 105.2° W), shows a significant increase of $\approx$1 % per year (approximately 0.1-0.45 ppmv per decade) in H_2O concentration in the LS (Oltmans and Hofmann, 1995). Note, that it is the longest continuous in situ time series of stratospheric H_2O, starting in 1980. It was found a similar positive trend in stratospheric H_2O of around 1 % per year over the period 1954-2000 (e.g., Hurst et al., 1999; Rosenlof et al., 2001; Kunz et al., 2013). However, contradicting negative trends during 1980-2010 are obtained from a merged zonal mean satellite dataset for a latitude band around Boulder's latitude of approximately 0.15 ppmv per decade (Hegglin et al., 2014). Such differences in the trends can be possibly explained by different temporal behaviour at the Boulder site (where measurements are influenced by both tropical and middle latitudinal air) and the used

zonal mean procedure for the satellite data, although this is a subject of further investigation (e.g., Hegglin et al., 2014; Lossow et al., 2018).

The UTLS H_2O merged satellite time series, averaged over 60° S-60° N, show a step-like drop after 2001, and an increasing trend since 2005 (Hartmann et al., 2013). Randel et al. (2006) point out a decrease in stratospheric H_2O beginning in 2001, and relate such a decrease to enhanced tropical upwelling after 2001, resulting in colder temperatures in the TTL. The decrease in H_2O mixing ratios at 15-20 km of about 0.4 ppmv is correlated to the decrease in TTL temperature of approximately 1 K (Randel et al., 2006).

Also other studies show a stratospheric H_2O drop of about 0.4-0.5 ppmv in October 2000, and an increase in stratospheric H_2O around 1991 of the same magnitude (Fueglistaler, 2012). The stratospheric H_2O drop in 2000 can be explained by anomalously large eddy heat fluxes in the Southern Hemisphere (SH) and related low tropopause temperatures. Stratospheric H_2O increase in 1991 is related to the eruption of Mt. Pinatubo, after which the amount of stratospheric aerosol was largely enhanced, causing a strongly intensified residual circulation (cooling the tropics) together with a rise in the radiative equilibrium temperature. Although the increase of stratospheric H_2O in 1991 could be only a coincidence with the eruption of Mt. Pinatubo; moreover, the datasets of stratospheric H_2O from SAGE II and HALOE between 1980's and 1995 are not well consistent (Fueglistaler, 2012). The interannual variability of stratospheric H_2O is linked to changes in tropical tropopause temperatures throughout the year (Fueglistaler and Haynes, 2005; Rosenlof and Reid, 2008).

In summary: the existing dataset of stratospheric H_2O from satellite measurements covers a relatively short period – from 1980s until present time – and thus, has only limited reliability in predictions of stratospheric H_2O trends. The fact that the increase in the long-term stratospheric H_2O trend cannot be fully explained by changes in tropical tropopause temperatures, CH_4 oxidation or other known factors, introduces additional complexity to the topic (Rohs et al., 2006; Hartmann et al., 2013; Fueglistaler et al., 2013; Hegglin et al., 2014).

Chapter 3

Data and method

3.1 CLaMS model set-up

To assess the sensitivities of simulated stratospheric H_2O, the Chemical Lagrangian Model of the Stratosphere (CLaMS) was used, a modular transport model, developed at Forschungszentrum Jülich (McKenna et al., 2002a,b). CLaMS is a Lagrangian model based on 3D-forward trajectories with an additional parametrization of small-scale mixing. The time dependent irregular CLaMS grid is defined by Lagrangian APs, which follow the large-scale flow. An advantage of the Lagrangian approach for simulating stratospheric transport is the ability to resolve small-scale features, which are often below the possible resolution of highly resolved Eulerian models (McKenna et al., 2002b). Such small-scale features are frequently observed in stratospheric trace gas distributions as elongated filaments, related to the stretching and differential advection in sheared flows (Orsolini et al., 1998).

CLaMS cosists of few modules, such as Lagrangian advection (TRAJ), stratospheric chemistry (CHEM), stratospheric mixing (MIX), freeze-drying and ice sedimentation of H_2O (CIRRUS), and several other modules responsible for simulation of various physical and chemical processes. The modules act successively at each time step. TRAJ, MIX and CIRRUS are the most relevant for this thesis and will be discussed in more details below. In addition, a simplified chemistry scheme was used in the performed CLaMS simulations, which includes CH_4 oxidation as a source of H_2O in the middle and upper stratosphere (for details see Pommrich et al., 2014).

3.1.1 Trajectory module (TRAJ)

The CLaMS trajectory module (TRAJ) performs full Lagrangian, non-diffusive, 3-dimensional advection of an ensemble of APs. There are approximately 2 million APs, which are advected at each time step. The initial positions of the APs are configured by creating an ensemble of n APs. The position of each AP is defined in hybrid isentropic coordinates (ζ, defined in Pommrich et al., 2014) and longitude-latitude space, and is stored in NetCDF initialisation file (for details see McKenna et al., 2002a).

The advection of forward trajectories in CLaMS is calculated based on a fourth-order Runge-Kutta scheme, as described by McKenna et al. (2002a), using 6-hourly wind fields from meteorological reanalysis data (ERA-Interim or JRA-55 in our study, see Sect. 3.2). Wind fields are linearly interpolated from the adjacent grid points to the locations of the APs.

For vertical transport, CLaMS uses a hybrid vertical coordinate ζ, which is an orography following σ-coordinate ($\sigma = p/p_s$) from the ground, and transforms into strictly isentropic θ-coordinate of potential temperature, above $\sigma = 0.3$ (about 300 hPa) (Mahowald et al., 2002; Pommrich et al., 2014). Hence, in the stratosphere the vertical transport is driven by the reanalysis total diabatic heating rate (Ploeger et al., 2010).

A horizontal resolution of about 100 km was used for the CLaMS simulations presented in this thesis. The vertical resolution was defined via a critical aspect ratio, equal to 250 (Haynes and Anglade, 1997). The critical aspect ratio expresses the ratio between horizontal and vertical scales. Thus, the vertical resolution in the simulations considered here was about 400 m around the tropical tropopause, degrading below and above this level (Konopka et al., 2012). The CLaMS simulations cover the atmosphere from the surface to about the stratopause (2500 K or $\approx$ 60 km). After the advection procedure performed with the TRAJ module, the new state of the APs ensemble is stored in an output NetCDF file.

3.1.2 Mixing module (MIX)

The parametrization of small-scale mixing in CLaMS is based on the deformation rate in the large-scale flow. Hence, APs may be merged, or new APs may be inserted at each time step (every 24 h), depending on the critical distances between them. The complete description of the mixing parametrisation scheme is presented in McKenna et al. (2002a); Konopka et al. (2004).

Briefly, each mixing event contains the following steps: firstly, the discrete vertical layers with a specific thickness are defined in accordance to the isentropic criteria (every layer should have approximately an equal number of APs). Secondly, the following procedure is done separately for each layer: nearest neighbours of each AP are identified using Delaunay triangulation on a horizontal projection of the vertical layer; namely, the initial positions of the APs within each layer is defined. From these positions, APs can be advected during the time step. The strength of parametrized small-scale mixing can be controlled by choosing a critical finite-time Lyapunov exponent (λ_c, constant at each time step) which, in turn, determines the critical distances between APs (for details see McKenna et al., 2002a; Konopka et al., 2004). Whenever the nearest neighbour APs move closer than a critical distance during one advection time step, they are merged into a single AP. Whenever they become further separated than a critical distance, a new AP is inserted in between (see McKenna et al., 2002a).

In order to perform mixing not only within a particular quasi-horizontal isentropic layer, but also between the adjacent layers (above or below), the definition of the layers after each time step is alternated by shifting the original layers by half of the layer thickness. Following the merging or inserting events, the mixing ratios of the APs will be recalculated as mean values of the APs taking part in the mixing event (for details see Konopka et al., 2004).

A validation of the CLaMS mixing scheme was presented by Konopka et al. (2005) in comparison to the observations from the experiment of Cryogenic Infrared Spectrometers and Telescopes for the Atmosphere (CRISTA-1). Importantly, the CLaMS mixing parametrization af-

fects both vertical and horizontal diffusivity. Horizontal diffusivity is largely associated with deformation in the horizontal flow, whereas the vertical mixing is mainly related to the vertical shear (Konopka et al., 2004, 2005).

3.1.3 Cirrus module (CIRRUS)

Dehydration in CLaMS is provided by the CIRRUS module, which includes freeze-drying in regions of cold temperatures, which mainly occurs around the tropical tropopause and in the Southern polar vortex. This, in turn, causes formation and sedimentation of ice particles.

The lower boundary for CLaMS H_2O simulation is taken from the reanalysis (ERA-Interim or JRA-55) specific humidity. If saturation along a CLaMS AP trajectory exceeds a critical saturation (100% with respect to ice), then the H_2O amount in excess is instantaneously transformed to the ice phase and partly sediments out. Such simple parametrisation has been adopted in several global Lagrangian studies (e.g., Kremser et al., 2009; Stenke et al., 2008). The saturation mixing ratio is calculated as $\chi_{H_2O} = p_s/p$ for each AP trajectory, with the saturation pressure being given by $p_s = 10^{-2663.5/T+12.537}$ (Marti and Mauersberger, 1993), where p is the ambient pressure (e.g., Kremser et al., 2009).

For sedimentation, the parametrization is based on a mean ice particle radius, the characteristic sedimentation length and the corresponding fall speed. The fallen path of the ice particles is calculated from the fall speed and the computation time step, and is compared with a characteristic sedimentation length of about the vertical grid size (here $l_c = 300\,\mathrm{m}$), which has been empirically optimized by comparison with observations (Ploeger et al., 2013). After this step, a respective fraction of ice will be removed. If the parcel is sub-saturated and ice exists, this ice is instantaneously evaporated to maintain saturation.

3.1.4 CLaMS remarks

The CLaMS mixing parametrisation is based on physical principles, as mixing occurs in regions of strong flow deformation, where it is expected to be in reality. In addition, due to the full Lagrangian transport scheme in CLaMS, the atmospheric transport barriers are well maintained, in particular at the edges of the tropical pipe and of the polar vortex (Hoppe et al., 2014).

Note that the CLaMS H_2O calculation gives meaningful results only above the tropopause, due the simple parametrization of ice microphysics and omission of a convection parametrization. In the stratosphere, however, CLaMS H_2O has been shown to agree well with the observations (e.g., Ploeger et al., 2013).

3.2 Meteorological reanalysis data

A meteorological reanalysis is a product of combined weather forecast model results with observations via data assimilation. In this way it is possible to derive a “best estimation” of the atmosphere state. Due to changes in the assimilation system (e.g., changes in available observations), artificial variability and trends can be introduced into the reanalysis products. A

reanalysis typically extends over several decades or longer, and covers the entire globe from the Earth's surface up to the stratosphere.

In this thesis, two reanalyses have been used: ERA-Interim and Japanese 55-year reanalysis data (JRA-55), to perform sensitivity studies with CLaMS.

ERA-Interim is a global atmospheric reanalysis, produced by ECMWF. The full description of the assimilation method used for ERA-Interim is given by Dee et al. (2011); Berrisford et al. (2009, 2011). ERA-Interim covers the period from 1979 until 2019. The data assimilation system includes 4-dimensional variational analysis (4DVar), with 12-hour analysis window. The spatial resolution of the dataset is approximately 80 km ($0.75^\circ \times 0.75^\circ$) on 60 vertical levels, from the surface up to 0.1 hPa. Gridded products of ERA-Interim consist of 3-hourly surface parameters (describing weather, ocean-wave and land-surface conditions), and 6-hourly upper-air parameters (troposphere and stratosphere).

A comprehensive report on JRA-55 was published by Ebita et al. (2011); Kobayashi et al. (2015). JRA-55 is a global reanalysis produced by the Japanese Weather Service. It covers the period from 1958 until 2019. The horizontal resolution is about 55 km, with 60 vertical levels from the surface up to 0.1 hPa in daily time steps. JRA-55 is the longest-running full observing reanalysis system with 4DVar. It is worth noting that JRA-55 has a time-varying warm bias in the upper troposphere, including a dry bias in upper and middle troposphere and in regions of deep convection.

3.3 Satellite observations

To validate the performed CLaMS simulations, the satellite observations from Aura Microwave Limb Sounder (MLS; in the thesis the Level 2 of Version 4 was used) and Atmospheric Chemistry Experiment-Fourier Transform Spectrometer (ACE-FTS; in the thesis Version 3.6 was used) were taken for comparison.

Detailed information on the MLS instrument can be found in Waters et al. (2004), and a general discussion of the microwave sounding technique is given in Waters et al. (1999). Briefly, the MLS instrument was launched in July 2004, on the National Aeronautics and Space Administration (NASA) Aura satellite and measured limb emissions in broad spectral regions. In total, MLS measurements include around 15 atmospheric chemical species along with temperature geopotential height, relative humidity, cloud ice water content and cloud ice water path, all described as functions of pressure. All measurements are made simultaneously and continuously, during both day and night (Waters et al., 2006). The resolution of the retrieved data is strictly related to the averaging kernels (Rodgers, 2000), which describe both vertical and horizontal resolutions. Particularly, the vertical resolution for H_2O is around 3 km in the UTLS region, whereas the along-track horizontal resolution is in between 170 and 350 km (Livesey et al., 2017). MLS measurements cover the range between 82° S to 82° N latitudes.

ACE-FTS is a satellite instrument, which is a part of the Canadian atmospheric science mission (SCISAT). The satellite was launched into the low Earth's circular orbit in August 2003. ACE-FTS covers the spectral region from 750 to 4400 cm^{-1}, and works mainly in solar occultation. During sunrise and sunset, the ACE-FTS instrument measures sequences of atmospheric absorption spectra in the limb-viewing geometry. Aerosols and clouds are being monitored us-

ing the extinction of solar radiation. Further, the spectra are analysed and inverted into vertical profiles. The satellite provides vertical profiles (typically, from 10 to 100 km) of temperature, pressure, and volume mixing ratios of several molecule species over the latitudes from 85° N to 85° S (Bernath et al., 2005). Solar occultation instruments, like ACE-FTS can have a high vertical resolution (around 1 km), but low horizontal resolution (about 300 km) in the limb direction (Hegglin et al., 2008). The detailed description of ACE-FTS is given by Bernath (2017).

Chapter 4

Sensitivities of modelled H_2O in the lower stratosphere (LS): temperature uncertainty, effects of horizontal transport and small-scale mixing

The major sources of stratospheric H_2O and involved processes are described in details above, in Sect. 2.4. As a reminder, the critical region controlling the amount of H_2O entering stratosphere is the TTL (e.g., defined in Fueglistaler et al., 2009), which extends from the level of main convective outflow around 12 km (about 340 K potential temperature) up to altitudes around 18 km (the highest level of convection). Stratospheric entry H_2O from the TTL distributes into the stratosphere by complex transport processes, which involves large-scale upwelling and horizontal advection, linked to the residual mean mass circulation, and small-scale mixing processes. The chemical source of H_2O in the middle and higher stratosphere is CH_4 oxidation.

In this chapter, we investigate the uncertainties of simulated LS H_2O due to the different tropopause temperatures (from the current reanalyses), horizontal transport, and small-scale mixing. To assess the sensitivities of simulated H_2O, the Chemical Lagrangian Model of the Stratosphere (CLaMS) was used. First, to investigate the robustness of simulated LS H_2O with respect to various meteorological datasets, CLaMS was driven by ERA-Interim and JRA-55 reanalyses. Second, to study the effects of horizontal transport on stratospheric H_2O, CLaMS sensitivity simulations with horizontal transport barriers along circles of latitude at the equator, at 15° N/S and at 35° N/S (Ploeger et al., 2013) were carried out. Third, to observe the uncertainties of stratospheric H_2O regarding different small-scale mixing schemes, the CLaMS parametrized mixing strength was varied. All performed types of sensitivity studies are described in Table 4.1, which summarizes the used reanalysis datasets, boundaries of the latitude barriers and the strengths of the Lyapunov exponent (where it is applicable).

The results regarding different reanalyses, horizontal transport and small-scale mixing strengths are presented below, and were published in Poshyvailo et al. (2018).

Simulation type	**Abbreviation**	**Reanalysis dataset**	**Latitude barriers**	**Lyapunov exponent** (λ_c, day^{-1})
Reference	REF	ERA-Interim	–	1.5
Reanalysis uncertainty	JRA-55	JRA-55	–	1.5
Horizontal transport effects	BAR-0	ERA-Interim	0°	1.5
	BAR-15	ERA-Interim	15° N/S	1.5
	BAR-15S	ERA-Interim	15° S	1.5
	BAR-15N	ERA-Interim	15° N	1.5
	BAR-35	ERA-Interim	35° N/S	1.5
Small-scale mixing effects	MIX-no	ERA-Interim	–	∞ (no mixing)
	MIX-weak	ERA-Interim	–	2.0
	MIX-strong	ERA-Interim	–	1.0

Table 4.1: CLaMS sensitivity simulations with respect to the used reanalysis datasets, horizontal transport barriers and small-scale mixing strengths. Note that the barriers are 10° wide (in latitude) with the central latitude indicated in the Table.

4.1 Simulation set-up

To study the sensitivity of simulated stratospheric H_2O regarding different reanalysis temperatures, horizontal transport effects, and small-scale mixing, we carried out a number of sensitivity simulations using CLaMS (McKenna et al., 2002a,b) in its 3D-version (Konopka et al., 2004). As a reference, we consider the run driven by ERA-Interim reanalysis data (Dee et al., 2011). To reach a steady state, we use a perpetuum technique, where the one year run (for 2011 conditions) is repeated several times. The initial values for the tracer fields at the first day of the simulation are taken from a long-term CLaMS simulation (Pommrich et al., 2014). After one year of the perpetuum calculation, tracer mixing ratios from December 31st, 2011 are interpolated to the APs positions on January 1st 2011, and the calculation is repeated for 2011 again. After the fourth time of the perpetuum, the maximum relative change of stratospheric H_2O mixing ratios between the consecutive perpetuum runs of the simulation is very small with the defined resolution and the time step (maximum year to year changes are below 1.0 %). As an example, Fig. 4.1 shows the relative changes in simulated H_2O mixing ratios (from the sensitivity studies of small-scale mixing effects) between different years of the perpetuum simulation for 1st of January, 2011. Consequently, we use the fifth year of the perpetuum simulation for our further analysis. Restricting the analysis to a single year instead of calculating a multi-year climatology has no effect on our conclusions regarding the differences between different simulations, as shown in Appendix A.

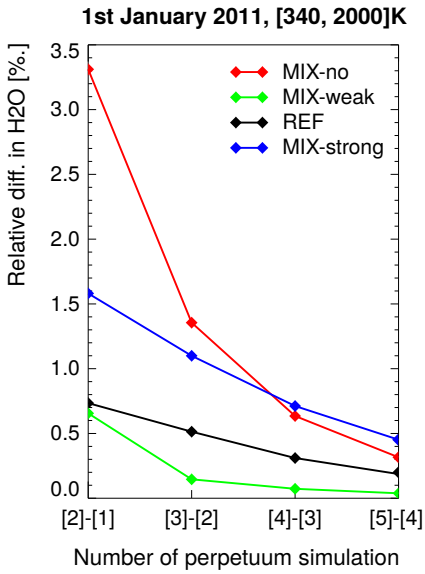

Figure 4.1: Relative differences in CLaMS simulated H_2O mixing ratios (from the sensitivity studies of small-scale mixing effects) between different years (denoted on X-axis) of perpetuum simulations for 1st of January 2011. The shown relative differences are averaged between 340 to 2000 K, over all ranges of latitudes and longitudes. The black line represents the CLaMS reference simulation (REF), with the other lines showing the cases without mixing (MIX-no, red), with weak (MIX-weak, green) and strong mixing (MIX-strong, blue).

In order to assess the robustness of simulated H_2O with respect to the meteorological datasets, we carry out another CLaMS simulation driven by the JRA-55 (Kobayashi et al., 2015), and compare it to the ERA-Interim based reference simulation.

Second, to assess the effects of horizontal transport, we carry out sensitivity simulations with horizontal transport barriers along circles of latitude at the equator, at 15° N/S and at 35° N/S (Ploeger et al., 2013). The transport barriers are defined in the model and centred at the given latitude. Their thickness is 10° in latitude (to inhibit diffusive mixing transport), and the barriers extend from the ground to a potential temperature of 600 K. The two types of barriers, BAR-15 and BAR-35, are located at the edge of the subtropics. BAR-15 is located at the equatorward edge and BAR-35 at the poleward edge of the subtropics. As such, both of them inhibit the transport from the subtropics. BAR-15 suppresses horizontal transport from the subtropics into the tropics, and BAR-35 suppresses transport from the subtropics to the extratropics. APs entering the barrier along their trajectories during one model time step are moved to their starting locations after Δt, as shown in Fig. 4.2. APs which were mixed into the barrier after the mixing procedure are moved to the closer barrier edge after the time step. Because of the broad barrier

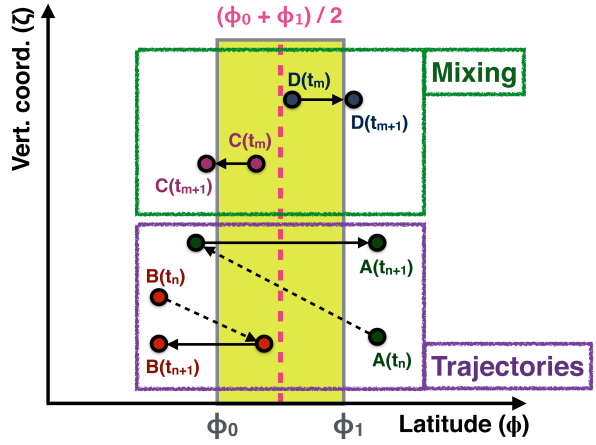

Figure 4.2: A schematic of the implementation of transport barriers in the CLaMS model into the trajectory and mixing modules, respectively. The X-axis represents latitude, the Y-axis is the vertical coordinate, respectively. The barrier is shown in light green colour, between ϕ_0 and ϕ_1 latitudes. The capital letters A, B, C and D represent the cross-barrier movements of different APs between time steps t_n and t_{n+1} for the trajectory module, and t_m and t_{m+1} for the mixing module.

width of 10°, this technique inhibits all cross-barrier transport. The CLaMS mixing parametrization ensures that no unrealistic clustering of APs occurs at the barrier edges.

The distributions of the APs (coloured accordingly to the simulated H_2O mixing ratio) with implemented horizontal transport barriers in CLaMS, is shown in Fig. 4.3. The effects of horizontal transport barriers on stratospheric H_2O are discussed in details in Sect. 4.4.

Third, to investigate the effects of small-scale mixing, we vary the parametrized mixing strength in CLaMS. A discussion of the choice of the critical Lyapunov coefficient, λ_c, controlling the strength of small-scale mixing in CLaMS, is given by Riese et al. (2012); Konopka et al. (2005). Hence, for a horizontal resolution of 100 km and a mixing step of 24 h, which were used also in our study, Lyapunov coefficients of 1.5 day^{-1} and 1.2 day^{-1} provide a good agreement between the observations and the simulation results, as indicated by the comparison of CLaMS simulations with observations from IR limb-sounding from the research aircraft Geophysica (Khosrawi et al., 2005). In particular, using the value of 1.2 day^{-1} gives a better agreement with observations in the 2D-version of CLaMS (Konopka et al., 2003). Furthermore, Konopka et al. (2004, 2005) showed that the value of λ_c = 1.5 day^{-1} (corresponding to the critical deformation of $\gamma_c = 1.5$) for the chosen horizontal resolution and time step here, turns out to be optimal for the 3D-version of CLaMS. Even for such a small difference in the small-scale

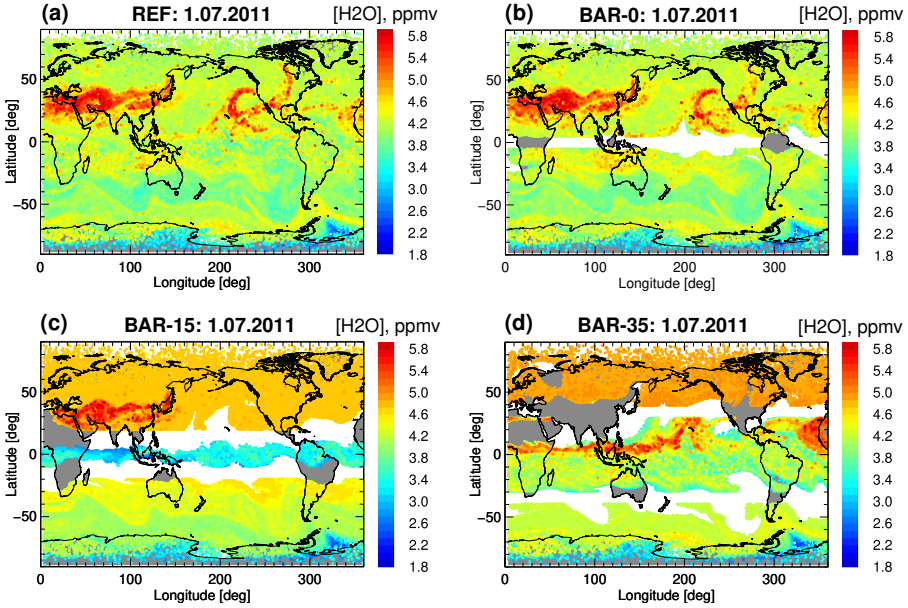

Figure 4.3: Maps of CLaMS APs distribution for the 1st of July 2011, at the potential temperature layer of 400±10 K: reference case (REF, a) and the sensitivity simulations with the horizontal transport barriers at the equator (BAR-0, b), at 15° N/S (BAR-15, c) and at 35° N/S (BAR-35, d). The colours of the APs respond to the CLaMS simulated H_2O mixing ratios. The transparent regions represent the areas without APs, including the artificial horizontal transport barriers.

mixing strengths, the annual mean H_2O concentrations in the extratropical LS differs by about 10-15% (Riese et al., 2012; McKenna et al., 2002a).

In our study we use a value of $\lambda_c = 1.5\,\mathrm{day}^{-1}$ for the reference run, $2.0\,\mathrm{day}^{-1}$ to represent weak mixing, and $1.0\,\mathrm{day}^{-1}$ for modelling strong mixing to cover the range of realistic small-scale mixing strength. Furthermore, we carry out a simulation without small-scale mixing (pure advection, when the mixing in CLaMS was switched off), equivalent to a critical Lyapunov exponent of infinity. The large range of the chosen mixing parameter here (λ_c) enables an investigation of sensitivities throughout a large range of possible mixing strengths, including significantly changed mixing characteristics in a potential future climate. As an example, the response of H_2O to different critical Lyapunov exponents is shown in Fig. 4.4 at 400 K. It shows the locations of the APs (presented with dots) coloured with respect to the mixing ratio values of simulated H_2O. As a remark, the case without small-scale mixing is not shown in Fig. 4.4, because it would not convey the right message due to the large spread of H_2O mixing ratios. The effects of different mixing strengths on stratospheric H_2O are discussed in detail in Sect. 4.5.

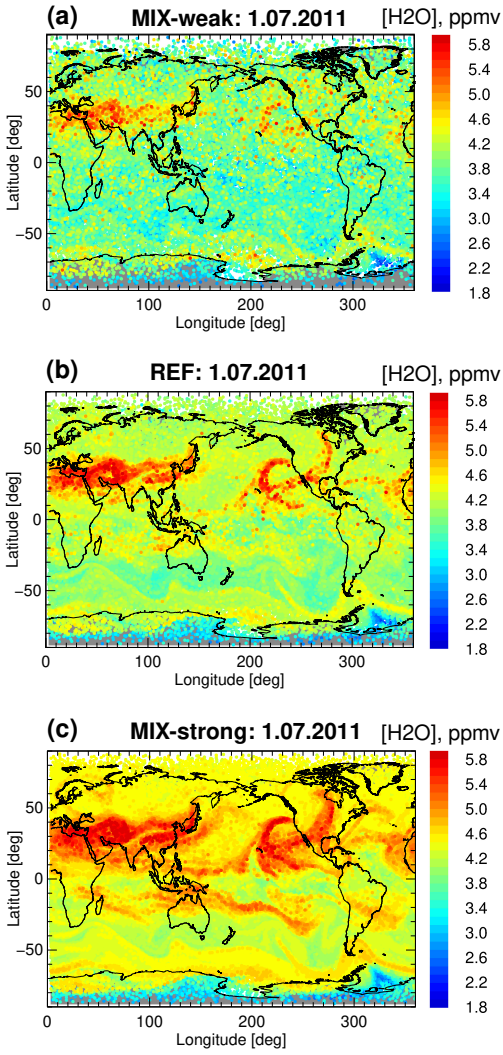

Figure 4.4: Maps of CLaMS APs distribution for the 1st of July 2011 at the potential temperature layer of 400±10 K from the sensitivity simulations with non-vanishing mixing strength: weak mixing (MIX-weak, a), reference case (REF, b) and strong mixing (MIX-strong, c). The colours of the APs respond to the CLaMS simulated H_2O mixing ratios.

Note, that small-scale mixing in CLaMS is parametrized in a physical way, by coupling the mixing intensity to deformations in the large-scale flow. The sensitivity of simulated H_2O to the parametrized mixing strength can therefore be regarded as representative to the response of changes in small-scale turbulence, as well as to the response of changes in numerical diffusion in climate models.

4.2 Stratospheric entry H_2O sensitivity

Figure 4.5 shows the annual cycle of tropical (10° S-10° N) stratospheric entry H_2O at 400 K for all performed simulations with CLaMS. While a clear annual cycle is evident for all cases, the mixing ratios vary by more than 1 ppmv between the simulations. The reference simulation (REF) agrees well with the MLS data, although there are some small differences during boreal winter. The largest sensitivity (spread between simulations) occurs for boreal summer and fall months. Suppressing horizontal transport from the subtropics into the tropics (BAR-15) significantly dries the tropical entry H_2O, with difference to the reference of up to around 1 ppmv. Note that with the tropical entry H_2O, we devote the H_2O entering the stratosphere at the level of potential temperatures of $\approx$ 400 K in the tropics (Fueglistaler et al., 2009). For the mixing sensitivity simulations, the largest difference from the reference case occurs for the case without mix-

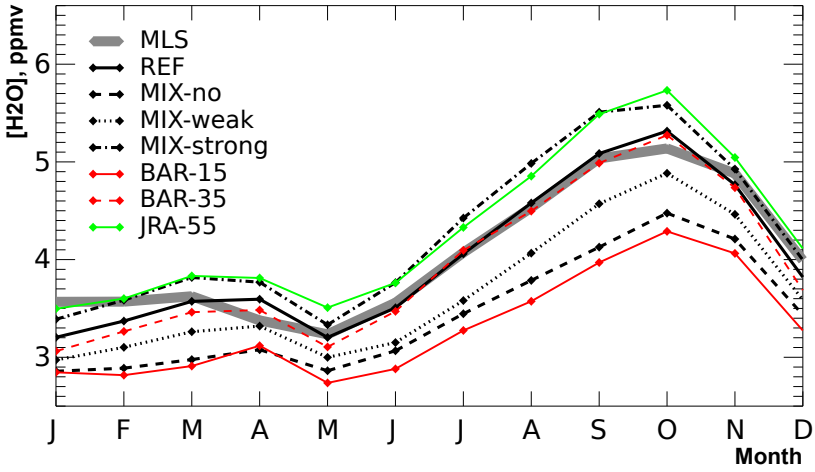

Figure 4.5: Annual cycle of tropical entry H_2O at 400 K (10°S-10°N) from different sensitivity simulations, with respect to variations in reanalysis datasets, horizontal transport and small-scale mixing for 2011. The grey line represents MLS satellite observations, for comparison. Shown are the reference simulation (REF), the cases without mixing (MIX-no), with weak (MIX-weak) and strong mixing (MIX-strong), the simulations with transport barriers at 15° N/S (BAR-15), at 35° N/S (BAR-35), and the simulation driven with JRA-55 reanalysis data (JRA-55).

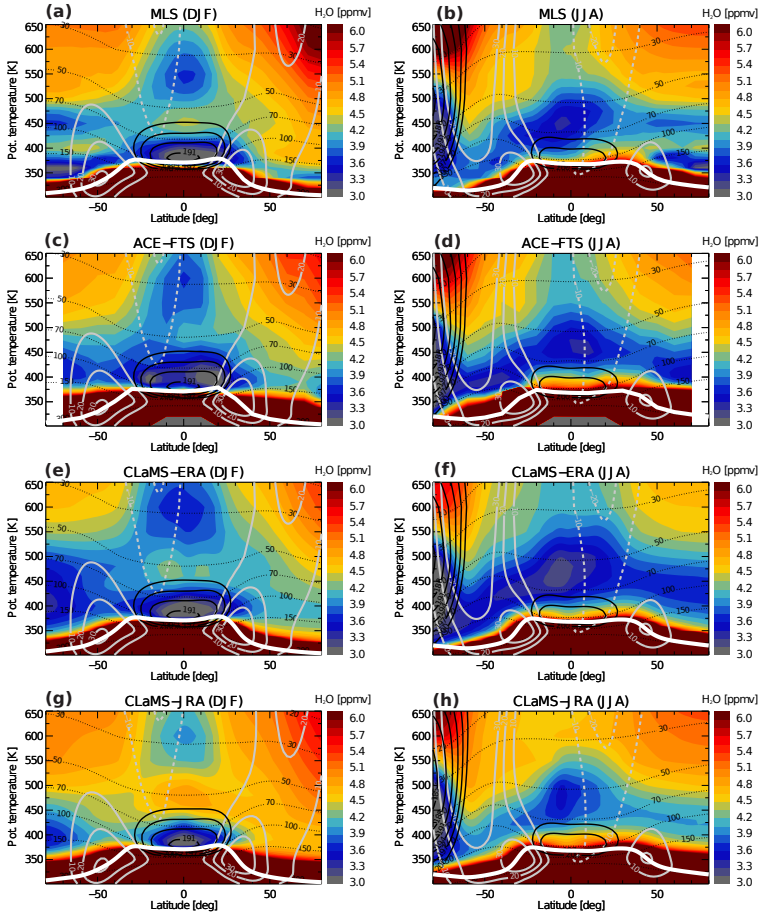

Figure 4.6: Zonal mean H_2O distributions for winter (DJF, left) and summer (JJA, right) from MLS and ACE-FTS satellite observations, as well as from CLaMS simulations driven with either ERA-Interim or JRA-55 reanalysis. Data shown are climatologies for 2004-2013 years. Black contours show temperatures (185 K, 188 K, 191 K, 194 K, 197 K, 200 K), grey contours are zonal winds (10 m/s, 20 m/s, 30 m/s), black dotted lines are pressure levels (in hPa) and the white line is the thermal tropopause. Note that the temperatures, zonal winds and pressure level contours are derived at the (a, b) and (c, d) from ERA-Interim sampled at the MLS or ACE-FTS locations respectively; (e, f) are from ERA-Interim and (g, h) are form JRA-55 reanalysis.

ing (MIX-no), with the MIX-no simulation dryer by about ≈ 0.8 ppmv in September-October. The CLaMS simulation driven with JRA-55 shows moister values in the TTL compared to the ERA-Interim simulation, which aligns with the recent findings of Davis et al. (2017).

The strong sensitivity of tropical entry H_2O shows the importance of such factors as the TTL temperatures from the used reanalysis dataset, horizontal transport and small-scale mixing, which are critical control factors for stratospheric H_2O. They will be investigated in more detail in the next Sections.

4.3 Reanalysis uncertainty

Zonal mean H_2O mixing ratios for boreal winter (December-January-February, DJF) and summer (June-July-August, JJA) from MLS and ACE-FTS satellite observations, and from CLaMS simulations, driven by ERA-Interim and JRA-55, are shown in Fig. 4.6. The comparison of the two different satellite datasets (first and second row) shows differences of about 0.5 ppmv (with ACE-FTS being moister), and even larger in the extratropical LS. Oscillations in MLS H_2O at high latitudes are a known effect of the broad averaging kernel (Ploeger et al., 2013). At low latitudes, the effects of the MLS averaging kernel on H_2O are much smaller, and we do not apply it to the model data here, in order not to smear out the structure in the simulated H_2O.

A comparison of the two simulations, driven by either ERA-Interim or JRA-55 (third and fourth row in Fig. 4.6), shows differences due to the used reanalysis dataset of about 0.5 ppmv, increasing towards the extratropical lowermost stratosphere. The main reason for JRA-55 causing a moister stratosphere when compared to the ERA-Interim is the positive difference in the temperatures around the TTL (Fig. 4.7). Zonal mean temperatures in this region are, on average, about 2 K higher for the JRA-55 than for the ERA-Interim. Remarkably, these differences only exist in a narrow layer around the tropical tropopause. In addition to the TTL temperature dif-

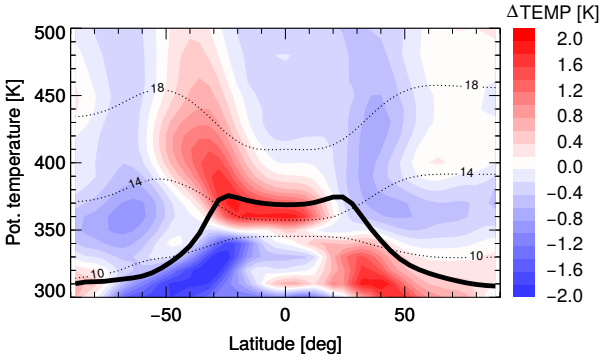

Figure 4.7: Differences in zonal mean temperatures between JRA-55 and ERA-Interim reanalysis data averaged for the period of 1979-2013; black dotted lines are altitude levels (in km) and the black line is the thermal tropopause.

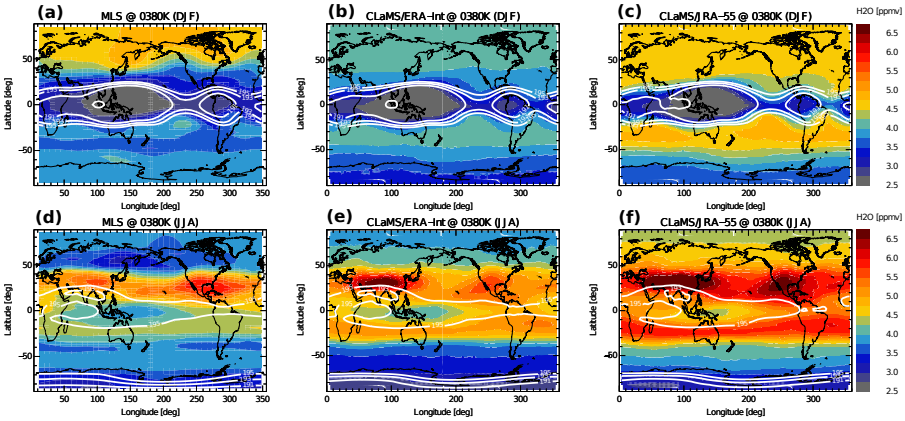

Figure 4.8: Maps of LS H_2O at the potential temperature level of 380 K from MLS (a, d), and CLaMS simulations driven by ERA-Interim (b, e) and JRA-55 (c, f). Shown are winter (DJF) and summer (JJA) data, respectively, from a 2004-2013 climatology. White lines show temperature contours (191 K, 193 K, 195 K). Note, that the temperatures at the (a, d) are from ERA-Interim sampled at the MLS locations, (b, e) are from ERA-Interim and (c, f) are from JRA-55 reanalysis.

ferences, also the differences in winds and heating rates between the two reanalysis could cause uncertainties in H_2O mixing ratios; however, the temperature difference provides a self-evident explanation.

A detailed comparison of the LS H_2O between MLS and CLaMS simulations driven by ERA-Interim and JRA-55 reanalysis at 380 K is given in Fig. 4.8. Note that the 380 K surface may be located well below the tropopause in some regions (e.g., Asian monsoon). The patterns of dominant freeze-drying regions above the West Pacific and South America in boreal winter are consistent between the observations and the two simulations. Notably, the larger area of low H_2O mixing ratios and colder temperatures for ERA-Interim when compared to JRA-55, is consistent with the drier global stratosphere, as discussed above. Also in boreal summer, the H_2O distributions for MLS observations and CLaMS, driven by the two reanalyses, are similar in the tropics. Nevertheless, in the subtropics, the strength of summertime monsoon anomalies in MLS differs from CLaMS, with the Asian monsoon dominating in both simulations, while the American monsoon appears stronger in MLS data (e.g., Ploeger et al., 2013). Note that in the tropical LS the long-term H_2O time series from CLaMS driven by ERA-Interim reanalysis agrees well with HALOE and MLS observations (Tao et al., 2015).

Overall, regarding the global H_2O distributions and maps in the LS, CLaMS modelling results with ERA-Interim are drier, when compared to JRA-55, resulting from lower TTL temperatures in ERA-Interim. The agreement between CLaMS based on ERA-Interim and JRA-55 with the observations strongly depends on the considered region and season. And it is not possible to

conclude from our analysis which reanalysis results in simulated H_2O shows the best agreement with the observations.

4.4 Horizontal transport

Probability density functions (PDFs) of H_2O mixing ratio (e.g., Schoeberl et al., 2013), allow a simple comparison of the overall effects of horizontal transport on H_2O (in the LS) by contrasting the various sensitivity simulations. Figure 4.9 shows these PDFs for the tropics and extratropics of both hemispheres, for the different barrier simulations.

In the SH (Fig. 4.9a), the frequent very low mixing ratios are insensitive to horizontal transport, indicating the occurrence of local dehydration. This insensitivity reflects the fact that temperatures in the Antarctic polar vortex are so low that H_2O mixing ratios are locally freeze-dried to the saturation value. However, there is a weak effect of transport from the NH on moistening the SH, indicated by a lowering of the PDF's tail without cross-equatorial transport. Suppressing transport from the tropics lowers the tail further, and suppressing transport from the SH subtropics (with the 35° S barrier) finally removes almost all mixing ratios higher than 5 ppmv.

In the tropics (Fig. 4.9b), the insignificant difference between the reference (REF) and an equatorial transport barrier (BAR-0) simulations shows that the interhemispheric transport is rather unimportant for tropical mean H_2O mixing ratios. Similarly, in-mixing of mid- and high-latitude air (see BAR-35) has a very small impact on tropical mean H_2O, which echoes the findings of Ploeger et al. (2012). In contrast, transport from the subtropics into the tropics has a strong effect. Suppressing such transport by applying a barrier at 15° N/S (BAR-15) changes the PDF substantially, as evident from the difference between the simulation BAR-15 and the reference cases. The isolation of the tropics due to the lack of horizontal transport in the BAR-15 simulation (all the way from the surface to 600 K) between the equator and the subtropics (both ways) causes dry air at the equator. Thus, with the barrier at 15° N/S the fraction of dry air at the equatorial region increases. The comparison of BAR-15 with BAR-35 shows that transport from the subtropical region into the tropics increases H_2O. Without transport from the subtropics, the tropical mean H_2O PDF appears more strongly skewed towards low mixing ratios (blue line in Fig. 4.9b), and the mean H_2O mixing ratio is shifted towards lower values by about 0.5 ppmv.

In the NH, cross-equatorial transport from the SH has only a weak effect, as visible from the equatorial transport barrier (Fig. 4.9c). The introduction of a transport barrier in the subtropics at 15° N removes the low mixing ratios from the PDF, showing that these low mixing ratios result from transport out of the deep tropics. Moving the transport barrier further away from the equator to 35° N changes the PDF drastically. In addition to the low mixing ratios, it also removes the tail of the PDF at high mixing ratios, such that a very narrow extratropical H_2O mixing ratio PDF remains. Hence, these high mixing ratios are the result of transport from the subtropics, and are likely related to the Asian monsoon, as argued by Ploeger et al. (2013). Accordingly, monsoon driven H_2O transport from the subtropics to the high latitudes is, by far, more pronounced for the NH, than for SH.

The pure transport effects of horizontal exchange between tropics and mid-latitudes are evident from the AoA, the mean transit time for air through the stratosphere for the different model experiments with horizontal transport barriers. Figure 4.10 shows CLaMS calculations of the

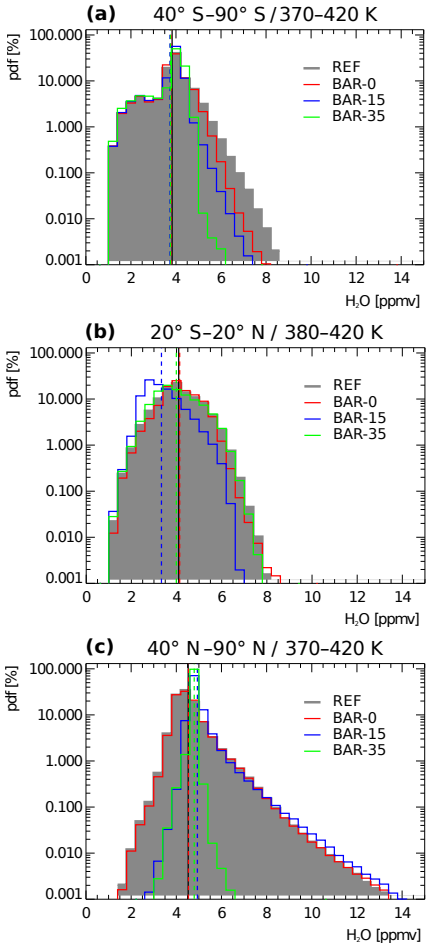

Figure 4.9: PDF of H_2O mixing ratios in the SH extratropics for 40° S-90° S between 370 K and 420 K (a), in the tropics for 20° S-20° N between 380 K and 420 K (b), and in the NH extratropics for 40° N-90° N between 370 K and 420 K (c). Shown data are from 2011 CLaMS sensitivity simulations with horizontal barriers along latitude circles at 0° (BAR-0, red solid line), 15° N/S (BAR-15, blue solid line), 35° N/S (BAR-35, green solid line) and the reference (REF, grey background). Dashed coloured lines represent the mean H_2O values for the different simulations respectively, whereas the black solid line shows the mean value of the reference simulation.

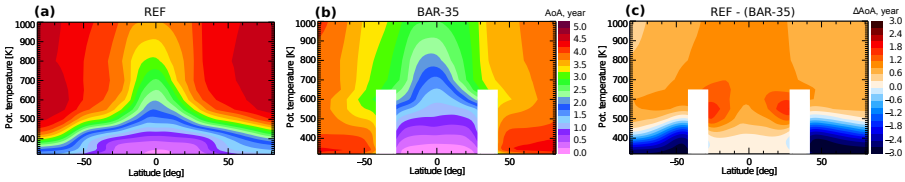

Figure 4.10: Zonal AoA distributions for 2011. Shown data are from the CLaMS reference simulation (a) and from the sensitivity simulation with barriers along latitude circles at 35° N/S (b) and the absolute difference between them (c). Transport barriers are set between the Earth's surface and the 600 K potential temperature levels and are represented in white.

AoA for the reference case (Fig. 4.10a) simulation, with transport barriers in the subtropics at 35° N/S (Fig. 4.10b), and the absolute difference between them (Fig. 4.10c). These horizontal transport barriers at 35° N/S effectively isolate the tropical pipe from the in-mixing of older stratospheric air from mid-latitudes, significantly decreasing the AoA globally by more than a year. Hence, recirculation from mid-latitudes into the tropics has a strong ageing effect on the stratosphere globally, which reinforces findings by Neu and Plumb (1999). Without recirculation (in the BAR-35 simulation) the global AoA distribution reflects mainly the pure effect of the residual circulation, resulting in oldest air in the extratropical lowermost stratosphere, and appears very similar to the distribution of residual circulation transit times (e.g., Ploeger et al., 2015a). Older air in the NH is related to the deeper NH residual circulation cell.

In the tropics, the age distribution in Fig. 4.10b shows a weak double peak structure up to about 500 K, indicating that the subtropics are regions of particularly fast transport likely related to subtropical processes like monsoon circulations. Suppressing transport in the subtropics with barriers at 35° N/S therefore significantly increases AoA in the extratropical stratosphere (Fig. 4.10c). A similar result has recently been shown by Garny et al. (2014). Furthermore, Garny et al. (2014) presents a nice explanation of the recirculation process, describing recirculation as a process when an AP enters the tropical stratosphere and travels along the residual circulation to the extratropics, where it can be mixed back into the tropics, and thus recirculates along the residual circulation again. In this way, the age of air of the parcels increases steadily while performing multiple circuits through the stratosphere.

Relating the pure horizontal transport effects (seen in the AoA) to H_2O is not straightforward, as H_2O is strongly controlled by TTL temperatures. Figure 4.11 shows the annual zonal mean H_2O mixing ratio for the different sensitivity simulations with transport barriers, and Fig. 4.12 highlights the differences between the simulations with largest H_2O changes. The small differences between the reference (Fig. 4.11a) and the equatorial barrier (Fig. 4.11b) simulations indicate only a very weak effect of transport processes in the deep tropics and interhemispheric exchange on global stratospheric H_2O. Similarly, the sensitivity simulation with a subtropical transport barrier at 35° N/S (Fig. 4.11c, 4.12c) shows that in-mixing of mid-latitude air has only a weak impact on global stratospheric H_2O (except in the NH LS). In contrast, transport from the subtropics, between 10° and 30° N/S, as visible from the comparison of sensitivity simulation

BAR-15 and BAR-35 (Fig. 4.5, 4.11c, 4.11d, 4.12a), has a strong effect on tropical entry H_2O and hence on global H_2O. Without such transport from the subtropics (Fig. 4.11a, 4.11d), the stratosphere becomes substantially drier (maximum differences through the entire stratosphere are up to about 1 ppmv). The fact that this drying occurs only with transport barriers at 15° N/S and not with barriers at 35° N/S, shows that it is not related to the suppression of recirculation of aged air from mid-latitudes, which has been affected by CH_4 oxidation. In fact, processes in the subtropics (e.g., monsoon circulations) have a strong effect in moistening the global stratosphere, and suppressing these processes in BAR-15 causes drying.

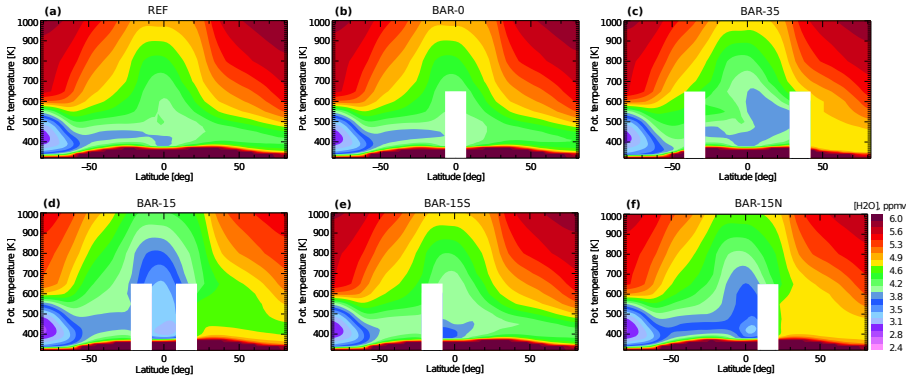

Figure 4.11: Zonal mean H_2O distributions for 2011. Shown data are from the CLaMS sensitivity simulations for the reference (a) and the horizontal transport barrier simulations along latitude circles at 0° (b), 35° N/S (c), 15° N/S (d), 15° S (e) and 15° N (f). Transport barriers are set between the Earth's surface and the 600 K potential temperature levels and are represented in white.

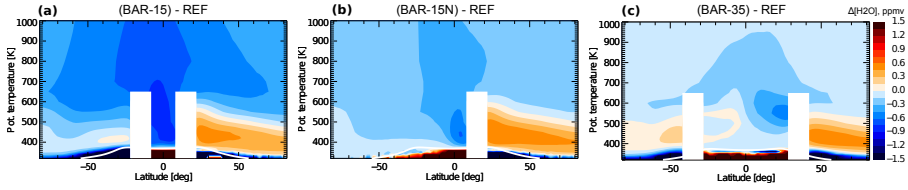

Figure 4.12: Zonal mean H_2O distributions for 2011. Shown are differences between the CLaMS reference simulation and the sensitivity simulations with the horizontal transport barriers at 15° N/S (a), 15° N (b), and 35° N/S (c). Transport barriers are set between the Earth's surface and the 600 K potential temperature levels and are represented in white. Tropopause is presented as white solid line, and is calculated from ERA-Interim reanalysis data.

The model experiments with transport barriers only in the NH or SH subtropics further show that the effect of the NH subtropics in moistening the global stratosphere is stronger compared to the SH subtropics (Fig. 4.12b), although the light moistening from the SH subtropics exists as well (Fig. 4.12a).

Figure 4.13 shows the H_2O seasonal cycle at 400 K and its latitudinal structure, sometimes termed the "horizontal tape recorder" (e.g., Randel et al., 2001; Flury et al., 2013). Consistent with the discussion above, a transport barrier at the equator has only a very weak drying effect on the SH subtropics and mid-latitudes, indicating only a minor role of the NH in moistening the SH lowest stratosphere. Furthermore, the effect of horizontal transport on the SH is small in all simulations as H_2O mixing ratios in the SH are strongly affected by local freeze-drying at SH high latitudes. In the NH, horizontal transport moistens the extratropical LS in summer and dries this region in winter. In the tropics, the annual cycle is related to minimum tropopause temperatures during boreal winter and maximum tropopause temperatures during summer. Therefore, during winter, horizontal transport exports dry air out of the tropics into the NH and moist air during summer. Consequently, the entire annual cycle of the H_2O in the NH extratropical LS is related to horizontal transport from low latitudes, as argued by Ploeger et al. (2013). The boreal summer maxima are related to monsoonal circulations and transport out of the tropics along the eastern and western flanks (Randel and Jensen, 2013).

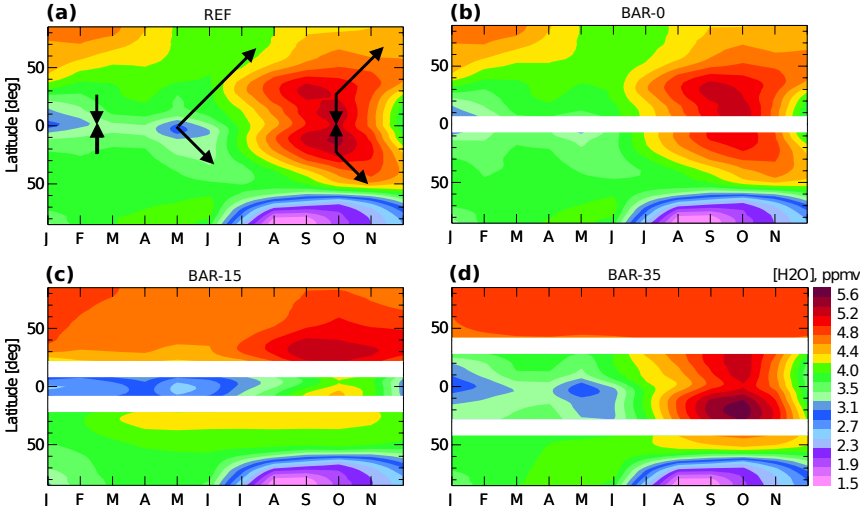

Figure 4.13: Horizontal tape recorder of H_2O at the potential temperature level of $\theta = 400$ K for 2011. Shown data are from CLaMS sensitivity simulations for the reference case (a), and with transport barriers along latitude circles at 0° (b), 15° N/S (c) and 35° N/S (d). Transport barriers are represented in white, and the main directions of air mass transport are presented with black arrows.

4.5 Mixing effects

The PDF of H_2O mixing ratio in Fig. 4.14 shows that increased small-scale mixing in the model generally moistens the LS in the tropics, as well as in the extratropics of both hemispheres. Increased mixing causes both a decrease in the fraction of dry air and an increase in the fraction of moist air, and therefore shifts the PDF to higher mixing ratios. In particular, for the NH extratropics, this effect is strong, substantially enhancing the tail of the PDF with simultaneously reducing the low values in the PDF. The mean H_2O mixing ratio is also increasing towards higher values with increasing mixing strength (dashed lines in Fig. 4.14).

Changes in the parametrized small-scale mixing strength, however, may affect different processes that are critical to the distribution of H_2O in the LS region. Such processes are: diffusive cross-tropopause moisture transport, recirculation of air masses, permeability of the tropical pipe, and vertical diffusion (for illustration see Fig. 4.15). Therefore, interpreting the mixing effects in terms of processes is a challenging task.

Figure 4.16 shows annual zonal mean distributions of H_2O (a-d) and HH (e-h). Similarly, Fig. 4.17 shows double CH_4 mixing ratios (a-d) and AoA (e-h) from the CLaMS simulation without mixing (MIX-no) and their incremental differences between the sensitivity simulations with increasing mixing from the weak mixing case (MIX-weak) through the reference (REF) to the strong mixing case (MIX-strong); i.e. [(MIX-weak) - MIX-no], [REF - (MIX-weak)], and [(MIX-strong) - REF]. Note, that the simulation without small-scale mixing (MIX-no) should not be considered as a realistic case, as turbulent mixing processes always take place in the atmosphere. However, we show the results from this simulation for the sake of completeness when analysing the mixing effects, and for facilitating comparisons with pure trajectory studies (e.g., Fueglistaler and Haynes, 2005; Schoeberl and Dessler, 2011).

A clear response to mixing is found for the LS (below ≈ 430 K), which is moistened with increasing small-scale mixing. In the following, we consider HH above the tropical tropopause as an indicator of changes in transport because it is not affected by chemistry (here CH_4 oxidation). As the moistening in the LS below 430 K is also evident in HH, but not in CH_4 and AoA, it is largely related to enhanced diffusive cross-tropopause transport of moist air. This enhanced diffusive cross-tropopause transport, in turn, increases the probability to by-pass the regions of cold temperatures, rendering the freeze-drying at the tropical tropopause less efficient. Consequently, H_2O entering the stratosphere is enhanced with increased small-scale mixing. The response of HH to changes in mixing is largely independent from the reference mixing strength throughout the stratosphere, with HH always increasing with the increased mixing (Fig. 4.16f, g, h), reflecting the fact that the efficiency of freeze-drying at the tropical tropopause decreases with increasing mixing.

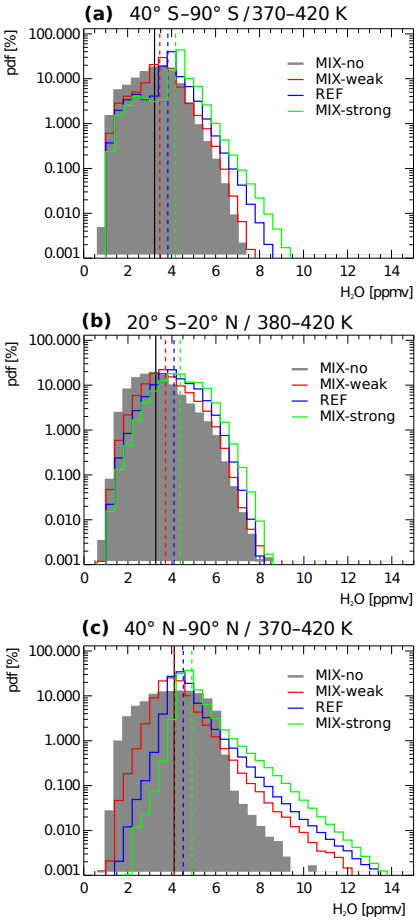

Figure 4.14: PDF for H_2O SH extratropics for 40° S-90° S between 370 K and 420 K (a), in the tropics for 20° S-20° N between 380 K and 420 K (b), and in the NH extratropics for 40° N-90° N between 370 K and 420 K (c). Shown data are from 2011 CLaMS sensitivity simulations with different strength of small-scale mixing for the case without mixing (MIX-no, grey shading background), weak mixing (MIX-weak, red solid line), reference simulation (REF, blue solid line) and strong mixing (MIX-strong, green solid line). Dashed coloured lines represent the mean H_2O values for the different simulations respectively, whereas the black solid line shows the mean value for the non-mixing case.

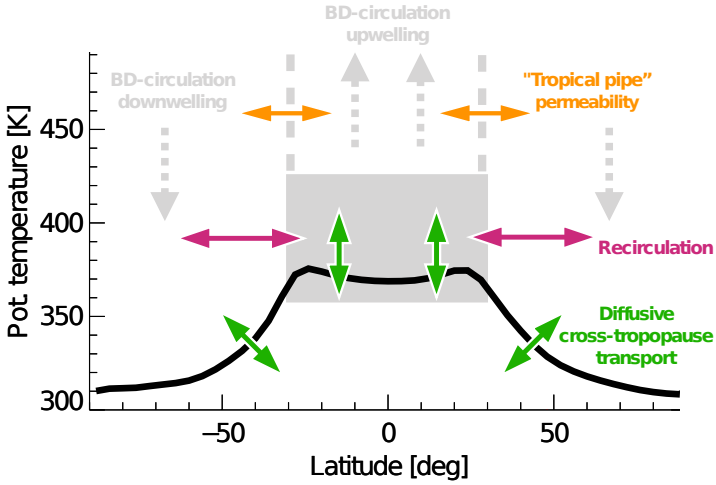

Figure 4.15: A schematic of the processes critical for the distribution of LS H_2O. Grey arrows represent Brewer-Dobson upwelling throughout the tropical region and downwelling towards the poles; green arrows stand for cross-tropopause transport through the whole latitudinal range; the pink arrows represent the region of recirculation of air masses in TTL and the orange arrows show the regions of "tropical pipe" permeability. TTL is represented with solid grey background.

Above about 430 K, the response of the H_2O mixing ratio to varying the mixing strength turns out to be more challenging to interpret, and strongly depends on the reference strength of mixing, due to a complex interplay between horizontal and vertical mixing processes. First, increasing the mixing strength from no-mixing (MIX-no) to weak mixing (MIX-weak) causes significant drying in the NH (Fig. 4.16b). A related signal (above $\approx$430 K in the middle and upper stratosphere) is evident in CH_4 (Fig. 4.17b) and AoA (Fig. 4.17f), but not in HH (Fig. 4.16f). Hence, the drying response in the NH is attributable to transport effects, most likely to an increased permeability of the tropical pipe with increasing mixing, and related an increased transport of dry air, and, also, enhanced CH_4 out of the tropics and into the NH. Second, increasing the mixing strength from weak mixing (MIX-weak) to reference mixing (REF) and from reference mixing to strong mixing (MIX-strong) causes a moister stratosphere globally, related to enhanced diffusive cross-tropopause transport and less efficient freeze-drying (see discussion above). For the former (increasing mixing from MIX-weak), a weak increase of CH_4 in the NH (Fig. f4.17c) indicates a simultaneous increase in the permeability of the tropical pipe. For the latter (increasing mixing from REF), decreasing CH_4 mixing ratios (Fig. 4.17d) and increasing mean age (Fig. 4.17h) throughout the stratosphere likely indicate a simultaneous increase in the strength of recirculation due to increasing mixing.

Figure 4.18 presents a zoom-in view onto the H_2O response to mixing changes in the UTLS

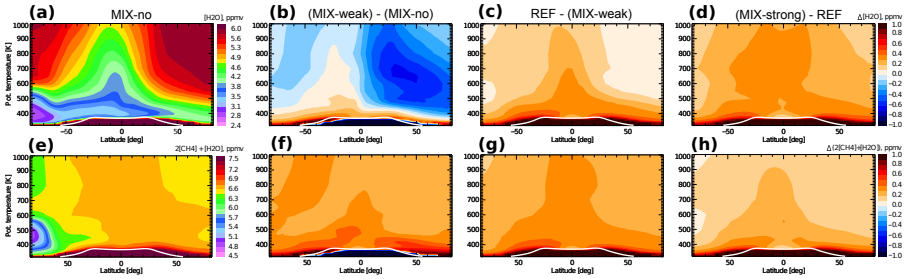

Figure 4.16: Annual zonal mean distributions of H_2O (a) and HH (e) from the CLaMS simulation without mixing (MIX-no), as well as the incremental differences between the sensitivity simulations with increasing mixing from the weak mixing case (MIX-weak) through the reference (REF) to the strong mixing case (MIX-strong); i.e. [(MIX-weak) - MIX-no] in the second column (b, f), [REF - (MIX-weak)] in the third column (c, g), and [(MIX-strong) - REF] in the fourth column (d, h). Tropopause is presented as white solid line, and is calculated from ERA-Interim reanalysis data. The data are shown for 2011.

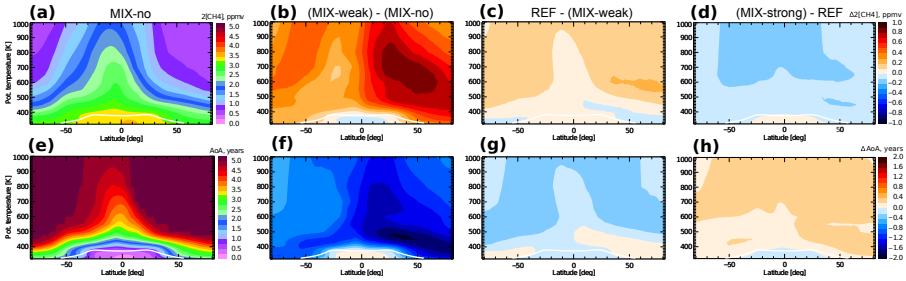

Figure 4.17: Annual zonal mean distributions of $2CH_4$ (a) and AoA (b) from the CLaMS simulation without mixing (MIX-no), as well as the incremental differences between the sensitivity simulations with increasing mixing from the weak mixing case (MIX-weak) through the reference (REF) to the strong mixing case (MIX-strong); i.e. [(MIX-weak) - MIX-no] in the second column (b, f), [REF - (MIX-weak)] in the third column (c, g), and [(MIX-strong) - REF] in the fourth column (d, h). Tropopause is presented as white solid line, and is calculated from ERA-Interim reanalysis data. The data are shown for 2011.

region, a critical region for global climate, for both summer (a, b) and winter (c, d). Clearly, enhanced small-scale mixing moistens the LS due to enhanced diffusive cross-tropopause moisture transport with maximum differences between the simulations of around 20 %. The moistening effects are particularly large in the region around the tropopause where the radiative effect is most sensitive (e.g., Riese et al., 2012). Furthermore, the moistening effect due to mixing is

maximised in the summer hemisphere (Konopka et al., 2007). In the SH, H_2O in the subtropical jet regions appears to be most critical to changes in small-scale mixing. In particular, increasing H_2O mixing ratios in the extratropical lowermost stratosphere causes a flattening of the H_2O isopleths towards high latitudes.

Maps of the H_2O distribution at 380 K for the different CLaMS simulations with different small-scale mixing strength show the regions most prone to mixing changes (Fig. 4.19). Strongest moistening due to increased mixing, occur in the regions of subtropical jets. This is consistent with the findings of Konopka and Pan (2012), where was shown that the subtropical jets are regions of intense mixing. Most intense moistening is always caused by mixing processes along the subtropical jet in the summer hemisphere. During boreal winter, the SH subtropical jet substantially moistens with increasing mixing, whereas during boreal summer, the NH jet moistens. In particular, the moist anomaly of the Asian and American monsoons during boreal summer is affected by small-scale mixing. Without mixing, only a weak anomaly occurs in the Asian monsoon, while the moist anomaly in the American monsoon is absent. With increased mixing, the Asian monsoon moist anomaly first increases (MIX-weak and REF cases). When mixing becomes very strong (MIX-strong) the entire jet region is strongly moistened. Thus, the anomaly of the Asian monsoon relatively to the entire jet region decreases. It should be noted, that the 380 K potential temperature surface may well be located below the tropopause

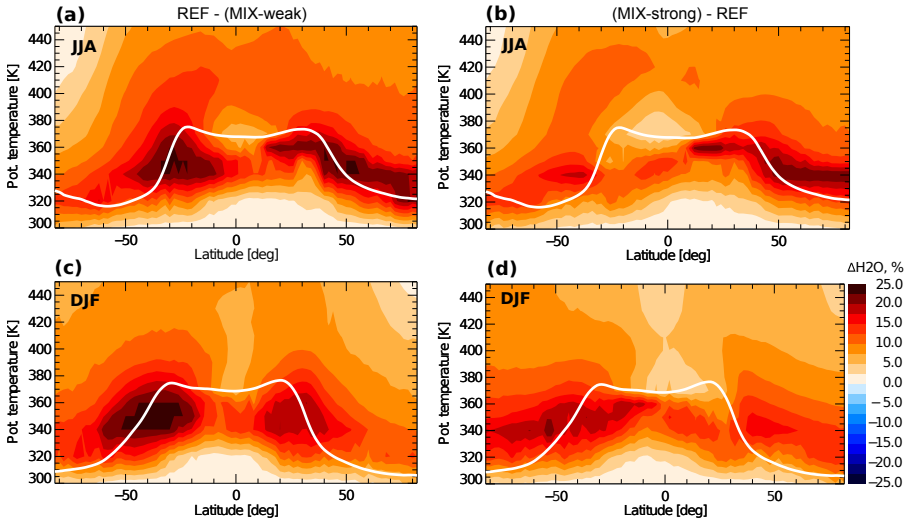

Figure 4.18: Relative differences of zonal mean water vapour for summer (a, b) and winter (c, d) seasons for 2011 between the reference and weak mixing and between the strong mixing and reference case for the LS region. Tropopause is presented with a white solid line, which is calculated from ERA-Interim reanalysis data.

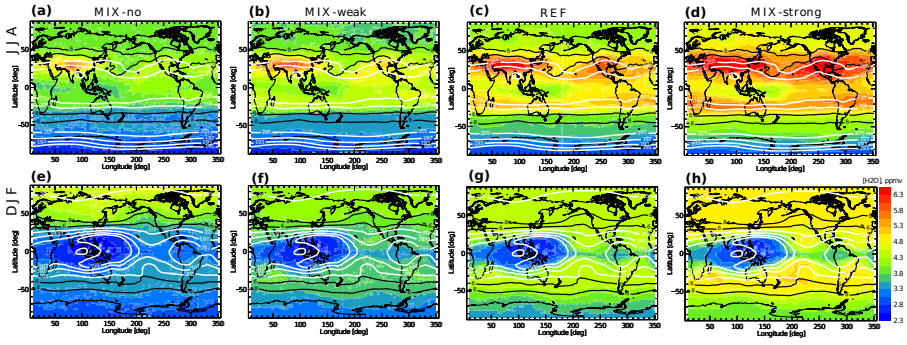

Figure 4.19: Seasonal mean H_2O distribution for 2011 from the CLaMS simulation without mixing (MIX-no) and the sensitivity simulations with non-vanishing mixing strength (MIX-weak, REF, MIX-strong) at the potential temperature level of 380 K; DJF indicates winter (a-d), and JJA summer periods (e-h). Black lines indicate potential vorticity from ERA-Interim reanalysis data (6 PVU, 8 PVU), and the white ones are temperatures (191 K, 193 K, 197 K, 205 K) taken from ERA-Interim reanalysis data.

in the Asian monsoon region such, that parts of the moist anomaly in Fig. 4.19 indicates tropospheric air rather than cross-tropopause transport. However, the response of the subtropical jet and monsoon moist anomalies to increased small-scale mixing remains comparable also at 400K and hence appears to be related to enhanced diffusive upward moisture transport, particularly in regions of strongly deformed zonal flow. Overall, small-scale mixing in the CLaMS simulations and related diffusive cross-tropopause moisture transport seem to be crucial for the development of Asian and American monsoon moisture anomalies, in particular for the American monsoon (where no anomaly occurs without including small-scale mixing).

4.6 Discussion

4.6.1 Comparison of CLaMS simulated and reanalysis stratospheric H_2O

The comparison between the reanalysis own specific humidity products and H_2O simulated with CLaMS driven by the meteorology of the same reanalysis reveals further insights into the control processes of H_2O in the reanalysis. Figure 4.20 shows H_2O mixing ratios in the LS at 380 K for winter and summer, as provided by ERA-Interim and JRA-55 specific humidity. Although the two CLaMS simulations driven by either ERA-Interim or JRA-55 showed differences in the details of the patterns (Fig. 4.8), both simulations agreed reliably well with the satellite observations. The reanalysis H_2O products, on the other hand, show a very different pattern (Fig. 4.20). Despite their success in describing the main dehydration regions in the deep tropics (mainly in the West Pacific, and over South America in boreal winter), they fail in representing the main moisture sources in the Asian and American monsoons during summer. ERA-Interim,

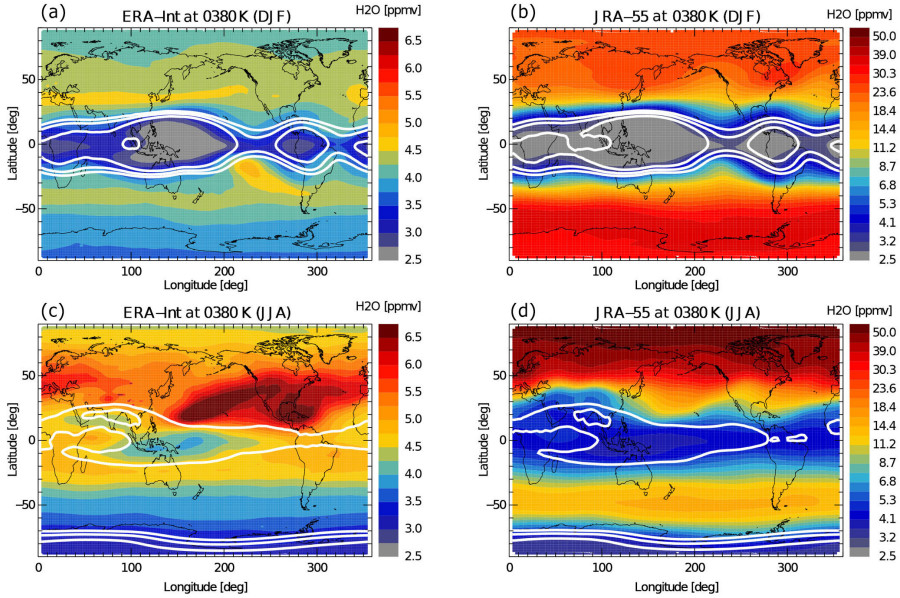

Figure 4.20: Seasonal mean H_2O distribution averaged over the period from 2004 to 2013 at the potential temperature level of 380 K; DJF indicates winter (a, b), and JJA summer periods (c, d). Shown data are from both reanalysis, ERA-Interim and JRA-55 reanalysis data. The white lines are constant temperature levels from corresponding reanalysis datasets (191 K, 193 K, 195 K). Note the logarithmic colour bar for JRA-55.

for instance, shows highest summertime H_2O mixing ratios above the Pacific.

The clearest difference to MLS and CLaMS, however, occurs for JRA-55 H_2O in the middle and high latitude LS. In this region, JRA-55 H_2O mixing ratios are about one order of magnitude higher than for ERA-Interim. A similar result was recently noticed by Davis et al. (2017), suggesting that JRA-55 strongly overestimates the amplitude of the seasonal H_2O cycle, although this result depends on the considered level. Remarkably, using the reanalysis temperature and wind fields to drive CLaMS transport, our results show a good agreement of H_2O distributions with MLS observations. Note, that in CLaMS the calculation of stratospheric H_2O is based on the CLaMS cirrus dehydration scheme based on the Clausius-Clapeyron relation and simplified fall-out of ice particles (see Sect. 3.1.3) and is, therefore, largely related to the large-scale reanalysis temperature and wind fields. The different CLaMS simulations also show a moister stratosphere for JRA-55, compared to ERA-Interim, consistent with a warmer tropical tropopause in JRA-55, but with much smaller differences than for the reanalysis H_2O products. Although both reanalysis assimilation systems are constrained by observational data to produce realistic temperatures, significant differences around the tropical tropopause still exist of about 2 K (see

Sect. 4.3). But these differences are not sufficient to explain the H_2O differences between the reanalysis products, as presented in Fig. 4.20. Hence, the reanalysis own H_2O products seem not consistent with the simple Clausius-Clapeyron relation.

Figure 4.21 shows H_2O PDFs for further insights into the processes causing the difference between ERA-Interim and JRA-55 H_2O in the NH extratropical LS. Both CLaMS simulations, driven with either ERA-Interim or JRA-55 data, and ERA-Interim reanalysis H_2O products show a skewed PDF with a tail at high values, particularly strong in boreal summer. JRA-55 H_2O mixing ratios, on the contrary, show a PDF with a totally different shape and a much higher mean value by about a factor of 5. This behaviour is clearest at around 370 K (Fig. 4.21), but it is also visible at levels below and above (not shown). The different shape of the JRA-55 PDFs with the peak at much higher mixing ratios suggests that high H_2O mixing ratios are deposited in the extratropical LS, from potential temperature levels of about 350 K up to at least about 400 K, which is potentially related to the convective scheme in the reanalysis. JRA-55 shows a higher frequency of high and optically thick clouds, when compared with the ERA-Interim (e.g., Kang and Ahn, 2015; Kobayashi et al., 2015; Tompkins et al., 2007), which might also indicate

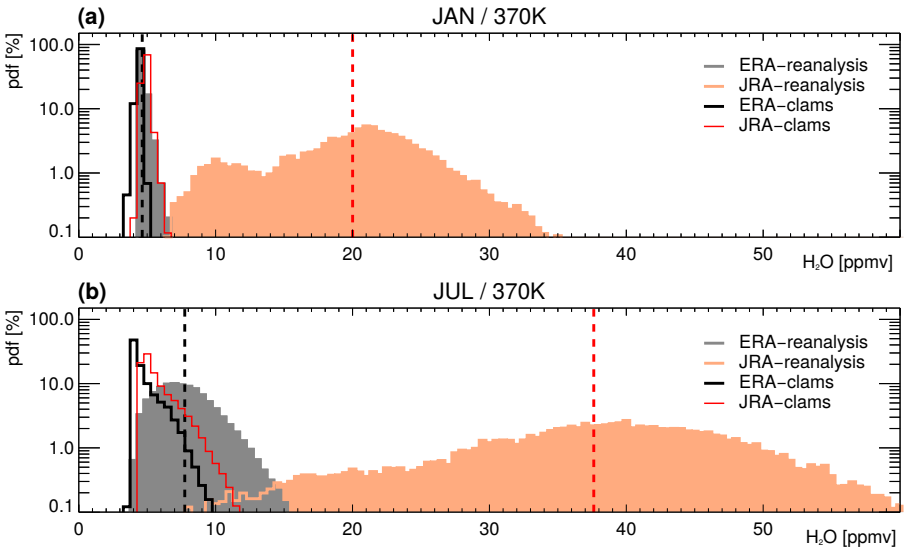

Figure 4.21: PDF of H_2O mixing ratio for 2011, at the potential temperature level of 370 K in the NH for middle and high latitudes (50°-90° N). The distribution is presented for January (a) and July (b). Shown data are taken from ERA-Interim (grey line) and JRA-55 (orange line) reanalysis data. CLaMS H_2O driven by ERA-Interim (black line) and JRA-55 (red line) is shown for comparison. Vertical dashed lines are the mean values of the reanalysis data respectively, black one of ERA-Interim, red one is JRA-55 reanalysis products.

a critical role of differences in convection for causing the differences in H_2O (e.g., Folkins and Martin, 2005; Sherwood et al., 2010).

Recent studies have emphasised the overall qualitatively positive agreement between the large-scale climatological features in the UTLS in different reanalysis datasets, however, important quantitative differences remain (e.g., Manney et al., 2017). This qualitative agreement among the reanalysis in many regions of the UTLS and different seasons points to the robustness of the representation of related transport and chemistry in the reanalysis datasets (Manney and Hegglin, 2018). As the stratospheric H_2O in the reanalysis is not assimilated directly, the treatment of H_2O in the particular reanalysis product plays an important role. For instance, JRA-55 does not contain a parametrization of CH_4 oxidation in contrary to ERA-Interim (Davis et al., 2017). Davis et al. (2017) further showed that the JRA-55 mean H_2O values are much too large at 100 hPa. Our results of excessively high H_2O values in the JRA-55 data product in the extratropical LS agree well with the findings of Davis et al. (2017). Furthermore, Davis et al. (2017) points out that there is still a lack of assimilated observations and that significant uncertainties remain in the representation of the relevant physical processes in the reanalysis.

4.6.2 Vertical diffusivity induced by small-scale mixing

Although, it is clear qualitatively that a decreasing critical Lyapunov exponent enhances mixing, it is also desirable, at least for comparison purposes, to quantify this effect. Because of the similarity between the mixing procedure in CLaMS and physical diffusion, the vertical mixing intensity can be quantified by computing the induced vertical diffusivity K_z (in m^2/s) (Konopka et al., 2007). We estimated K_z for each AP in CLaMS following Konopka et al. (2007), i.e.:

$$K_z = c\frac{\Delta z^2}{\Delta t}, \tag{4.1}$$

if mixing occurs during Δt time step; and $K_z = 0$, if mixing did not happen. Here Δz is the model layer depth (in meters), $\Delta t = 1$ day is the mixing time step, and c is taken to be $1/24$ to account for the random position of the APs within the layer. The average diffusivity can be computed as mean of the local diffusivity of the APs.

In the tropical LS (between 380 K and 420 K), we estimate the vertical diffusivity of the simulations with critical Lyapunov exponent $2.0\,day^{-1}$ (MIX-weak), $1.5\,day^{-1}$ (REF), and $1.0\,day^{-1}$ (MIX-strong) to be respectively $0.005\,m^2/s$, $0.02\,m^2/s$, and $0.065\,m^2/s$ (Fig. 4.22). The range of about one order of magnitude difference for the parametrized K_z in the tropical LS matches the uncertainty in that coefficient (e.g. Podglajen et al., 2017). Indeed, the value parametrized in the reference run (REF) is similar to the one estimated by Mote et al. (1998) ($0.02\,m^2/s$) from satellite tracer measurements, or to the results from a recent study by Podglajen et al. (2017) based on small-scale in-situ wind measurements. Glanville and Birner (2017) rather suggest an average K_z of $0.08\,m^2/s$, which is closer to the value in the MIX-strong simulations.

Figure 4.22 also shows the annual average H_2O concentration in the tropical LS as a function of the estimated annual average K_z in the same region. The increase of vertical diffusivity by approximately one order of magnitude, from MIX-weak to MIX-strong, results in a moistening of about 0.6 ppmv. This sensitivity is of the same order as suggested by Ueyama et al. (2015), although those authors varied the diffusivity by 2 orders of magnitude (from $0.001\,m^2/s$

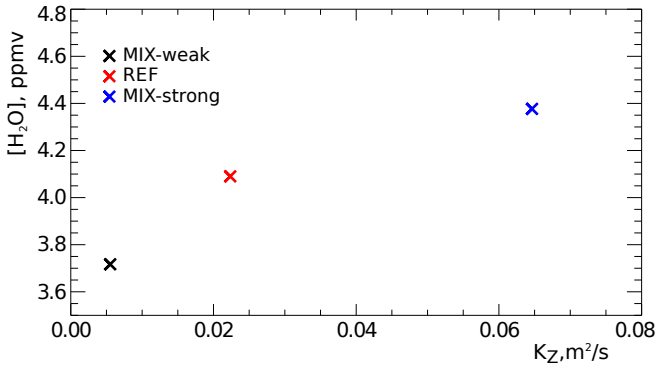

Figure 4.22: Distribution of H_2O as a function of the average vertical diffusivity coefficient (K_z) in the simulations with different small-scale mixing strength. The data are annual mean values spatially averaged over the 380 K to 420 K potential temperature and 20° S-20° N latitude region from different sensitivity simulations with respect to small-scale mixing (for 2011). Black cross represents weak mixing (MIX-weak, $\lambda_c = 2.0\,\mathrm{day}^{-1}$), red shows reference (REF, $\lambda_c = 1.5\,\mathrm{day}^{-1}$) and blue cross strong mixing (MIX-strong, $\lambda_c = 1.0\,\mathrm{day}^{-1}$) cases.

to 0.1 m^2/s) and found a moistening effect of around 0.5 ppmv. The discrepancy might be partly due to the non-linear dependence of mean H_2O on diffusivity; although there are only three points in Fig 4.22, the impact of increasing vertical diffusivity appears to saturate, which is probably due to the limitation of transport effects by dehydration.

Finally, it should be noted that the mixing in CLaMS induces both vertical and horizontal diffusion. However, given the larger vertical gradients of H_2O compared to horizontal gradients in the UTLS, the impact of small-scale horizontal diffusion is assumed to be much smaller than the impact of vertical diffusion, especially in the tropics.

4.7 Chapter conclusions

We investigated the sensitivities of modelling H_2O in the LS region regarding different reanalysis datasets, horizontal transport between tropics and extratropics, and small-scale mixing, using the Lagrangian transport model CLaMS.

Differences in H_2O between CLaMS model simulations driven by ERA-Interim and JRA-55 reanalysis amount to about 0.5 ppmv throughout the stratosphere. This demonstrates a substantial uncertainty in simulated H_2O, even when using the recent reanalysis products. This uncertainty in simulated H_2O results mainly from differences in temperatures between the reanalysis products around the tropical tropopause, indicating that tropopause temperatures in the current reanalysis datasets are not sufficiently constrained.

Sensitivity simulations with introduced artificial transport barriers in the model to suppress

certain horizontal transport pathways shows that the overall effects of interhemispheric transport is weak and insignificant for stratospheric H_2O. Furthermore, our results suggest that the NH subtropical region is a critical source region of moisture for the global stratosphere, which is likely related to the subtropical monsoon circulations. A comparison of the tropical entry H_2O from the sensitivity 15° N/S barrier run, and the reference case shows differences of up to around 1 ppmv. Hence, a reliable representation of processes in the subtropics in global models turns out to be critical for simulating stratospheric H_2O and its climate effects.

Changing the strength of small-scale mixing in CLaMS shows that increased mixing causes moistening of the stratosphere by enhanced diffusive moisture transport across the tropopause. For the sensitivity simulation with varied mixing strength differences in tropical entry H_2O between the weak and strong mixing cases amount to about 1 ppmv, with small-scale mixing enhancing H_2O in the LS. Interestingly, the impacts of the horizontal transport processes and small-scale mixing are of the same order of magnitude. The strongest mixing effects occur around the subtropical jets in the respective summer hemisphere. In particular, the Asian and American monsoon systems during boreal summer turn out as regions especially sensitive to changes in small-scale mixing, which appears crucial for controlling the moisture anomalies in the monsoon UTLS. Above about 430 K, increased mixing causes a complex interplay between vertical and horizontal mixing, which results in either moistening or drying of the stratosphere depending on the mixing strength. Therefore, the interpretation of differences in simulated H_2O from models in terms of differences in numerical diffusion is a problematic task. The results from our sensitivity simulations help to interpret the uncertainties of simulated stratospheric H_2O and to identify deficits in various climate models.

Chapter 5

Estimating BDC trends from stratospheric H_2O changes: sensitivity of the method

The trace gas distribution in the LS is largely controlled by influx from the troposphere and by the BDC, which consists of the mean meridional mass circulation and additional eddy mixing (Butchart, 2014; Ploeger et al., 2015a; Ploeger and Birner, 2016). Thus, any changes in the strength or pattern of the BDC may cause a response in trace gas concentrations and in their trends (e.g., Butchart and Scaife, 2001; Bunzel and Schmidt, 2013). Therefore, a correct representation of changes in the BDC is crucial for accurate and reliable future climate predictions.

Climate model simulations generally show strengthening of the BDC with global warming, due to increasing greenhouse gases (e.g., Sigmond et al., 2004; Butchart et al., 2006; Li et al., 2008). An intensification of the BDC is caused mainly by enhanced extratropical wave forcing in the middle atmosphere via the "downward control" principle (Haynes et al., 1991), with contributions from both planetary and gravity waves (e.g., Butchart et al., 2010).

Here, following Schoeberl et al. (2000), we consider a sample of atmospheric air as a statistically robust ensemble of irreducible APs. Such APs may take different paths to arrive at the sampling volume. The AoA for such an ensemble of APs can be interpreted as the mean of the transit time distribution, which is possible to compute following Eulerian (Hall and Waugh, 1997) or Lagrangian (Schoeberl et al., 2000) calculations. Mean age of air (AoA) can be used to study stratospheric circulation and transport (Schoeberl et al., 2000; Ploeger and Birner, 2016). Moreover, mean age of stratospheric air is commonly used as a measure for the strength of the BDC (e.g., Waugh and Hall, 2002).

Garcia et al. (2011) pointed out, that the AoA is difficult to estimate from stratospheric observations, as they do not include the time history of the air explicitly. However, under some conditions, it is possible to infer AoA from the trace gas concentrations (e.g., Hall and Plumb, 1994; Strunk et al., 2000; Engel et al., 2009). Suitable species are so-called "clock tracers"[1], like SF_6 or CO_2, which contain the information about the time along a parcel path from the source to

[1] **Clock tracer** is a trace gas with a linearly increasing source (Schoeberl et al., 2005).

the point of observation. The first convenient example of such a clock tracer is an inert tracer[2] with a monotonically increasing source. A second example concerns species with the source constant in time but chemically decaying (Schoeberl et al., 2000). Such thoughts were followed by many research groups (e.g., Engel et al., 2009; Ray et al., 2014), to diagnose AoA and the evolution of the BDC. There is also evidence, that the patterns of some other trace gas species, such as CH_4 or N_2O, are dominated by the BDC transport (e.g., Holton, 1986; Plumb and Ko, 1992).

5.1 Theory of the mean age of air (AoA)

It is challenging to define the AoA directly from the trace gas concentration, as parcels with the same age can arrive to the observation point through different paths (Schoeberl et al., 2000). So, it is not straightforward to diagnose circulation only from a chemical trace gas time series. In general, the mixing ratio of any long-lived trace gas, $\chi(r,\ t)$, at a specific time and specific location in the stratosphere can be expressed as the following integral over all the past times

$$\chi_{[strat]}(r,\ t)\ =\ \int_{-\infty}^{t} \chi(r_0,\ t_0)\ G(r,\ t\mid r_0,\ t_0)\ L(r,\ t-t_0)\ dt_0, \tag{5.1}$$

where $\chi(r_0,\ t_0)$ is the tropospheric time series of the source at the stratospheric entry; $G(r,\ t\mid r_0,\ t_0)$ is the boundary propagator (or Green's function of the transport operator); $L(r,\ t-t_0)$ is a function, describing the chemical loss of the trace gas during the transit time $t'=t-t_0$, where t_0 is a source time[3], and t is a field time[4] at the sampling volume.

So, the stratospheric tracer distribution can be described through the contributions of tropospheric growth, chemical sinks (assuming there are no chemical sources), and transport. Notably, a loss function L, is an average loss factor of all irreducible elements that took paths with transit time t' from the point of stratospheric entry to the r point of a sampling volume (Volk et al., 1997; Waugh and Hall, 2002). In general, a loss function should depend on the path spectra[5]. Only tracers with constant tropospheric values and constant radioactive decay within the stratosphere are path independent (Hall and Plumb, 1994).

Assuming the absence of integrated loss, $L(r,\ t')\ =\ 1$, the Eq. 5.1 can be rewritten (Hall and Plumb, 1994; Waugh and Hall, 2002)

$$\chi_{[strat]}(r,\ t)\ =\ \int_{-\infty}^{t} \chi(r_0,\ t_0)\ G(r,\ t\mid r_0,\ t_0)\ dt_0. \tag{5.2}$$

[2]**Inert tracer** – inert trace gas, which does not take part in chemical processes.

[3]**Source time** – the time, when the tracer was the last time in contact with the source at the position r_0 (Ploeger and Birner, 2016).

[4]**Field time** – the time when the tracer mixing ratio is sampled.

[5]**Path spectra** are all pathways from the entrance region, or tropical tropopause, to the specific location in the stratosphere (e.g., Holzer and Hall, 2000; Remsberg, 2015).

If we replace the initial times with transit times (means $t_0 = t - t'$), we get

$$\chi_{[strat]}(r,\, t) \;=\; \int_0^\infty \chi(r_0,\, t-t')\; G(r,\, t \mid r_0,\, t-t')\; dt'. \tag{5.3}$$

Here, G is interpreted as transit time distribution (or "age spectrum"); and it is the probability, that the transit time of the air parcel travelling from the source r_0 to the sample point r is in the range between t' and $t' + dt'$. Moreover, the age spectrum fulfils the normalization condition

$$\int_0^\infty G(r,\, t \mid r_0,\, t-t')\; dt' \;=\; 1. \tag{5.4}$$

The AoA is the first moment of the age spectrum

$$\tau(r,\, t) \;=\; \int_0^\infty t'\; G(r,\, t \mid r_0,\, t-t')\; dt'. \tag{5.5}$$

For CH_4 and H_2O in the stratosphere, the complications due to non-conservation can be solved by considering HH (see Eq. 2.15)

$$\mathrm{HH}_{[\mathrm{strat}]} = \mathrm{H_2O}_{[\mathrm{strat}]} \;+\; 2\;\mathrm{CH_4}_{[\mathrm{strat}]}. \tag{5.6}$$

As HH is nearly constant in the lower and middle stratosphere, it can be treated as a conserved tracer when investigating this region. Note that the variations in HH entry mixing ratios are dominated by variations in H_2O (Fueglistaler, 2012). Thus, the time series of HH in the lower and middle stratosphere away from regions of dehydration (in particular the Antarctic polar vortex), is a time series of HH at entry into the stratosphere convolved with the age spectrum at the given location (Waugh and Hall, 2002), and can be described with the relation 5.3. The usage of the combination of CH_4 and H_2O was suggested by Fueglistaler (2012) for circulation change investigations.

Thus, it is a complicated task to evaluate accurately AoA from the trace gas distribution. Consequently, approximations are often used (e.g., Schoeberl et al., 2000, 2005; Hegglin et al., 2014). In this work, we consider the applicability of two common assumptions for estimating the AoA trend: (I) instantaneous propagation of the stratospheric entry mixing ratio $\chi_{[strat]}(r,\, t)$, and (II) stationarity of the correlation between AoA and the CH_4 fractional release factor. Below, we present the effects of these assumptions on the trends of stratospheric H_2O distribution and the AoA, in order to investigate the changes in the BDC.

5.2 Methodology of estimating AoA trends from stratospheric H_2O changes

Our investigation is motivated by the work of Hegglin et al. (2014), describing a method for merging H_2O satellite data. Through the changes in measured stratospheric H_2O, Hegglin et al. (2014) estimated AoA trends, which show evidence for an accelerating BDC in the lower stratosphere (Fig. 5.1). Note that the usage of words "trend" or "change" is similar in the context of

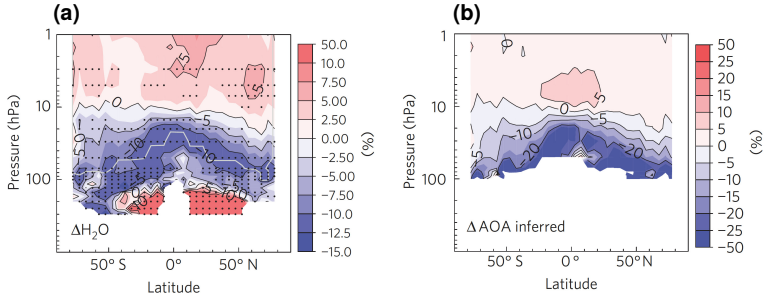

Figure 5.1: Long-term changes in stratospheric H_2O (a) shown as percentage changes from the merged satellite record since 1986/1988 (above/below grey line) up to 2010. Dots indicate the 95%-significance level. The plot (b) represents AoA changes estimated from changes in the CH_4 fractional release factor. (The figure is adapted from Hegglin et al., 2014).

this thesis, with "trend" describing changes over longer than 10 years.

The methodology for estimating the drivers to stratospheric H_2O changes and inferred AoA trends, introduced by Hegglin et al. (2014), is described below.

5.2.1 Drivers of H_2O changes

It has been suggested to use HH for extracting the information about stratospheric circulation (e.g., Dessler et al., 1994; Fueglistaler et al., 2013; Hegglin et al., 2014). HH is approximately conserved in the lower and middle stratosphere (LeTexier et al., 1988; Dessler et al., 1994). Note that HH is not conserved in the polar regions or in the TTL, where dehydration occurs (see Sect. 2.4.1, Appendix B).

As pointed out before, stratospheric H_2O has two main sources: H_2O transported upward through the cold TTL by the BDC, and CH_4 oxidation (mainly in the middle and high stratosphere). Thus, the full H_2O mixing ratio in the sampling volume in the stratosphere at the specific location r and time t is:

$$H_2O_{[\mathrm{strat}]}(r,\,t) = H_2O_{[\mathrm{entry}]}(r,\,t) + 2\alpha(r,\,t)\;CH_{4\,[\mathrm{entry}]}(r,\,t), \tag{5.7}$$

where $H_2O_{[\mathrm{entry}]}(r,\,t)$ and $CH_{4\,[\mathrm{entry}]}(r,\,t)$ are the H_2O and CH_4 mixing ratios respectively, at the specific time and location in the stratosphere, transported from the stratospheric entry (in the TTL) without any chemical effects; α is the fractional release factor (FRF).

FRF describes the fraction of CH_4 which has been dissociated in the stratosphere (Solomon and Albritton, 1992). The FRF is equal to 0 at the entry to the stratosphere. Then the air mass following the stratospheric circulation, moves through different pathways and CH_4 molecules and gets dissociated. The reactions of CH_4 with $O(^1D)$, OH, and Cl, cause CH_4 loss in the

stratosphere (see Reactions 2.3, 2.4, 2.5). FRF increases until it reaches the value of 1, when CH_4 is completely depleted (e.g., Ostermöller et al., 2017). Thus, FRF shows the effectiveness of CH_4 breaking down in the stratosphere. Analogously, FRFs can be defined for ozone depleting substances (e.g., Laube et al., 2010). The FRF distribution changes with atmospheric conditions, in particular, stratospheric dynamics or photochemistry.

The full CH_4 mixing ratio is equal to the difference between CH_4 transported from the TTL and dissociated CH_4

$$\mathrm{CH_{4\,[strat]}}(r,\,t) = [1-\alpha(r,\,t)]\;\mathrm{CH_{4\,[entry]}}(r,\,t), \tag{5.8}$$

Based on Eq. 5.7 and Eq. 5.8, it is possible to infer the information about stratospheric circulation changes from long-term H_2O trends (Hegglin et al., 2014).

Considering the change at the fixed location in the stratosphere, the full derivative of $\mathrm{H_2O_{[strat]}}(r,\,t)$ from Eq. 5.7 is

$$\begin{aligned} d\mathrm{H_2O_{[strat]}}(r,\,t) = \\ \frac{\partial \mathrm{H_2O_{[entry]}}(r,\,t)}{\partial t}dt + 2\alpha(r,\,t)\frac{\partial \mathrm{CH_{4\,[entry]}}(r,\,t)}{\partial t}dt + 2\mathrm{CH_{4\,[entry]}}(r,\,t)\;\frac{\partial \alpha(r,\,t)}{\partial t}dt. \end{aligned} \tag{5.9}$$

Integrating Eq. 5.9 over a finite time period Δt, we can describe changes in stratospheric H_2O as

$$\begin{aligned} \Delta\mathrm{H_2O_{[strat]}}(r,\,t) = \\ \Delta\mathrm{H_2O_{[entry]}}(r,\,t) + 2\alpha(r,\,t)\;\Delta\mathrm{CH_{4\,[entry]}}(r,\,t) + 2\mathrm{CH_{4\,[entry]}}(r,\,t)\;\Delta\alpha(r,\,t). \end{aligned} \tag{5.10}$$

During a time period with constant stratospheric entry mixing ratio in the TTL, the time dependence vanishes

$$\mathrm{H_2O_{[entry]}}(r,\,t) = \mathrm{H_2O_{[entry]}}(r_0), \tag{5.11}$$

$$\mathrm{CH_{4\,[entry]}}(r,\,t) = \mathrm{CH_{4\,[entry]}}(r_0), \tag{5.12}$$

where r_0 is the location at the stratospheric entry (mainly TTL). For simplicity, hereafter, we denote the mixing ratio of the trace gas $\chi_{[entry]}(r_0)$ as $\chi_{[entry]}$.

In this way, the changes in stratospheric H_2O can be rewritten via changes in the stratospheric H_2O entry mixing ratio ($\mathrm{H_2O_{[entry]}}$), changes in the stratospheric CH_4 entry mixing ratio ($\mathrm{CH_{4\,[entry]}}$), and changes in the FRF which, in turn, represents changes in stratospheric circulation and thus, the changes in the BDC:

$$\begin{aligned} \Delta\mathrm{H_2O_{[strat]}}(r,\,t) = \\ \Delta\mathrm{H_2O_{[entry]}} + 2\alpha(r,\,t)\;\Delta\mathrm{CH_{4\,[entry]}} + 2\mathrm{CH_{4\,[entry]}}\Delta\alpha(r,\,t). \end{aligned} \tag{5.13}$$

The contribution from $\mathrm{H_2O_{[entry]}}$ (first term in Eq. 5.13) in the work of Hegglin et al. (2014) was calculated from merged satellite data. The contribution from $\mathrm{CH_{4\,[entry]}}$ and circulation changes (second and third terms in Eq. 5.13) were estimated using stratospheric observations of CH_4 from ACE-FTS, HALOE (see Sec. 3.3), and MIPAS, complemented with the tropospheric flask measurements at Mauna Loa. In the work of Hegglin et al. (2014), the changes in

the stratospheric quantities $\Delta\chi_{[entry]}$, were calculated as a difference between their mixing ratios during the first and the last year of the investigated period.

For deducing α, which is needed for Eq. 5.13, the relation 5.8 with assumption 5.12 can be used. Thus, FRF can be estimated as

$$\alpha(r,\, t) \;=\; 1 - \mathrm{CH_4}_{[\mathrm{strat}]}(r,\, t)/\mathrm{CH_4}_{[\mathrm{entry}]}, \tag{5.14}$$

where $\mathrm{CH_4}_{[\mathrm{strat}]}(r,\, t)$ is the stratospheric CH_4 mixing ratio. Hegglin et al. (2014) used CH_4 mixing ratios averaged over 2005-2006 as $\mathrm{CH_4}_{[\mathrm{strat}]}(r,\, t)$. This specific period is characterised by relatively constant tropospheric CH_4 values. Accordingly, the dependence of stratospheric CH_4 entry mixing ratios on transit time can be neglected, and $\mathrm{CH_4}_{[\mathrm{strat}]}$ can be assumed constant over these years. The stratospheric CH_4 in this case is a fraction of the tropospheric CH_4, which is a function of latitude, height and season (Remsberg, 2015). The air needs some years to be transported through the stratosphere, and following Hegglin et al. (2014), stratospheric CH_4 during 2005-2006 originates in the TTL during approximately 2002-2006. So, $\mathrm{CH_4}_{[\mathrm{entry}]}$ can be calculated as a mean over the 2002-2006 period. Consequently, FRF is the same for any year.

As a remark, Ostermöller et al. (2017) pointed out that FRF is highly time dependent. Although, the widely used "current" formulation of FRF (e.g., Newman et al., 2007; Laube et al., 2013) considered it to be a time independent quantity, which depends only on the location in the stratosphere (see also Eq. 5.14). Ostermöller et al. (2017) showed that the tropospheric trend of the species has an impact on the derived FRF and may cause its time dependency. For species, like N_2O, with a small linear tropospheric trend (about 0.2 % per year), the previous formulation of FRF works well and does not need any correction for the tropospheric trend. For the species, like CFC-11 or CFC-12, with a high (above 6 % per year) tropospheric trend, FRF is strongly time dependent, and the new formulation of FRF with the correction for tropospheric trends, proposed by Ostermöller et al. (2017), should be used.

Further, in our study, we use CLaMS stratospheric entry CH_4 for calculating FRF. Following Ostermöller et al. (2017), we can estimate the impact of CH_4 tropospheric trend on the FRF, by comparing CLaMS CH_4 tropospheric trend to the CLaMS N_2O tropospheric trend (because N_2O was considered in Ostermöller et al., 2017). Figure 5.2 shows the time series of CLaMS CH_4 (a) and CLaMS N_2O (b) mixing ratios at the entry into the stratosphere (averaged over the tropics 30° S-30° N between 390-400 K) for 1979-2017. The red line shows the steepest trend during the investigated period, from 1990 to 2017. The yearly trend of CLaMS CH_4 (0.48 % per year) is comparable with CLaMS N_2O trend (0.26 % per year, which is similar to the one published by Ostermöller et al., 2017). So, the effect of CLaMS CH_4 TTL trend on further estimated FRF will be negligible. Thus, the FRF calculation does not require any corrections for the tropospheric CH_4 trend. Consequently, any trend in the estimated FRF from CLaMS CH_4 is related to the changes in stratospheric dynamics.

Assuming conservation of HH, the third term in Eq. 5.13, which is attributed to changes in FRF, can be calculated as a difference between the full changes in stratospheric H_2O and a sum of the two first terms.

$$\begin{aligned} 2\mathrm{CH_4}_{[\mathrm{entry}]}\Delta\alpha(r,\, t) = \\ \Delta\mathrm{H_2O}_{[\mathrm{strat}]}(r,\, t) - (\Delta\mathrm{H_2O}_{[\mathrm{entry}]} + 2\alpha(r,\, t)\,\Delta\mathrm{CH_4}_{[\mathrm{entry}]}). \end{aligned} \tag{5.15}$$

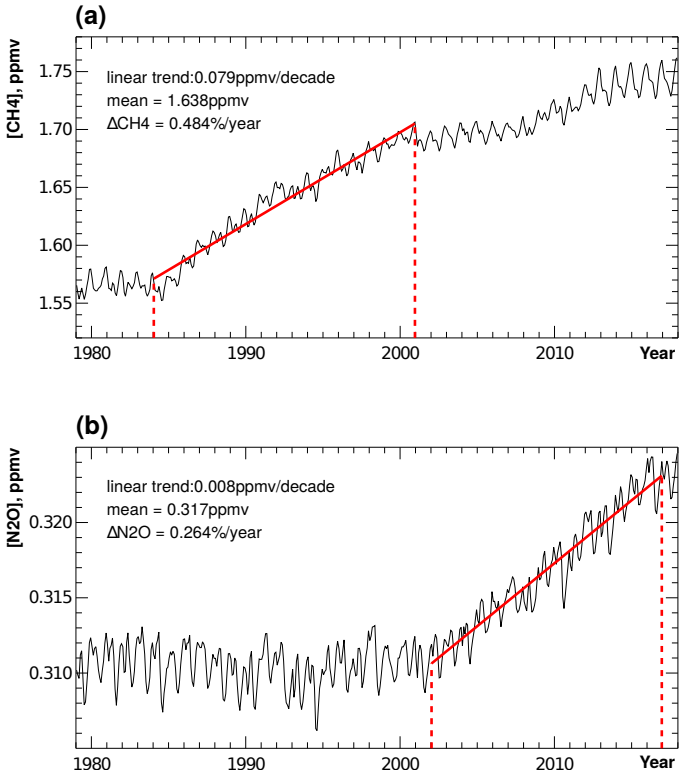

Figure 5.2: Evolution of CH_4 (a) and N_2O (b) mixing ratios averaged in the tropics 30°S-30°N at the potential temperature level between 390-400 K, for 1979-2017. The shown data is from CLaMS simulation driven by ERA-Interim reanalysis. For CLaMS, the boundary conditions at the surface are prescribed based on ground-based measurements in the lowest model level (below ≈ 4 km). For CH_4 from 1983 to 2011 it is taken from zonally-symmetric NOAA/CMDL dataset, for 2011-2017 it is taken from zonally-resolved AIRS data. For N_2O boundary was used zonally-symmetric NOAA/CATS long term observations for 1999-2017. For the periods not covered by the measurements, the boundary mixing ratios were prescribed repeatedly to the mixing ratio values of the first year where measurement data are available (for the detailed description follow Pommrich et al., 2014). The red line at the Figure shows the periods of the steepest slope, which indicates the highest trend. Thus, for CH_4 this period is defined between 1984-2000, and for N_2O is it 2002-2016. Also, the mean mixing ratio values are indicated at each Figure for every species during this period, as well as the highest percentage trend per year with the relation to the mean value.

Thus, the third term represents the effect of changes in stratospheric circulation caused by stratospheric H_2O changes.

Consequently, using the above approach, it is possible to define the separate drivers of H_2O changes in the stratosphere, related to changes in stratospheric H_2O entry mixing ratio, changes in CH_4 entry mixing ratio, and changes in the FRF. As $\Delta\alpha$ represents a change in stratospheric circulation (which, in turn, is related to changes in the BDC), it is possible to estimate from $\Delta\alpha$ the changes in the AoA.

5.2.2 Assessing AoA trends from H_2O changes

The approximate relationship AoA = $f(\alpha)$, with f an empirically determined function, taken from the correlation between calculated FRF and aforehand known modelled AoA, leads to approximate estimation of AoA changes. This relationship is needed for translation of the inferred α changes (caused by stratospheric H_2O trend) into AoA changes. The AoA trend can be estimated as

$$\Delta\text{AoA} = f(\alpha + \Delta\alpha) - f(\alpha). \tag{5.16}$$

Hegglin et al. (2014) proposed a third-order polynomial function, constant in time, as a good fitting function for the correlation between FRF and modelled AoA.

5.2.3 Research strategy

In the following we consider the consequences of the two major approximations in the method introduced above:

- instantaneous propagation of stratospheric entry H_2O and CH_4 mixing ratios,
- constant correlation (stationary relationship) between FRF and modelled AoA.

In turn we evaluate the effects of these approximations on the AoA trends inferred from H_2O changes through comparison of the "true" (actual model CLaMS) AoA trends with the AoA trends estimated with the approximation methods. For this, we perform sensitivity studies

Method	**Abbreviation**	**Propagation of entry CH_4 and/or H_2O**	**Time-varying AoA-FRF correlation**
Reference ("true" CLaMS)	REF	–	–
Approximation	APPROX	no	no
Constant correlation	C-CORR	yes	no
Full reconstruction	FULL	yes	yes

Table 5.1: Sensitivity studies with respect to the stratospheric entry H_2O and CH_4 propagation, and type of time-varying correlation between FRF and modelled AoA

described in Table 5.1 for three different periods: 1990-2017, 1990-2006, and 2002-2017. At the beginning we consider the extended 1990-2017 period and thereafter shorter periods.

The results of this work provide an estimate of the reliability of the approximation method to deduce circulation trends from observed stratospheric H_2O and CH_4 mixing ratios.

5.3 Application of the approximation method to the CLaMS data

Next we investigate the impact of the mentioned approximations on the quality of inferred AoA trends within a model environment, applying the procedure described in Sec. 5.2.1 and 5.2.2 to the CLaMS H_2O and CH_4 model results. The method, based on the two approximations, is named "approximation method" in the following, and abbreviated as APPROX.

The first term in equation 5.13, which refers to the changes in the stratospheric entry H_2O, is obtained as a linear trend of CLaMS H_2O from its 1990-2017 time series, averaged over 390-400 K potential temperature (approximately 80 hPa) and 30° S-30° N (see Fig. 5.3). Note that the region for averaging entry H_2O was chosen just above the cold tropical tropopause region. Interestingly, the H_2O trend during 2002-2017 is positive, while during 1990-2006 it is negative.

The second term in equation 5.13 requires two quantities: stratospheric entry CH_4 changes and FRF. The changes in the stratospheric entry CH_4 are calculated analogically to H_2O changes, as a linear trend of CLaMS CH_4 over the 1990-2017 period, averaged over 390-400 K potential temperature and 30° S-30° N (Fig. 5.4). The figure shows, that CH_4 linear trends for the periods 1990-2017 and 2002-2017 are almost equal.

Another quantity, necessary for the second term calculation in Eq. 5.13, is FRF. It is derived from relation 5.14. Following Hegglin et al. (2014), for $CH_{4\,[strat]}$ we take zonal mean simulated stratospheric CH_4 mixing ratios, averaged over 2005-2006. $CH_{4\,[entry]}$ is calculated as a mean over 2002-2006, and averaged between 390-400 K potential temperatures and 30° S-30° N (highlighted with the shaded grey area in Fig. 5.4). The mean CLaMS $CH_{4\,[entry]}$ mixing ratio over 2002-2006 is 1.696 ± 0.001 ppmv, which is approximately 0.05 ppmv lower than NOAA tropospheric measurements at Mauna Loa, used by Hegglin et al. (2014). The resulting FRF distribution is shown in Fig. 5.5. Due to the method, FRF is calculated from CLaMS climatological 2005-2006 CH_4 mixing ratios, and, thus, it is stable in time and does not depend on the chosen period. Thus, knowing FRF and $\Delta CH_{4\,[entry]}$ we can evaluate the second term in Eq. 5.13.

The impact of circulation changes on stratospheric H_2O changes is described by the changes in FRF, and is represented by the third term in Eq. 5.13. This third term is calculated as a residual (Eq. 5.15). Dividing it by $2CH_{4\,[entry]}$ (taken as a mean CH_4 over the considered period, averaged between 390-400 K potential temperature and 30° S-30° N, see Fig. 5.4), yields FRF changes, denoted as $\Delta\alpha$.

The different contributions to the total stratospheric H_2O change are shown in Fig. 5.6 for the 1990-2017 period. Figure 5.6a shows the "true" H_2O trend from the reference CLaMS simulation. Figures 5.6b, c represent the contributions from stratospheric entry H_2O and CH_4 mixing ratios respectively. Neither stratospheric entry H_2O nor CH_4 can explain the pattern of the "true" H_2O trend. The third term, presented in Fig. 5.6d, includes the impact from circulation changes. Note that it is calculated as the residual. In general, the different factors affect

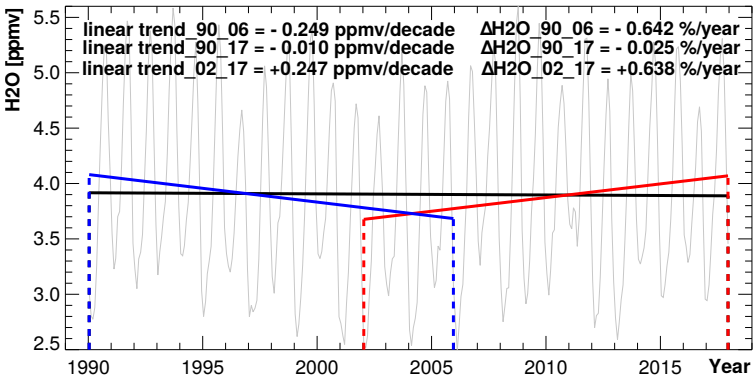

Figure 5.3: Time series of H_2O entry mixing ratios averaged over the tropics at 30°S-30°N and in the potential temperature layer 390-400 K. Linear trends for different periods are indicated with coloured lines: 1990-2006 blue line, 1990-2010 green, 1990-2017 black and 2002-2017 red. Also, the values of the linear H_2O trend (in ppmv per decade), as well as the relative H_2O trend (in % per year) for different periods are given. Data shown is from CLaMS simulation driven by ERA-Interim reanalysis.

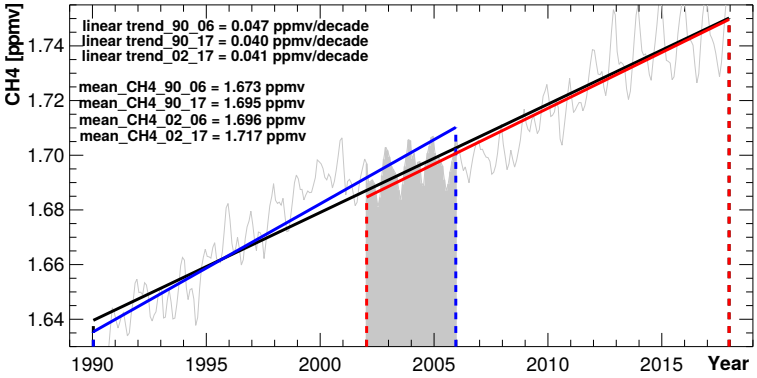

Figure 5.4: Time series of CH_4 entry mixing ratios averaged over the tropics at 30°S-30°N and in the potential temperature layer 390-400 K. Linear trends for different periods are indicated with coloured lines: 1990-2006 blue line, 1990-2010 green, 1990-2017 black, 2002-2017 red, and 2002-2006 period is highlighted with the shaded grey area. Also, the values of the linear CH_4 trend (in ppmv per decade), as well as the mean CH_4 value for different periods are given. Data shown is from CLaMS simulation driven by ERA-Interim reanalysis.

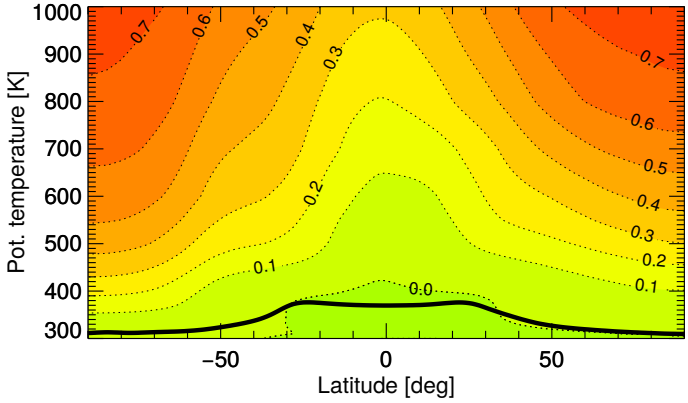

Figure 5.5: Annual mean FRF (α) distribution derived from CH_4 mixing ratio (simulated by CLaMS driven by ERA-Interim reanalysis) averaged over 2005-2006. The black line represents the tropopause calculated from ERA-Interim, and averaged over 2005-2006.

the stratospheric H_2O changes differently in different regions, consistent with the findings of Hegglin et al. (2014).

As a remark, HH is not conserved around and below the tropopause. Hence, the impacts from the drivers of stratospheric H_2O changes can not be calculated below the tropopause. Moreover, as mentioned before, CLaMS H_2O gives meaningful results only above the tropopause due to the simple parametrization of ice microphysics and omission of a convection parametrization. Thus, the region below TTL is masked in the figures (e.g., Fig. 5.6).

As known, FRF correlates well with the AoA. Consequently, the changes in FRF can be translated into an AoA trend. In order to estimate the AoA trend induced by the changes in stratospheric H_2O, we define the relationship between zonally averaged FRF (with monthly resolution within the year, calculated with the approximation method, shown in Fig. 5.5) and modelled AoA. The correlation function is presented in Fig. 5.7; it is derived by fitting a third-order polynomial, as suggested by Hegglin et al. (2014). From the Fig. 5.7, the empirical relationship between the CLaMS AoA and the FRF is described by

$$\text{AoA} \equiv f(\alpha), \tag{5.17}$$

where

$$f(\alpha) = 0.85 + 16.49\alpha - 25.30\alpha^2 + 13.77\alpha^3. \tag{5.18}$$

As pointed out above, the approximation method assumes, that the AoA-FRF relationship is stable in time (stationary). Hence, the same relationship 5.18 will be applied for all different periods, considered in the following. Using the Eq. 5.16, we can estimate AoA changes from the previously calculated FRF (α) and its changes ($\Delta\alpha$).

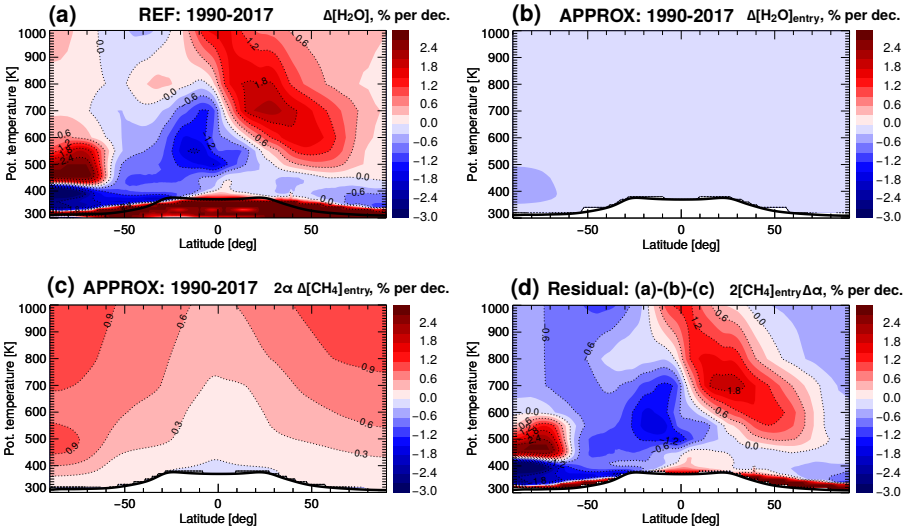

Figure 5.6: Long-term changes in stratospheric H_2O (a) and its drivers (b, c, d) over the period 1990-2017, derived from CLaMS simulation driven by ERA-Interim reanalysis. Sub-figure (b) represents contributions from the changes in stratospheric entry H_2O mixing ratio, (c) stratospheric entry CH_4 mixing ratio, and (d) circulation. The data is presented in percentage per decade, with relation to the climatological 1990-2017 CLaMS stratospheric H_2O mixing ratios. The black line is the tropopause calculated from the ERA-Interim. Below the tropopause (white region in b, c, d), the method can not be applied (see text).

The resulting AoA change for 1990-2017, estimated with the approximated method, is shown in Fig. 5.8a. It can be compared to the "true" AoA changes from the reference CLaMS simulations driven by ERA-Interim reanalysis, shown in Fig. 5.8b. We see, that quantitatively there are differences between the "true" and the estimated trend of the AoA. Firstly, the approximation method gives a large error in the Antarctic region. This was expected due to the strong dehydration occurring in that region and the related failure of HH conservation. Secondly, the approximation method overestimates the AoA trend in the NH subtropical middle stratosphere. Although, qualitatively, both trends (Fig. 5.8a, b) show a decreasing AoA trend in the LS, and an increasing trend in the NH middle stratosphere. Thus, the approximation method provides a good estimate of the AoA trend during 1990-2017, corroborating the validity of the use of the approximate method by Hegglin et al. (2014). Interestingly, during the 1990-2017 period, AoA trends show differences between the NH and SH. These hemispheric difference have been related to the effect of mixing (e.g., Ploeger et al., 2015a), and were also found in long-term age trends derived from the observed stratospheric CH_4 by Remsberg (2015).

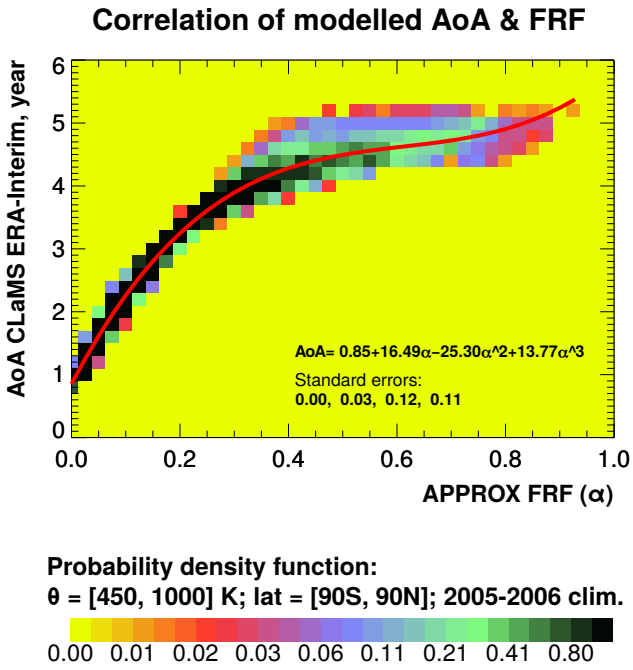

Figure 5.7: Relationship between CLaMS AoA and FRF, calculated with the approximation method. The considered correlated region is between 450-1000 K and 90° S-90° N. The colour bar represents the probability density function. The red line is the third-order polynomial fitting function. Note that due to the approximations in the method (described in Sec. 5.2.1), FRF is calculated from climatological 2005-2006 stratospheric CH_4. Thus here, FRF is correlated with climatological AoA from the same 2005-2006 period.

To assess the general applicability of the approximation method, we consider the period of 1990-2006. The result from the approximation method is presented in Fig. 5.8c, together with the "true" AoA trend from the CLaMS simulation (Fig. 5.8d). In this case, the AoA trend from the approximation method disagrees substantially, when compared with the "true" trend. The differences occur even in sign of the AoA trend. Particularly, clear differences occur in the exact strength of the AoA trend and its detailed pattern. Thus, the accuracy of the estimated AoA changes from the approximation method depends substantially on the considered period. In our study, the AoA trend from 1990-2017 was much closer to the "true" one, than the estimated AoA trend from 1990-2006.

In the following sections, we investigate the effects of the two approximations (instantaneous entry H_2O and CH_4 mixing ratio propagation; constant AoA-FRF correlation) on the quality of the estimated AoA trend.

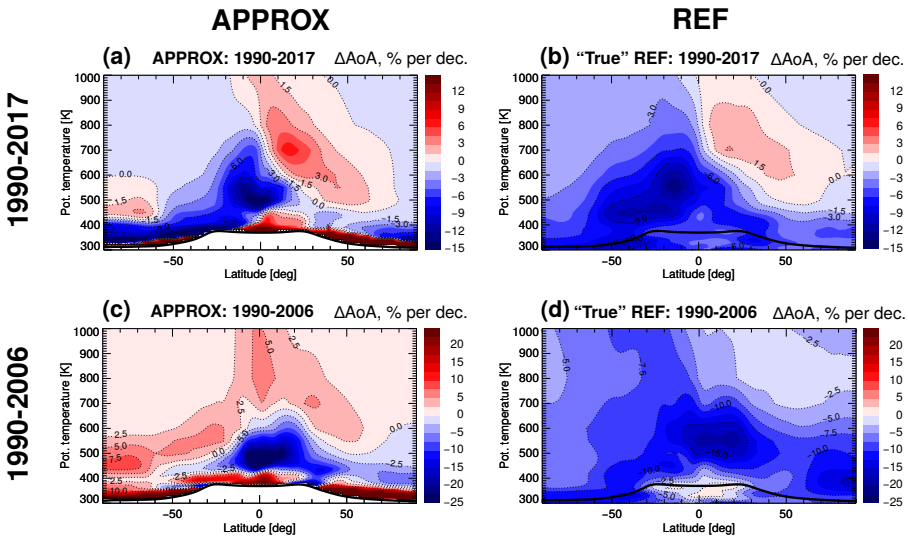

Figure 5.8: Decadal changes of AoA over 1990-2017 (a, b) and 1990-2006 (c, d). Figures (a, c) represent "true" AoA changes from the CLaMS simulation driven with ERA-Interim reanalysis. Figures (b, d) show AoA changes estimated with the approximation method. The changes are presented in percentage per decade with relation to the AoA climatologies of the considered period (regarding the used method of AoA calculation). The black line is the tropopause calculated from ERA-Interim. The white region below tropopause denotes the region, where the approximation method can not be applied (see text).

5.4 Impact of entry mixing ratio propagation

The goal of this section is to find out what causes the large uncertainty in the estimated AoA trend for 1990-2006 from the approximation method. Firstly, we evaluate the effect of the approximation of the instantaneous entry mixing ratio propagation. For this purpose, we perform a sensitivity study, with entry H_2O and CH_4 mixing ratios propagated through the convolution of the TTL mixing ratios with the modelled age spectrum, but with the stationary relationship (constant correlation) between FRF and modelled AoA (denoted as C-CORR in Table 5.1). The details of the used technique are described below.

5.4.1 The propagation of entry mixing ratios

Dynamical changes in the stratosphere affect both, the age spectrum and temperatures around the TTL, what in turn affects stratospheric H_2O, as well as HH (Fueglistaler, 2012). The propagation of the entry mixing ratio into the stratosphere is described by Eq. 5.3, for which it is necessary

to know the function $G(r,\ t \mid r_0,\ t-t')$, representing the age spectrum of the considered air volume, and $\chi(r_0,\ t-t')$, representing the time series of the trace gas mixing ratio at the entry to the stratosphere. If the air at the entry into the stratosphere is sufficiently mixed in the tropical lower stratosphere, the entry mixing ratio can be assumed fairly uniform.

Waugh and Hall (2002) give a comprehensive overview on the age of stratospheric air and its connection to the tracer distributions, including a theoretical, experimental and modelling view on the topic. Importantly, the age spectrum contains the information of the transport of the air between the source and response points. However, the age spectrum can not be measured directly, because the measured properties are always averaged in a macroscopic AP (Waugh and Hall, 2002). In principle, AoA and the age spectrum can be deduced from trace gas observations, but this is a complicated task (e.g., Engel et al., 2017; Hauck et al., 2019; Podglajen and Ploeger, 2019).

In our study of the mixing ratio propagation of entry H_2O and CH_4 mixing ratios, we use the age spectrum calculated with CLaMS driven by ERA-Interim winds and total diabatic heating rates. The age spectrum was calculated using a Boundary Impulse (time-)Evolving (BIER) method based on multiple tracer pulses, described by Ploeger and Birner (2016). Here, we give a concise overview on the BIER method.

For the inert tracer χ, with a pulse at the location r_0, the field time t_0, and the source time t_0^*, the time evolution of the source can be described with a δ-distribution

$$\chi(r_0,\ t_0)\ =\ \delta(t_0-t_0^*). \tag{5.19}$$

Thus, the Eq. 5.3 can be transformed to

$$\chi_{[strat]}(r,\ t'+t_0^*)\ =\ G(r,\ t'+t_0^*|\ r_0,\ t_0^*), \tag{5.20}$$

where $t'=t_0-t_0^*$ is a transit time, $G(r,\ t'+t_0^*|\ r_0,\ t_0^*)$ is the boundary impulse response at location r to δ-boundary condition at the location r_0 at a source time t_0^* (Ploeger and Birner, 2016).

Having N different tracers, $\chi_i (i=1,...,N)$, in the stratosphere with pulses at the location r_0 at times $t_{0[i]}$, gives us the field time dependence of the propagator G. The age spectrum, may be constructed at each field time t and location r as

$$G(r,\ t|\ r_0,\ t-t'_{[i]})\ =\ \chi_i(r,\ t). \tag{5.21}$$

In this way, we get N pieces of information for the age spectrum at the discrete transit times $t'_{[i]}\ =\ t-t_{0[i]}$.

For our study, we use $N\ =\ 60$ different boundary pulse tracers. The pulses were released directly at the tropical tropopause between 30° S-30° N. Precisely, the source region covers the potential temperature layer from 10 K below to 10 K above the WMO (lapse rate) tropopause. The particular tracer mixing ratio is set to 1 for each pulse for a period of 30 days (month) at the location r_0, and it is set to 0 in the location r_0 at other times. Pulses are launched every month. Consequently, to build the age spectrum for January 1990, the most recent tracer pulse has source times in January 1990, the second tracer pulse in December 1989, and so on. In our study, the original length of each age spectrum is 10 years.

It is known, that for transit times larger than 4-5 years, the age spectra are decaying roughly exponentially (e.g., Ploeger and Birner, 2016). Thus, the tail of the age spectrum can be approximated with an exponential function after some threshold transit time (10 years in our study). We used the exponential correction for the tail back to January 1979 for each age spectrum. After the correction, the age spectrum was normalized to unity. The normalization of the age spectrum is important for the propagation of the trace gases with low variability (e.g., CH_4) and has a weaker impact for the tracers with high variability (e.g., H_2O). The detailed shape of the age spectrum for March-April-May, 2006 at the equator at 450 K is shown in Fig. 5.9a, b together with the corrected age spectrum tail.

In our study, the entry time series of the trace gases (e.g., clock-tracers, CH_4, H_2O), are taken from zonally averaged monthly mean data simulated with CLaMS driven by ERA-Interim reanalysis. The location of entry to the stratosphere is approximated at the 390 to 400 K layer between 30°S-30°N, which is just above the TTL to avoid complications with the H_2O dehydration. The small difference between the age spectrum source region (tropopause $\pm$10 K) and the trace gases entry region has only a negligible impact on our results from above $\approx$420 K due to the small difference in the transit time between the two regions.

Hence, having the age spectrum and boundary time series of the tracer, we can apply Eq. 5.3 to propagate entry mixing ratios of the tracers into the stratosphere. Note, that we applied this procedure to CLaMS age spectrum and boundary time series, from 1990 to 2017, due to availability of the CLaMS data and the necessary age spectrum length. In the future, the procedure can be extended to other years.

Below, we estimate the accuracy of the propagation procedure (Eq. 5.3) using the example of the inert conserved clock tracer BA ("boundary age"; used for AoA calculation in CLaMS model), and the HH tracer.

5.4.2 Application of propagation procedure to the conserved mean age tracer

In theory, convolution of the trace gas mixing ratio with the age spectrum yields exactly the mixing ratio at the sampling location and time (see Eq. 5.3). However, as we use monthly mean source time series and age spectra for the entry mixing ratio propagation, and due to the limited length of the age spectra, the reconstructed mixing ratios in the stratosphere has a finite precision.

Firstly, we check the precision of the propagation procedure on the example of the conserved passive and inert clock-tracer of the AoA (BA, in ppmv). BA is an artificial clock tracer, introduced in CLaMS, with a linearly increasing source time-series in the lowest model layer; it is generally used to calculate AoA in models (Hall and Plumb, 1994).

Figure 5.9 shows the BA reconstruction for 2006 at one location in the stratosphere (450 K at the equator). Figure 5.9a explains the reconstruction of the AoA at a particular time and at a particular location, based on the convolution of the BA boundary mixing ratios with the age spectrum for March-April-May (described by Eq. 5.3). The boundary BA time series (shown as black line) is taken as zonal mean CLaMS BA averaged over 390-400 K potential temperature and 30° S-30° N. The monthly age spectra (solid blue for March, solid green for April, and dashed pink for May) is presented with the starting point at the respective field time running backward. The detailed age spectra calculations are described in Sec. 5.4.1. The results of the

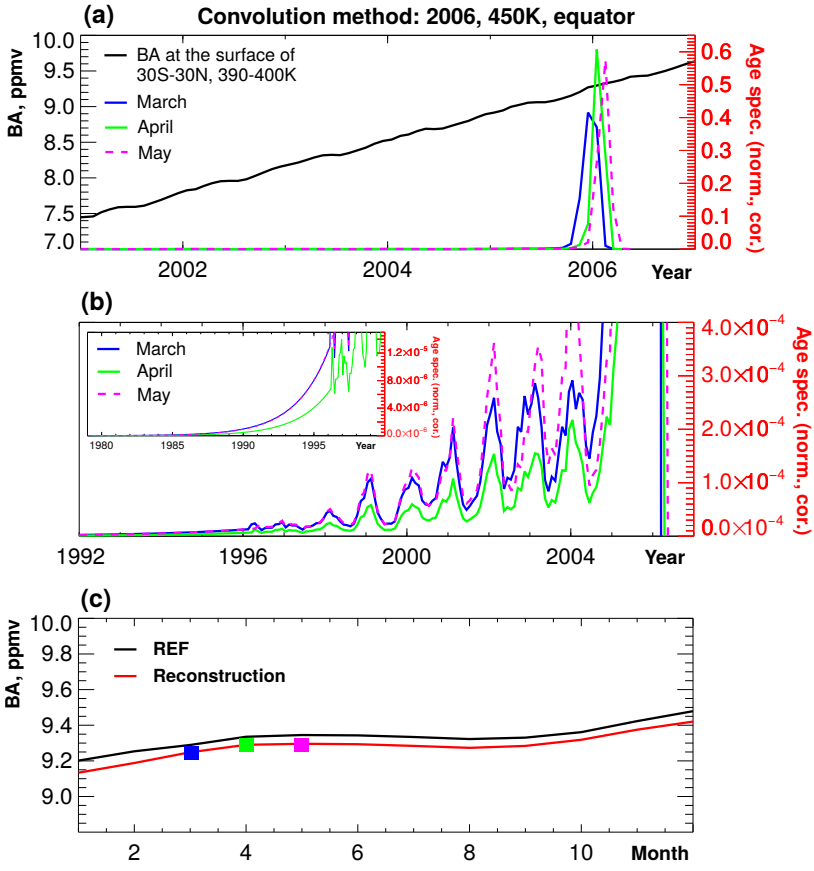

Figure 5.9: Illustration of the CLaMS clock tracer (BA) propagation, on the example of 2006 (during March, April, May) at θ = 450 K and 0°. Black line at the panel (a) represents the boundary surface mixing ratio of the BA tracer averaged between 30° S-30° N and 390-400 K potential temperature. The coloured lines represent the age spectrum for the chosen months: March (solid blue), April (solid green) and May (dashed pink). Figure (b) shows the detailed structure of the age spectrum tail. The monthly age spectrum is normalized and has a corrected tail, expanded to the beginning of 1979 with the exponential function fit (see text), shown in the zoomed-in Fig. (b). The convolution of the BA time series with monthly age-spectrum yields the reconstructed monthly BA in the stratosphere, shown in Fig. (c) with the red line, and the blue/green/pink dots illustrating specific reconstructed values for March/April/May respectively. The black line in panel (c) shows the "true" BA CLaMS values.

age spectrum and BA time series convolution for 2006 are shown in Fig. 5.9c (red line), and compared to "true" CLaMS BA (shown as black line, termed REF). Note, that each convolution event in Fig. 5.9a gives one reconstruction point in Fig. 5.9c. In theory, reconstructed and "true" BA should be equal. But, there is a small offset between them, with a low bias for the reconstructed BA. This disagreement is partly related to inaccuracies in the age spectrum (one-month pulsing, limited length), and to inaccuracies in the boundary time-series (averaging in the layer of 390-400 K potential temperature and 30° S-30° N). Note, that through the convolution of the age spectrum and the TTL time series it is possible to reconstruct mixing ratios only above the tropopause (or the level of the boundary time-series, if it was chosen different from the TTL).

Propagating BA to each grid point in the stratosphere, provides the full reconstructed stratospheric BA field. Fig. 5.10 shows the comparison between "true" and reconstructed BA for July, 2006. The relative difference between them in the lower stratosphere is less than 2 % depending on the considered level. Such a high precision of reconstructed BA is also kept for any other month from 1990 to 2017. Note, that propagated BA gives an offset towards lower values, when compared with CLaMS BA. As the conclusion, the procedure of the entry mixing ratios propagation using the CLaMS modelled age spectrum is highly reliable for the inert tracer.

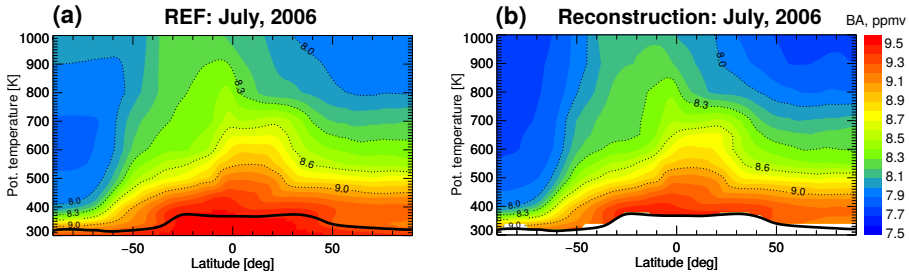

Figure 5.10: Zonally averaged BA distributions for July, 2006; (a) shows "true" BA, simulated with CLaMS driven by ERA-Interim reanalysis, (b) is BA propagated from the TTL though the convolution with the age spectrum. The black line is the tropopause calculated from ERA-Interim. The white region below the tropopause (b) is the region, where the reconstruction method can not be applied (see text).

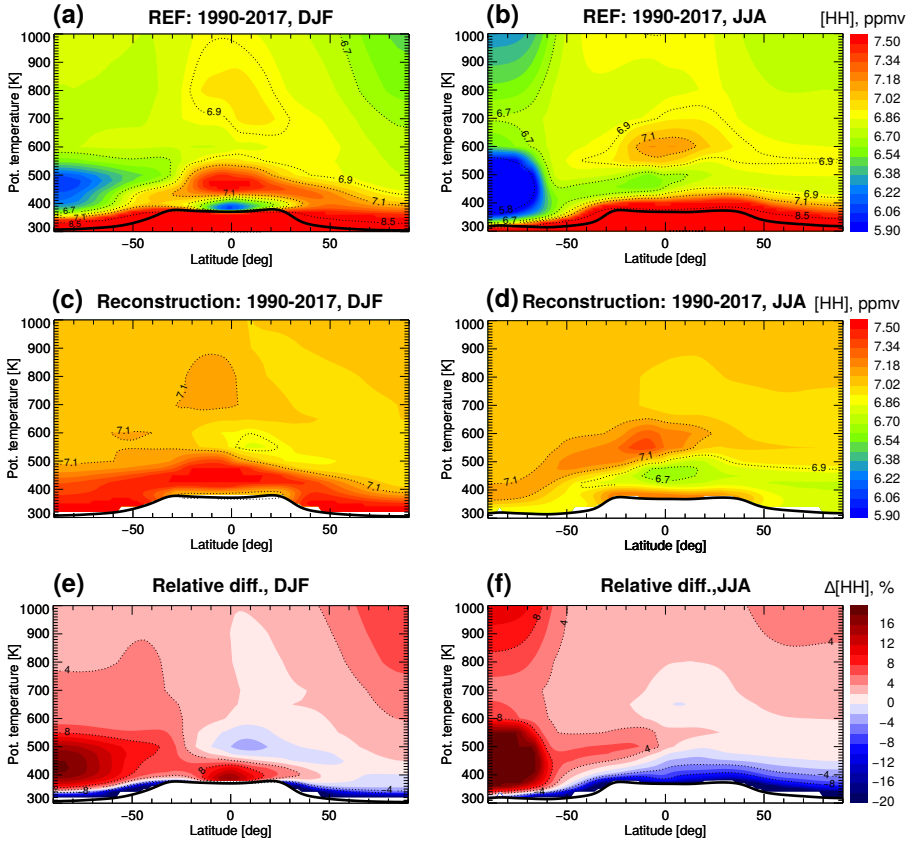

Figure 5.11: Zonal mean HH climatology for 1990-2017 for winter (DJF, left panel) and summer (JJA, right panel) seasons. Figures (a, b) represent HH simulated with CLaMS driven by ERA-Interim reanalysis (denoted as REF). Figures (c, d) show reconstructed HH. The relative differences between reconstructed and "true" HH are shown in (e, f) in percentage with respect to the mean CLaMS HH climatologies. The black line is the tropopause calculated from ERA-Interim. Below the tropopause, the white region indicates the areas, where the propagation procedure can not be applied.

5.4.3 Application of propagation procedure to total hydrogen (HH)

Next, we consider the accuracy of the propagation procedure by applying it to the conserved HH tracer (see Eq. 2.15). HH is nearly constant in the lower and middle stratosphere and, thus, Eq. 5.3 can be used to propagate entry HH mixing ratios into the stratosphere.

The result of the propagation procedure is shown as zonal mean 1990-2017 climatologies in Fig. 5.11c, d, whereas the "true" HH from CLaMS is shown in Fig. 5.11a, b. The lowest "true" HH mixing ratios are located in the region of Antarctic dehydration, which can not be captured with the propagation procedure. The propagated HH are overestimated or underestimated, depending on the considered location. The propagated HH gives lower mixing ratios when compared to the "true" HH below 500 K during summer season (Fig. 5.11f). This is due to the used averaged HH boundary for reconstruction (between 390-400 K potential temperature, from 30° S to 30° N), where H_2O during the summer is lower than the "true" H_2O mixing ratios in the Asian monsoon. The opposite situation occurs during the winter period below 500 K (Fig. 5.11e), when the "true" H_2O mixing ratios are lower than the mean H_2O at the boundary. Above 500 K, in general, the propagated HH gives higher values than CLaMS HH. Propagated HH captures well the inter-seasonal response. The relative difference between CLaMS HH and propagated HH (Fig. 5.11e, f) is less than 4 %, except the dehydration region at the SH pole, and the middle stratospheric high latitudes. The effects of the Antarctic dehydration are discussed in Appendix B.

Thus, the propagation procedure of the entry mixing ratios by the age spectrum has a high precision for the HH tracer.

5.4.4 The effects of propagated stratospheric entry H_2O and CH_4 mixing ratios on the AoA trends

Having the reliable technique of propagating entry mixing ratios into the stratosphere (described in the previous Sect. 5.4.2, 5.4.3), we can reconstruct stratospheric entry H_2O and CH_4 mixing ratios from their TTL time series. After applying the propagation procedure (Eq. 5.3), we gain zonally averaged stratospheric entry H_2O and CH_4 distributions with a monthly resolution on a latitude-potential temperature grid. Then, based on Eq. 5.13, we can estimate the contributions from propagated stratospheric entry H_2O, CH_4 (first and second term in the equation, respectively). The needed trends were calculated through a linear fit with the least standard deviation at each latitude-potential temperature grid.

The changes in FRF we estimate as the residual (see Eq. 5.15). Then, the changes in FRF can be translated into changes in AoA (through Eq. 5.16) using the same stationary correlation between AoA and FRF (relation 5.18).

Resulting AoA trends from this sensitivity experiment (with the propagated mixing ratios by the age spectrum) are denoted C-CORR. Note that for calculating trends in the AoA, in both cases, APPROX and C-CORR, the same FRF distribution (α) was used (taken from Fig. 5.5), but the changes in circulation ($\Delta\alpha$) are different depending on whether the stratospheric entry H_2O and CH_4 were propagated by the age spectrum or not.

The estimated AoA changes for 1990-2006, using mixing ratio entry propagation instantaneously or by the age spectrum, are shown in Fig. 5.12a, b (note that (a) is the same with Fig. 5.8 c). Clearly, the approximation of the instantaneous entry propagation largely affects the AoA trend (difference between Fig. 5.12a and b). Therefore, adding the propagation by the age spectrum to the method (even as the monthly mean), noticeably improves the estimated AoA trend.

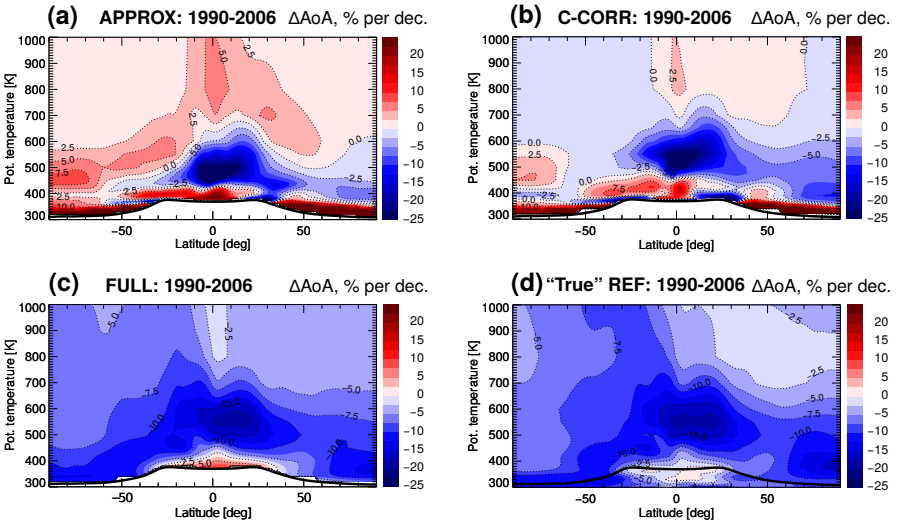

Figure 5.12: Comparison of AoA trends for the 1990-2006 period, estimated using different methods: (a) applying the approximation method (instantaneous entry propagation and a constant AoA-FRF correlation); (b) using entry H_2O and CH_4 propagations and a constant AoA-FRF correlation; (c) using entry CH_4 propagation and monthly varying AoA-FRF correlation; (d) shows the "true" AoA trend from CLaMS simulation driven by ERA-Interim reanalysis. The AoA trends are presented in percentage per decade with respect to the 1990-2006 AoA climatologies from the used method. The black line is the climatological 1990-2006 tropopause calculated from ERA-Interim. Below the tropopause, the white region indicates the areas, where the propagation procedure can not be applied.

5.5 Impact of using a monthly AoA-FRF correlation

In this section, we evaluate the effect of the assumption of a constant correlation between FRF and AoA. For this purpose, we perform one more sensitivity study, with propagated entry mixing ratios for H_2O and CH_4 through the convolution of the TTL mixing ratios with the modelled age spectrum, and the monthly FRF-modelled AoA correlation (denoted as FULL). The details of the used correlation technique is described below.

The difference between C-CORR and FULL is in the used correlation between AoA-FRF, and the way of FRF calculation. For C-CORR, a constant AoA-FRF was used, whereas for FULL a monthly varying correlation was used to include effects of the non-stationarity of the correlation. The procedure of propagating entry mixing ratios in C-CORR and FULL is exactly the same. As a remark, in FULL method, FRF is calculated from CLaMS monthly entry CH_4 propagated with the age spectrum (assumed to be $CH_{4\,[entry]}$) and CLaMS stratospheric monthly mean CH_4 mixing ratios (assumed to be $CH_{4\,[strat]}$); consequently, FRF has a monthly resolution.

A comparison of FRF calculated with the APPROX (see Sect. 5.3) and FULL methods is presented in Fig. 5.13. Here, FRF is shown as a time series at 500 K potential temperature (about 20 km, and averaged at the tropics between 20° S-20° N. The discrepancy between two FRF estimations, with APPROX or FULL, depends on the considered period. For example, for the years 1992 or 2000, the FRFs differ by more than 50 %. Whereas, during the other years, such as 1997 or 2007, the differences between FRFs is relatively small.

Figure 5.14 presents the FRF distribution at the level of 700 K potential temperature, used in APPROX (a) and in FULL (b) methods. Evidently, monthly propagation of stratospheric entry CH_4 changes FRF patterns. Thus, for example, in the region of the South pole during 1999-2001, FRF is overestimated with the APPROX method, and during 1990-1998 it is underestimated; or, during 2010-2017, FRF is underestimated in the NH tropics when using the APPROX method.

To improve the AoA-FRF correlation (used as constant in APPROX and C-CORR, see Sect. 5.3, Sect. 5.4.4), we calculate a monthly varying correlation of the zonally averaged FRF (calculated though CLaMS monthly propagated entry CH_4 by the age spectrum) and zonally averaged CLaMS AoA.

For illustration of the non-stationarity of the correlation, Fig. 5.15 presents the AoA-FRF correlation functions for January, April and July for 1995. The relation between AoA and FRF is derived by fitting a third-order polynomial function for each considered month. Although, the lines in Fig. 5.15 appear very close, the AoA-FRF correlation functions are unique for each month, because the differences in magnitude of the coefficients are greater than the standard error's range. Moreover, monthly AoA-FRF correlation functions have a very small difference for relatively young air (below 4 years), and low FRF (below 0.4). Thus, the tropical pipe and LS can be still described well with the averaged AoA-FRF correlation function. But, one should be careful applying the constant AoA-FRF correlation in the middle and upper stratosphere.

Thus, it is reasonable to use a monthly varying AoA-FRF correlation, instead of a constant AoA-FRF relationship. By applying constant AoA-FRF correlation function, some atmospheric processes can be smeared out, causing wrong description of the dynamic state of the stratosphere. As a remark, monthly AoA-FRF correlation functions are still not perfect, and have

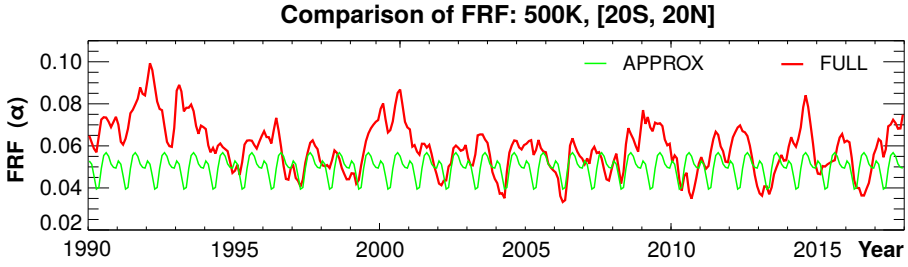

Figure 5.13: Comparison of FRF time series (1990-2017) calculated with the assumption of the instantaneous entry propagation (green line, APPROX) and with propagated entry CH_4 by the age spectrum (red line, FULL). Presented data is at 500 K averaged between 20°S-20°N.

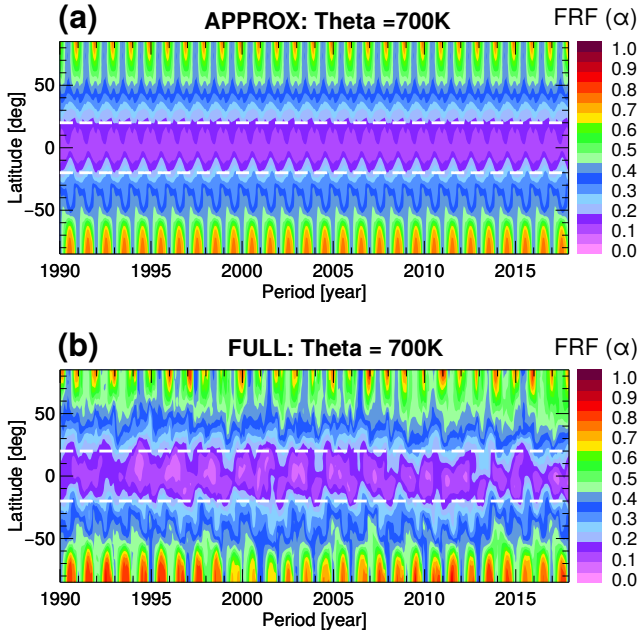

Figure 5.14: Comparison of FRF averaged over 1990-2017 at the level of 700 K potential temperature. Figure (a) shows FRF calculated with the approximation method, and Fig. (b) is taking into account the propagation of the entry CH_4 by the age spectrum. Approximate boundaries of the tropical region, 20°S and 20°N, are highlighted with the dashed white lines.

some bias during the same month. Furthermore, an accurate AoA-FRF correlation function depends not only on the considered period or time resolution, but also on longitude, latitude and altitude (see Appendix C).

In the FULL method, due to the monthly varying AoA-FRF correlation functions, FRFs are translated into AoA for each month. The AoA trend is calculated from resulting AoA as a linear fit with the least standard deviation at each latitude-potential temperature grid. Note, that for estimating AoA trend with the FULL method, the propagated entry H_2O mixing ratios are not used; the AoA trend is deduced from FRF, which requires only propagated entry CH_4 mixing ratios.

The comparison of the estimated AoA trends for 1990-2006 from the three different approaches, together with the "true" CLaMS AoA trend, is shown in Fig. 5.12. Clearly, the two used approximations indeed affect the accuracy of the estimated AoA trend. Overall, APPROX gives the worst estimate of the AoA trend (Fig. 5.12 a). But, even adding the entry H_2O and CH_4 propagation (Fig. 5.12b) does not significantly improves the AoA trend representation. When comparing C-CORR to APPROX, the patterns stay the same, and there are visible improvements

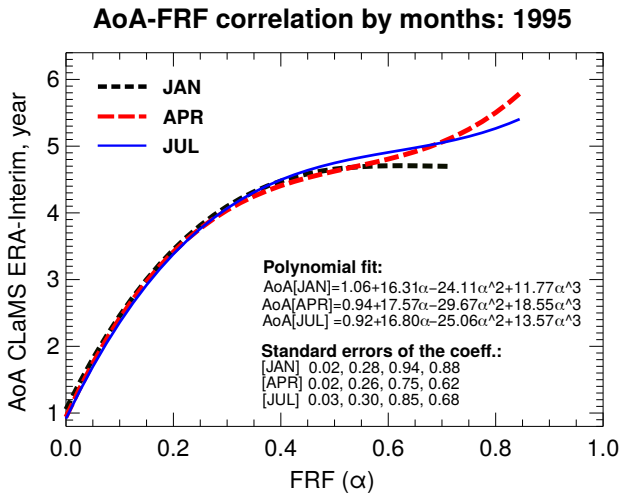

Figure 5.15: Relationship between FRF (used in FULL method) and CLaMS AoA for January (black dashed line), April (red dashed line) and July (blue solid line). For each months, FRF and CLaMS (driven by ERA-Interim) AoA were taken as zonally averaged data between 450 and 1000 K (where FRF has positive values due to the method) at the whole range of latitudes (90° S-90° N). The AoA-FRF relationship is shown by monthly fitting third-order polynomial function to the AoA-FRF distribution (which is not shown to avoid too busy plot).

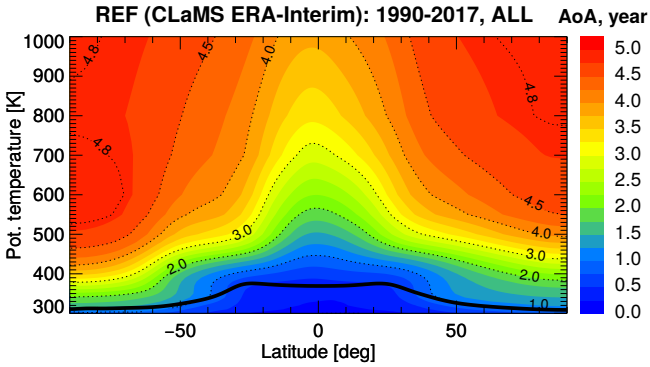

Figure 5.16: Zonal mean of AoA from CLaMS reference simulation driven by ERA-Interim reanalysis. Data shown are climatologies for 1990-2017 years.

above 600 K from including propagation of entry mixing ratios. Finally, keeping the entry CH_4 propagated by the age spectrum, and, at the same time including monthly varying AoA-FRF correlation (Fig. 5.12c) gives the best estimate of the AoA trend. Thus, the monthly AoA-FRF correlation improves the accuracy of the estimated AoA trend, both qualitatively and quantitatively.

The same sensitivity experiments are carried out for the period, 2002-2017 (Fig. 5.17). The approximation method shows the worst estimation of the AoA trend: while the overall pattern is similar, clear differences occur in the exact strength of the AoA trend and in the detailed structures. Above 600 K, the derived AoA trend from APPROX even differs in sign drawing a totally different picture of BDC changes. Propagation of the entry H_2O and CH_4 mixing ratios (Fig. 5.17b) improves the AoA trend above 600 K. But, below this level, the AoA trend is still not well represented. Consistently with the previous discussion, the best estimation of the AoA trend results from additionally including the monthly varying AoA-FRF correlation (Fig. 5.17c), giving the sign and patterns of AoA trend very close to the "true" AoA trend (Fig. 5.17d).

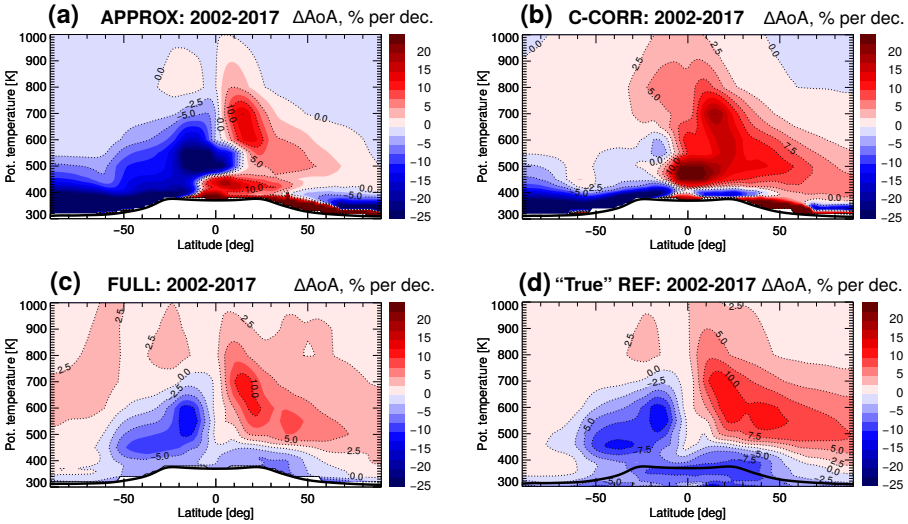

Figure 5.17: Comparison of AoA trends for the 2002-2017, estimated with different approximations: (a) approximation method (instantaneous entry propagation and constant AoA-FRF relationship); (b) using entry H_2O and CH_4 propagation and a constant AoA-FRF relationship; (c) using CH_4 entry propagation and monthly AoA-FRF correlation; (d) "true" AoA trend from CLaMS simulation driven by ERA-Interim reanalysis. AoA trends are presented in percentage per decade with respect to 2002-2017 AoA from the used method. The black line is the climatological 2002-2017 tropopause calculated from ERA-Interim. Below the tropopause, the white region indicates the areas, where the propagation procedure can not be applied.

5.6 Discussion

In the following, we further assess the effects of the two approximations of assuming (I) an instantaneous propagation of stratospheric H_2O and CH_4 entry mixing ratios, and (II) a constant correlation between FRF and AoA. Therefore, the differences among AoA trends estimated with different methods (APPROX, C-CORR, FULL) and for different periods are analysed (Fig. 5.18). The difference between AoA trends from APPROX and C-CORR gives an estimate of the magnitude of the approximation I. The difference between AoA trends from C-CORR and FULL gives an estimate of the magnitude intensity of the approximation II.

Figure 5.18a shows the difference in AoA trend for 1990-2006 estimated with the methods APPROX and C-CORR (see also Fig. 5.12a, b). The difference above 600 K is smaller than 5 %, below 600 K – the pattern is more complicated to interpret. Note, that the C-CORR method includes the entry H_2O and CH_4 mixing ratios propagation using the age spectrum, instead of the instantaneous propagation used in the APPROX method.

To gain a better understanding of the reasons for these patterns in Fig. 5.18a, we look at the contributions to the AoA trend in the APPROX and CORR methods (Fig. 5.19). The contributions of stratospheric entry H_2O mixing ratio trends are shown in Fig. 5.19b, c. The differences between the methods are a few precents.The difference in the contributions from stratospheric entry CH_4 mixing ratio trends estimated with APPROX and C-CORR is smaller, and reaches 0.5 % per decade (Fig. 5.19d, e). The circulation contribution is calculated as the residual between CLaMS H_2O trend (Fig. 5.19a) and the other two components; it is shown in Fig. 5.19f, g. The differences in the circulation components are caused by the discrepancies in the stratospheric entry H_2O and CH_4 mixing ratio contributions (calculated with APPROX or C-CORR), with the major impact from the stratospheric entry H_2O trend.

As the conclusion, instantaneous entry propagation causes an error in the estimated stratospheric entry H_2O and CH_4 mixing ratio contributions. This, in turn, causes the error in the derived circulation impact, which naturally translates through the constant AoA-FRF relationship into AoA trend (Fig. 5.19h, i), keeping the patterns comparable to the circulation change patterns. So, underestimated circulation changes cause also underestimated AoA changes and vice versa. As a result, the approximation of instantaneous entry propagation can lead even to a sign flip in the AoA trend (when compared to the "true" AoA trend)

Figure 5.18b shows the difference in AoA trend for 1990-2006 from the methods C-CORR and FULL (see also Fig. 5.12b, c). Above 600 K the discrepancies are around 5 % per decade. A more complex structure is shown below 600 K. Consequently, the effects of both approximations (on the estimated AoA trend) are comparable.

For the other periods 2002-2017 and 1990-2017 (Fig. 5.18c, d and Fig. 5.18e, f) the differences in AoA trends above 600 K are less than 5 % per decade. Below 600 K, the differences in AoA trends are higher with the maxima at approximately 480 K. Interestingly, for 2002-2017 and 1990-2017, the effects of the approximations I and II are opposite in sign. Consequently, the effects from both approximations cancel out, such that the APPROX method yields results remarkably close to the true AoA trend (see Fig. 5.8a, b, Fig. 5.17a, d). However, in general such cancellation can not be expected and the approximation method APPROX can produce misleading results.

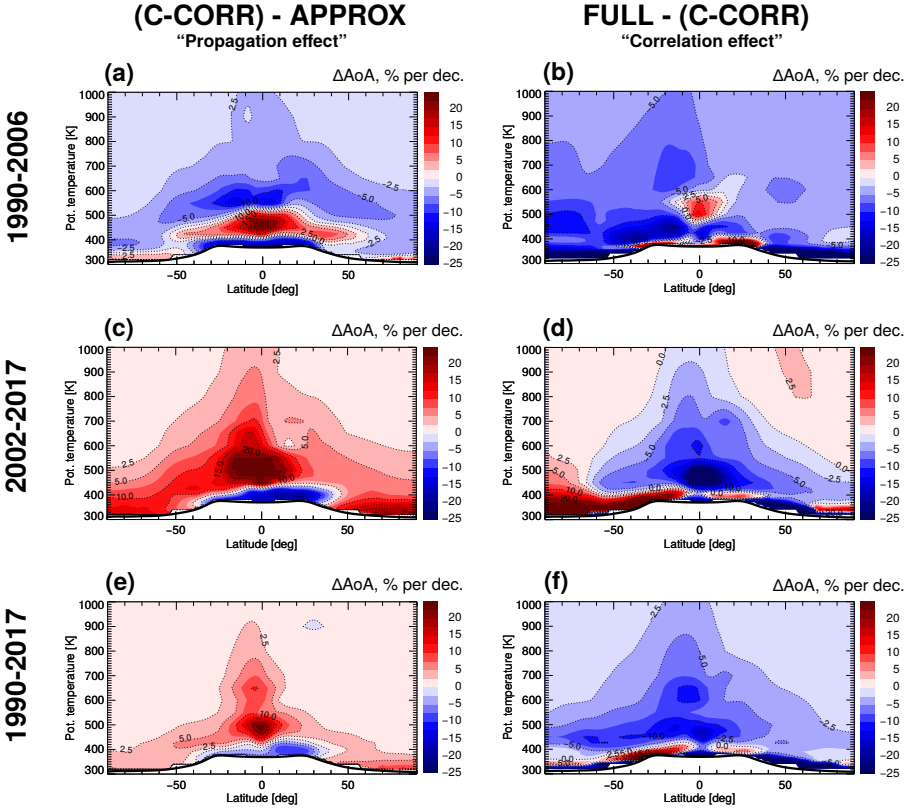

Figure 5.18: Differences in AoA trends estimated with the three methods (APPROX, C-CORR, and FULL) for the periods 1990-2006 (a, b), 2002-2017 (c, d), 1900-2017 in (e, f). The AoA trends are calculated in percentage per decade with respected to the AoA from the used method. The black line is the climatological tropopause calculated from ERA-Interim for the considered period. The white region below the tropopause indicates the areas where the propagation procedure can not be applied.

In order to estimate the accuracy of circulation impact ($2CH_{4[\text{entry}]}\Delta\alpha$) calculated as the residual (in APPROX and C-CORR methods), we further consider a set of circulation contributions, where $\Delta\alpha$ was calculated as a residual in APPROX and C-CORR, and as a linear trend (from α) in the FULL method. We assume, that the full reconstruction method FULL is the closest to the true stratospheric circulation impact. The comparison of the circulation contributions are presented in Fig. 5.20 for the different periods 1990-2006, 1990-2017, 2002-2017. First and second columns show circulation impacts from APPROX and C-CORR methods, third

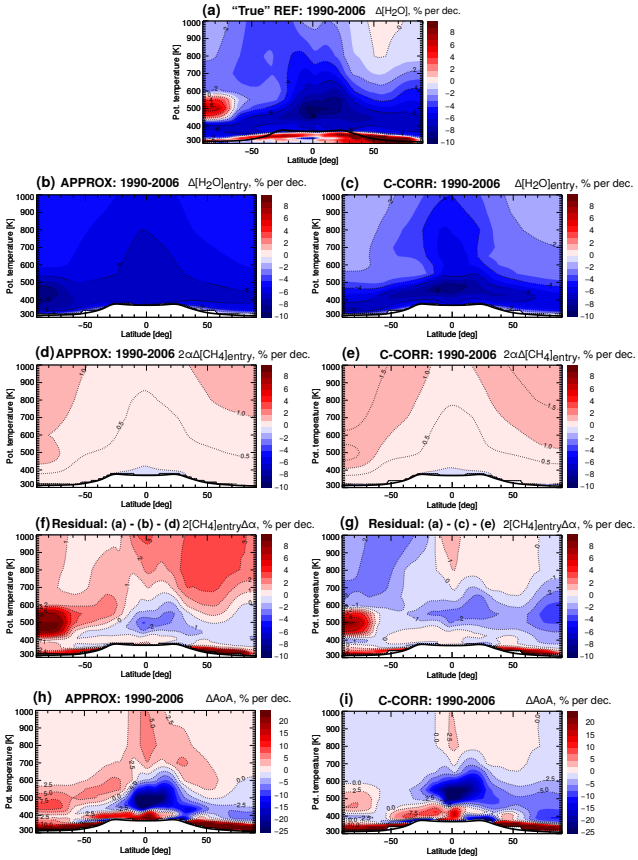

Figure 5.19: Contributions to H_2O trends during 1990-2006, shown in percentage per decade with respect to CLaMS 1990-2006 H_2O climatologies. Figure (a) represents the "true" H_2O trend calculated from CLaMS simulations driven by ERA-Interim reanalysis. Further plots show the drivers of H_2O trends from the approaches with instantaneous entry H_2O and CH_4 propagation (APPROX; b, d) and propagated entry mixing ratios by the age spectrum (C-CORR; c, e). Note, that (a)-(g) are presented in percentage per decade, with relation to the climatological 1990-2006 CLaMS stratospheric H_2O mixing ratios. The contribution from the circulation changes is calculated as the residual (f, g). Figures (h, i) show the respective AoA trends calculated through constant in time AoA-FRF relationship (see Eq. 5.17). The black line is the tropopause calculated from ERA-Interim. Below the tropopause, the white region indicates the areas, where the propagation procedure can not be applied.

column represents circulation changes from the FULL method (using propagated entry CH_4 climatologies and calculated linear FRF trend).

From the comparison of Fig. 5.20 (b, c), (e, f), and (h, i), we conclude, that calculating the circulation impact as a residual, yields a reliable representation of the circulation contribution. Large discrepancies occur in the Antarctic region, where the reconstruction method is expected to fail due to presence of local dehydration. Thus, the AoA trend estimated from circulation contribution calculated as a residual, is not reliable in the Southern polar region (Fig. 5.20a, d, g). Furthermore, the residual circulation contribution depends also on the accuracy of the used H_2O trend (in our study, H_2O trend is calculated from CLaMS simulation driven by ERA-Interim reanalysis). The impact of the dehydration at the polar regions to the H_2O CLaMS distribution is discussed in the Appendix B.

In general, the errors in the estimated circulation contribution from the APPROX method can be large, and the sign of the circulation contributions can be even opposite in particular regions

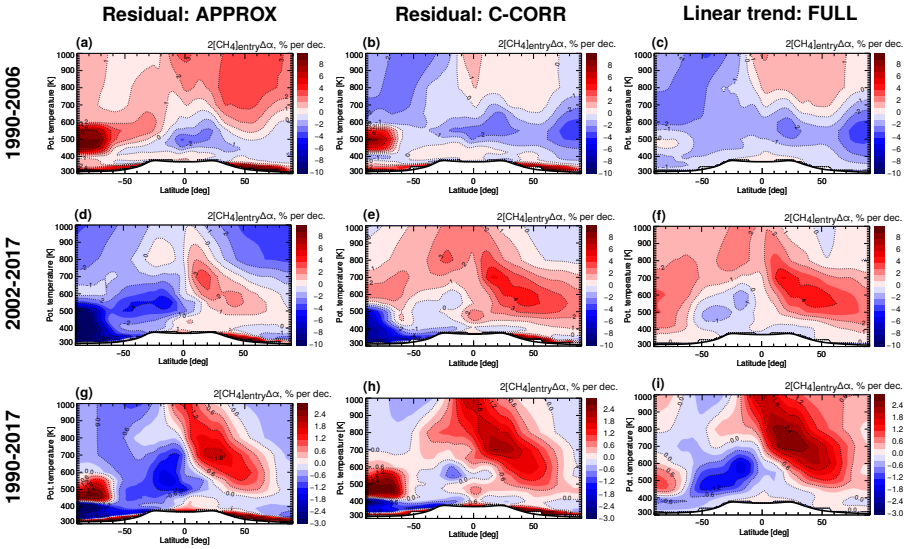

Figure 5.20: Circulation contribution ($2CH_{4\,[entry]}\Delta\alpha$) estimated with three approaches: calculated as a residual in APPROX (a, d, g) and in C-CORR (b, e, h) methods, and as a linear trend in FULL method (using a linear fit with the least standard deviation at each latitude-potential temperature grid; c, f, i). The contributions are shown for three periods: 1990-2006 (a, b, c), 1990-2017 (d, e, f) and 2002-2017 (g, h, i). The data are shown in percentage per decade with respect to CLaMS H_2O climatologies from the considered period. The black line is the tropopause calculated from ERA-Interim. Below the tropopause, the white region indicates the areas, where the propagation procedure can not be applied.

(see Fig. 5.20 (a, b), (d, e), and (g, h). Propagating stratospheric entry H_2O and CH_4 by using the age spectrum (in C-CORR) improves the representation of circulation changes significantly, except in the Southern polar dehydration region.

5.7 Chapter conclusions

The BDC is an important factor controlling the UTLS composition, which, in turn, crucially affects the global radiation budget and climate. Therefore, changes in the BDC with global warming may induce important feedback mechanisms on climate. However, the BDC is a zonal mean residual circulation and can not be measured directly. Thus, it is necessary to infer BDC trends from the changes in measured trace gas distributions. For estimation of the AoA trend, two main simplifications are often applied: (I) instantaneous propagation of entry H_2O and CH_4 mixing ratios, and (II) constant AoA-FRF relationship. In this chapter, we assessed the effects of I and II approximations on the accuracy of the AoA trend estimation from stratospheric H_2O trend within a CLaMS model environment.

We carried out different sensitivity experiments: including both above mentioned approximations (APPROX), only the constant correlation approximation but representing the correct entry mixing ratio propagation (C-CORR), and representing the non-stationarity of the correlation as well as the entry mixing ratio propagation (FULL). Estimated AoA trends were compared to the actual CLaMS AoA trend ("true"). Each of these methods assumes that stratospheric H_2O changes can be divided into changes in the entry H_2O mixing ratio, changes in the entry CH_4 mixing ratio, and circulation changes, which, in turn, are related to changes in the BDC.

We investigated three periods (1990-2006, 1990-2017, 2002-2017) for the effects of the I and II approximations on the AoA trend estimation. Our results show that the accuracy of the defined AoA trend depends on the used method, considered period and investigated location of the stratosphere. Moreover, both approximations are important, and they impact the estimated AoA trend qualitatively and quantitatively.

Method APPROX showed noticeable differences in the derived AoA trend when compared with the "true" AoA trend from CLaMS (REF), but strongly depending on the considered period. For some periods the overall resulting AoA trend patterns are similar, but in general clear differences occur particularly in the exact strength of the AoA trend and in its detailed structure. In specific regions of the stratosphere, derived AoA trends from APPROX were even different in sign drawing different pictures of BDC changes. However, the estimated AoA trend during 1990-2017 period was comparably well represented with method APPROX. We speculate, that the good agreement for 1990-2017 is likely a coincidence, as the constant FRF (which was calculated through averaged 2005-2006 stratospheric CH_4) is roughly in the middle of the 1990-2017 period, and it acts as a "mean" quantity over the whole 1990-2017 period. For the other two considered periods (1990-2006 and 2002-2017) the APPROX method did not provide a reliable representation of the true AoA trend.

To calculate the impact of the instantaneous entry propagation, we compared the resulting AoA trends from APPROX and C-CORR. The usage of the stratospheric entry H_2O and CH_4 propagation in C-CORR, improves the representation of the circulation contribution, and, in turn, improves the calculated AoA trend. But, depending on the investigated region of the stratosphere

and the considered period, the error still can be large.

To estimate the impact of assuming a constant AoA-FRF relationship, we compared the resulting AoA trends defined with C-CORR and FULL. Adding the monthly varying AoA-FRF correlation in the FULL method (instead of using a constant AoA-FRF correlation, as done in APPROX and C-CORR) improves the AoA trend representation substantially. Although, the monthly AoA-FRF correlation is not perfectly compact, as the AoA-FRF relationship can depend also on the other parameters (such as latitude, height, longitude). As a conclusion, the precise AoA-FRF correlation is an important factor to take into account when estimating AoA trends and interpreting BDC changes.

In summary, both approximations (assuming instantaneous entry propagation and constant AoA-FRF correlation) affect the estimated AoA trend similarly strong. Depending on the considered period, the effects from both approximations can also be opposite (e.g., for 1990-2017 or 2002-2017), and may even cancel out, resulting in a good estimate of the AoA trend. Thus, we would encourage to be careful with using the APPROX method, as it can lead to the wrong results, depending on the considered period.

The results of this chapter can be used for assessing the uncertainty in estimation of stratospheric circulation changes from global satellite measurements.

Chapter 6

Summary and conclusions

This thesis investigates the processes controlling UTLS H_2O. The first part of the thesis is particularly focused on studying the effects of TTL temperatures, horizontal transport, and small-scale mixing on the simulated UTLS H_2O distribution. In the second part of the thesis, the effects of commonly used approximations to estimate AoA trends from stratospheric H_2O trends are assessed. The main approximations are the assumptions of (I) instantaneous stratospheric entry mixing ratio propagation, and (II) stationary AoA-FRF correlation.

The first part of the thesis presents the sensitivity studies to investigate the effects of TTL temperatures, horizontal transport and small-scale mixing on stratospheric H_2O mixing ratios. A number of sensitivity simulations using CLaMS in its 3D-version were carried out. The CLaMS run, driven by ERA-Interim reanalysis data was considered as the reference. For investigating the effects of different TTL temperatures on stratospheric H_2O mixing ratios, a CLaMS simulation driven by JRA-55 was performed. For assessing the effects of horizontal transport on stratospheric H_2O, CLaMS sensitivity simulations with artificial horizontal transport barriers along latitude circles at the equator, at 15° N/S and at 35° N/S were carried out. For investigating the uncertainties of stratospheric H_2O with regard to different small-scale mixing schemes, the parameterized small-scale mixing strength in CLaMS was varied. The effects of TTL temperatures, horizontal transport and small-scale mixing on stratospheric H_2O, have been estimated through the comparison of the CLaMS sensitivity simulations with the ERA-Interim-based reference simulation.

A substantial uncertainty in simulating stratospheric H_2O stems from uncertainties in TTL temperatures between the different reanalysis products, even when using the recent reanalyses. Suppressing of horizontal transport with artificial horizontal transport barriers in the model, changes the stratospheric H_2O mixing ratios up to around 1 ppmv, whereas different strength in small-scale mixing cause an uncertainty of about 0.8 ppmv. The main results are formulated to answer the following questions:

- *How robust is simulated stratospheric H_2O with respect to different TTL temperatures in current meteorological datasets?*
  There is a significant uncertainty in simulated H_2O, even when using the most recent reanalysis products (such as ERA-Interim and JRA-55). Differences in H_2O between CLaMS simulations driven by ERA-Interim and JRA-55 reanalyses amount to about

0.5 ppmv throughout the stratosphere. The main reason for JRA-55 causing a moister stratosphere when compared to the ERA-Interim is the positive difference (on average about 2 K) in the temperatures around the tropopause.

- *How large is the effect of horizontal transport on stratospheric H_2O?*
  Sensitivity simulations with introduced artificial transport barriers in CLaMS (which suppress certain horizontal transport pathways) showed only a weak effect of interhemispheric transport. Similarly, the sensitivity simulation with a subtropical transport barrier at 35° N/S showed that in-mixing of mid-latitude air has only a weak impact on global stratospheric H_2O; it is due to "out-mixing" of moist tropical air. In contrast, the NH subtropics have a strong moistening effect on global stratospheric H_2O, and it is a critical source region of moisture, which is likely related to the subtropical monsoon circulations. Furthermore, it was shown that a weak moistening effect from the SH subtropics exists as well. The effect of horizontal transport on the SH is small in all sensitivity simulations, because stratospheric H_2O mixing ratios in the SH are strongly affected by local freeze-drying at SH high-latitudes.

- *How sensitive is stratospheric H_2O to atmospheric small-scale mixing?*
  Small-scale mixing mainly increases troposphere-stratosphere exchange, causing an enhancement of stratospheric H_2O, particularly along the subtropical jets in the summer hemisphere and in the NH monsoon regions. In particular, the Asian and American monsoon systems during boreal summer are very sensitive to changes in small-scale mixing, which appears to be crucial for controlling the moisture anomalies in the monsoon UTLS. For the sensitivity simulation with varied mixing strength, differences in tropical entry H_2O between the weak and strong mixing cases amount to about 1 ppmv. Above about 430 K, increased model small-scale mixing causes a complex interplay between vertical and horizontal mixing, which results in either moistening or drying of the stratosphere depending on the mixing strength.

The second part of the thesis evaluated the methods of AoA trends estimation from stratospheric H_2O changes, using approximations I and II. Sensitivity studies with CLaMS have been performed: with approximations I and II (APPROX); with only approximation II (C-CORR); with using the correct entry mixing ratios (calculated though the propagation by age spectrum) and the non-stationary AoA-FRF correlation (FULL). The sensitivity experiments were analyzed through comparison with the reference CLaMS AoA trend. The main results are formulated to answer the following questions:

- *How reliable are estimated AoA trends from stratospheric H_2O changes?*
  The APPROX method showed noticeable differences in the derived mean AoA trend when compared with the "true" AoA trend from CLaMS reference simulation, but these differences are strongly dependent on the considered period. The results show that both approximations I and II are important for calculating AoA trend; and they affect the estimated AoA trend similarly strong (causing the discrepancies of up to 5 % per decade above 600 K, and even higher discrepancies below 600 K). For some periods, the overall resulting mean AoA trend patterns showed clear differences, which occurred particularly

in the exact strength of the trends and in the detailed structures. In specific regions of the stratosphere, the derived mean AoA trends from APPROX were even different in sign, resulting in different pictures of BDC changes. However, for the long 1990-2017 period, the estimated AoA trend with APPROX was comparably well represented. In this case, the effects from approximations I and II were opposite, and canceled out, resulting in a good estimate of the AoA trend.

Outlook

The sensitivity studies presented in the thesis provide new insights into the leading processes that control stratospheric H_2O and its trends. The findings are important for assessing and improving climate model projections. Moreover, the results from the performed CLaMS sensitivity simulations (shown in the first part of the thesis) may help to interpret the uncertainties of simulated stratospheric H_2O, and to identify deficits in climate models. The results from the sensitivity experiments within CLaMS shown in the second part of the thesis are useful for assessing the uncertainty in estimates of stratospheric circulation and BDC changes from global satellite measurements of stratospheric H_2O.

The research of this thesis can be extended for investigating other important aspects defining stratospheric H_2O: TTL temperatures uncertainties from the newest reanalyses (in particular, employing the ERA-5 reanalysis which will replace ERA-Interim in the future) and their impact on stratospheric H_2O; artificial horizontal transport barriers can be applied for investigating the interhemispheric asymmetry, as well as Antarctic dehydration and transport at the poles; different small-scale mixing schemes may be used in order to study separately horizontal and vertical transport. The studies of defining AoA trends may be further continued with defining in detail the AoA-FRF correlation function; also, the method of AoA trend estimation could be improved in order to apply it to satellite measurements (e.g., CH_4).

Appendix A

Validation of the CLaMS simulations

In order to study the robustness of our conclusions concerning changes in the simulation period, we carried out some of the simulations for the entire period between 2011 and 2014. Figure A.1 shows the distribution of zonal mean H_2O mixing ratios for this period for the reference (a) and horizontal barrier simulations with barriers at 15° N/S (b) and 35° N/S (c). Clearly, the differences between the different simulations with transport barriers stay qualitatively similar, when compared to the 2011 case (see Fig. 4.11). Although the results for the year 2011 appear slightly drier when compared to 2011-2014, this is likely related to the occurrence of La Niña in 2011.

The effects of increased small-scale mixing for 2011 (presented in Sec. 4.4) are consistent with the climatological data for the 2011-2014 period (Fig. A.2). Although, the effect of increased mixing strength appears even stronger for 2011-2014 (see Fig. 4.16d for comparison). As a conclusion, restricting the analysis of this study to a single year has no significant effect on our conclusions, which can be regarded as representative for the climatological case.

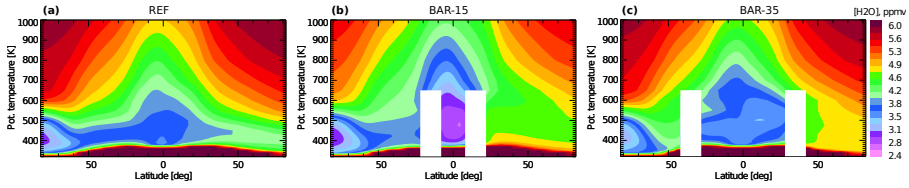

Figure A.1: Zonal mean H_2O distribution averaged over the period from 2011 to 2014. Shown data are from CLaMS sensitivity simulations for the reference (a) and the horizontal transport barrier simulations with barriers along 15° N/S (b) and 35° N/S (c). Barriers are set between the Earth's surface and the 600 K potential temperature levels and are represented in white.

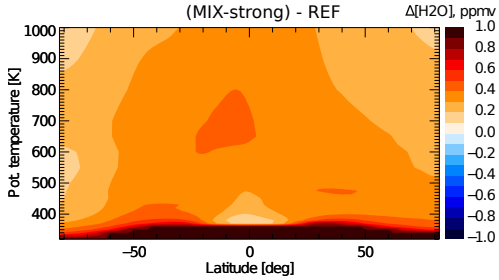

Figure A.2: Differences of zonal mean H_2O from CLaMS sensitivity simulations between reference (REF) and strong mixing (MIX-strong) cases averaged over the period from 2011 to 2014.

Appendix B

Impact of the dehydration at the poles on simulated stratospheric H_2O

When considering the conserved HH, we see the discrepancies between the propagated HH and the "true" CLaMS HH (Fig. 5.11e, f). The first reason for such discrepancies is the method's set-up (described in Sect. 5.4.3), in which the propagation by the age spectrum is performed monthly from the averaged boundary (between 390-400 K potential temperature, from 30° S to 30° N) causing uncertainties. Secondly, due to the propagation procedure, the dehydration processes are missing as well (especially, at the South pole).

In order to estimate the magnitude of the dehydration at the poles, we perform one additional sensitivity study with the turned off freeze-drying at high latitudes of 50° S-90° S and 50° N-90° N (shown 2011 in Fig. B.1b). From the difference between the REF H_2O and H_2O without the freeze-drying at the poles (Fig. B.1 c), we observe, that the polar dehydration impacts mainly SH, and has a global drying effect. Moreover, the effect of dehydration at the South pole is higher than 1 ppmv. Because of very cold winter 2011, there is a slight impact of the dehydration at the Northern pole as well. Thus, the polar dehydration effects must be taken into account when interpreting the differences between propagated HH and "true" CLaMS HH.

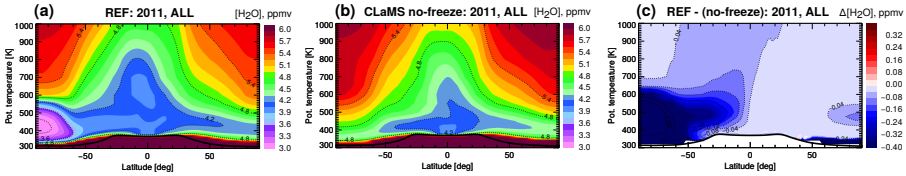

Figure B.1: Zonal mean H_2O distributions for 2011. Shown data are from CLaMS sensitivity simulations: (a) from the reference CLaMS simulation; (b) without dehydration at the poles (50° S-90° S and 50° N-90° N); (c) shows the absolute difference between CLaMS reference H_2O the H_2O without freeze-drying. Note, that CLaMS simulation driven by ERA-Interim reanalysis.

Appendix C

AoA-FRF correlation

An accurate AoA-FRF correlation function depends on many parameters, including time resolution, latitude, and altitude.

The relationship between AoA and FRF (estimated following FULL method) with regard to different latitude range (10° S-20° S, 10° S-10° N, 10° N-20° N) is shown in Fig. C.1. The AoA-FRF correlation functions are derived by a third-order polynomial fit for each considered range of latitudes. The AoA-FRF correlation functions are unique for each latitude range, because the differences in the magnitude of

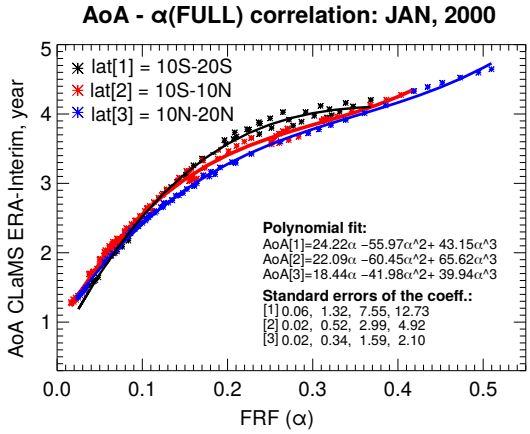

Figure C.1: Relationship between FRF (from FULL method) and CLaMS modelled AoA for January 2000, for three intervals of latitudes: between 10° S and 20° S (black line and black star-dots), 10° S-10° N (red line and red star-dots), 10° N-20° N (blue line and blue star-dots). For each interval, FRF and CLaMS (driven by ERA-Interim) AoA were taken as zonally averaged data between 450 and 1000 K (where FRF has positive values due to the method). At this plot, the relationship is shown by fitting third-order polynomial functions to the AoA-FRF distribution.

coefficients are out of the standard error's range. And, for instance, at the same FRF level of 0.25, the air at the Northern tropics (10° N-20° N) is younger than at the Southern tropics (10° S-20° S) for almost half a year. Also, there is a hemispheric difference in the FRF: at the Northern tropics FRF reaches 0.5, while at the Southern tropics the highest FRF value is close to 0.35.

Moreover, there are differences in the AoA-FRF correlation functions even in the range of the same latitudes, but at various heights (potential temperature levels). The different AoA-FRF relationships at 500 K and 700 K are shown in Fig. C.2, described by a linear fitting functions.

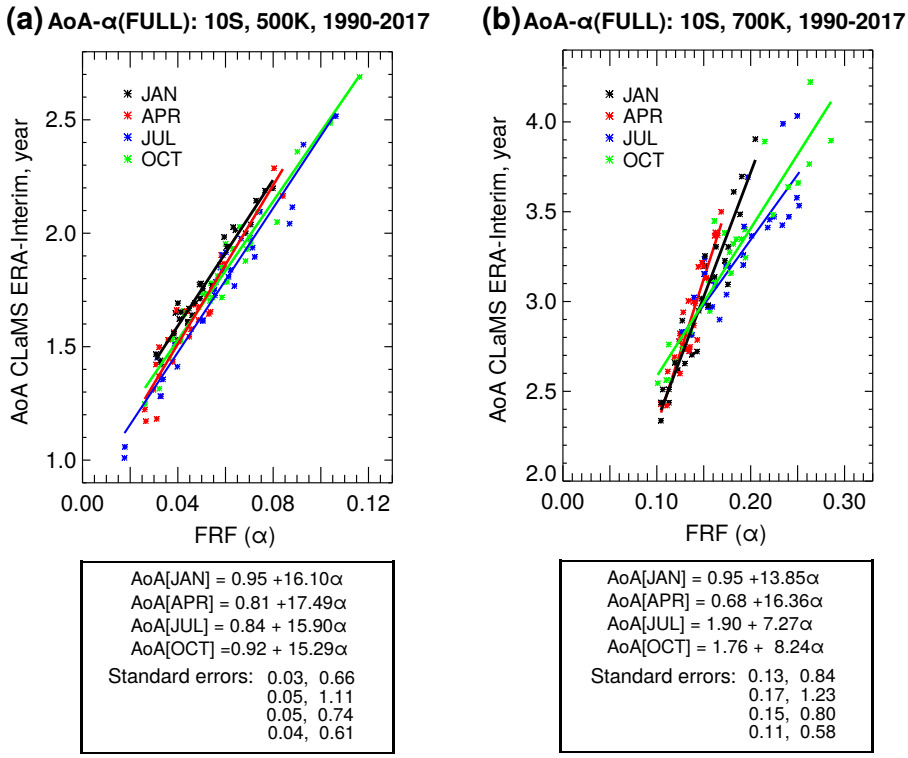

Figure C.2: Relationship between FRF (from FULL method) and CLaMS modelled AoA at the locations of 10° S at 500 K (a) and 700 K (b) potential temperature. At each sub-figure are shown linear correlation functions depending on the month (January in black line, April in red line, July in blue line, and October is shown with green line). The correlation points are taken from the monthly data through all the years between 1990 and 2017. For each represented month, FRF and CLaMS (driven by ERA-Interim) AoA were taken as zonally averaged data in potential temperature range between 450 and 1000 K (where FRF has positive values due to the method). At this plot, the relationship is shown by fitting linear functions to the AoA-FRF distribution.

Symbols and abbreviations

Acronym	Description
4DVar	4-dimensional variational analysis
ALL	annual mean
AoA	mean age of air
AP	air parcel
BDC	Brewer-Dobson circulation
BIER	Boundary Impulse (time-)Evolving
CCM	chemistry-climate model
DJF	December-January-February mean
ENSO	El Niño-Southern Oscillation
Ex-UTLS	extratropical upper troposphere and lower stratosphere
FRF	fractional release factor
GCM	general circulation model
HH	approximated total hydrogen
IR	infrared
JJA	June-July-August mean
LS	lower stratosphere
NH	Northern Hemisphere
PDF	probability density functions
QBO	quasi-biennial oscillations
SH	Southern Hemisphere
TTL	tropical tropopause layer
TWP	Tropical West Pacific
UTLS	upper troposphere and lower stratosphere
UV	ultraviolet

Symbol	Description	Value, unit
c_p	specific heat of dry air at a constant pressure	$1004\,\mathrm{J\,K^{-1}\,kg^{-1}}$
G	age spectrum	
K_z	vertical diffusivity	$\mathrm{m^2/s}$
L	chemical loss function	
l_c	characteristic sedimentation length	m
p	pressure	hPa
p_s	standard surface pressure	1000 hPa
Q	diabatic heating rate	K/day
R	gas constant for dry air	$287\,\mathrm{J\,kg^{-1}\,K^{-1}}$
r	distance	km
T	temperature	K
t	time	day
z	height	km
α	fractional release factor	
Γ	lapse rate	K/km
γ_c	critical deformation	
ζ	hybrid isentropic coordinate	
θ	potential temperature	K
λ_c	critical Lyapunov exponent	$\mathrm{day^{-1}}$
σ	orography following coordinate	
τ	mean age of air	year
χ	mixing ratio	ppmv
ψ	total hydrogen	ppmv

Chemical formula	Description
CH_4	methane
CO_2	carbon dioxide
H_2	molecular hydrogen
H_2O	liquid water
H_2SO_4	sulphuric acid
H_2SO_4/H_2O	diluted sulphuric acid
O_2	molecular oxygen

List of Figures

List of Tables

Bibliography

American Meteorological Society: Detrainment. Glossary of Meteorology. [Available online at http://glossary.ametsoc.org/wiki/Detrainment], a.

American Meteorological Society: Entrainment. Glossary of Meteorology. [Available online at http://glossary.ametsoc.org/wiki/Entrainment], b.

Afchine, A., Rolf, C., Costa, A., Spelten, N., Riese, M., Buchholz, B., Ebert, V., Heller, R., Kaufmann, S., Minikin, A., Voigt, C., Zöger, M., Smith, J., Lawson, P., Lykov, A., Khaykin, S., and Krämer, M.: Ice particle sampling from aircraft – influence of the probing position on the ice water content, Atmos. Meas. Tech., 11, 4015–4031, https://doi.org/10.5194/amt-11-4015-2018, 2018.

Allen, D. C., Haigh, J. D., Houghton, J. T., and Simpson, C. J. S. M.: Radiative cooling near the mesopause, Nature, 281, 660–661, https://doi.org/10.1038/281660a0, 1979.

Andrews, D., Holton, J., and Leovy, C.: Middle Atmosphere Dynamics, International geophysics series, Academic Press, San Diego, USA, 1987.

Andrews, D. G. and McIntyre, M. E.: An exact theory of nonlinear waves on a Lagrangian-mean flow, Journal of Fluid Mechanics, 89, 609–646, https://doi.org/10.1017/S0022112078002773, 1978.

Archer, D. and Brovkin, V.: The millennial atmospheric lifetime of anthropogenic CO_2, Clim. Change, 90, 283–297, https://doi.org/10.1007/s10584-008-9413-1, 2008.

Avery, M. A., Davis, S. M., Rosenlof, K. H., Ye, H., and Dessler, A. E.: Large anomalies in lower stratospheric water vapour and ice during the 2015-2016 El Niño, Nat. Geosci., 10, 405–410, https://doi.org/10.1038/ngeo2961, 2017.

Baldwin, M., Gray, L., Dunkerton, T., Hamilton, K., Haynes, P., Randel, W., Holton, J., Alexander, M., Hirota, I., Horinouchi, T., Jones, D., Kinnersley, J., Marquardt, C., Sato, K., and Takahashi, M.: The quasi-biennial oscillation, Rev. Geophys., 39, 179–229, https://doi.org/10.1029/1999RG000073, 2001.

Bannister, R. N., O'Neill, A., Gregory, A. R., and Nissen, K. M.: The role of the south-east Asian monsoon and other seasonal features in creating the "tape-recorder" signal in the Unified Model, Q. J. R. Meteorol. Soc., 130, 1531–1554, https://doi.org/10.1256/qj.03.106, 2004.

Basha, G., Kishore, P., Ratnam, M. V., Ravindra Babu, S., Velicogna, I., Jiang, J. H., and Ao, C. O.: Global climatology of planetary boundary layer top obtained from multi-satellite GPS RO observations, Clim. Dyn., 52, 2385–2398, https://doi.org/10.1007/s00382-018-4269-1, 2019.

Bernath, P.: The Atmospheric Chemistry Experiment (ACE), J. Quant. Spectr. Radiat. Transfer, 186, 3–16, https://doi.org/10.1016/j.jqsrt.2016.04.006, 2017.

Bernath, P. F., McElroy, C. T., Abrams, M. C., Boone, C. D., Butler, M., Camy-Peyret, C., Carleer, M., Clerbaux, C., Coheur, P.-F., Colin, R., DeCola, P., DeMazière, M., Drummond, J. R., Dufour, D., Evans, W. F. J., Fast, H., Fussen, D., Gilbert, K., Jennings, D. E., Llewellyn, E. J., Lowe, R. P., Mahieu, E., McConnell, J. C., McHugh, M., McLeod, S. D., Michaud, R., Midwinter, C., Nassar, R., Nichitiu, F., Nowlan, C., Rinsland, C. P., Rochon, Y. J., Rowlands, N., Semeniuk, K., Simon, P., Skelton, R., Sloan, J. J., Soucy, M.-A., Strong, K., Tremblay, P., Turnbull, D., Walker, K. A., Walkty, I., Wardle, D. A., Wehrle, V., Zander, R., and Zou, J.: Atmospheric Chemistry Experiment (ACE): Mission overview, Geophys. Res. Lett., 32, L15S01, https://doi.org/10.1029/2005GL022386, 2005.

Berrisford, P., Dee, D., Fielding, K., Fuentes, M., Kallberg, P., Kobayashi, S., and Uppala, S.: The ERA-Interim archive: Version 1.0, ERA Report, European Centre for Medium Range Weather Forecasts, Shinfield Park, Reading, 2009.

Berrisford, P., Dee, D., Poli, P., Brugge, R., Fielding, M., Fuentes, M., Kallberg, P., Kobayashi, S., Uppala, S., and Simmons, A.: The ERA-Interim archive: Version 2.0, ERA Report, European Centre for Medium Range Weather Forecasts, Shinfield Park, Reading, 2011.

Birner, T. and Bönisch, H.: Residual circulation trajectories and transit times into the extratropical lowermost stratosphere, Atmos. Chem. Phys., 11, 817–827, https://doi.org/10.5194/acp-11-817-2011, 2011.

Blunden, J. and Arndt, D. S.: Global Climate. Overview (Chapter 2 of "State of the Climate in 2016"), Bull. Amer. Meteor. Soc., 98, S5–S10, https://doi.org/10.1175/2017BAMSStateoftheClimate.1, 2017.

Boehm, M. T. and Lee, S.: The Implications of Tropical Rossby Waves for Tropical Tropopause Cirrus Formation and for the Equatorial Upwelling of the Brewer-Dobson Circulation, J. Atmos. Sci., 60, 247–261, https://doi.org/10.1175/1520-0469(2003)060<0247:TIOTRW>2.0.CO;2, 2003.

Brasseur, G. P., Prinn, R. G., and Pszenny, A.: Atmospheric Chemistry in a Changing World, Springer, Heidelberg, Germany, https://doi.org/10.1007/978-3-642-18984-5, 2003.

Brewer, A. W.: Evidence for a world circulation provided by the measurements of helium and water vapour distribution in the stratosphere, Q. J. R. Meteorol. Soc., 75, 351–363, https://doi.org/10.1002/qj.49707532603, 1949.

Bunzel, F. and Schmidt, H.: The Brewer-Dobson Circulation in a Changing Climate: Impact of the Model Configuration, J. Atmos. Sci., 70, 1437–1455, https://doi.org/10.1175/JAS-D-12-0215.1, 2013.

Butchart, N.: The Brewer-Dobson circulation, Rev. Geophys., 52, 157–184, https://doi.org/10.1002/2013RG000448, 2014.

Butchart, N. and Scaife, A.: Removal of chlorofluorocarbons by increased mass exchange between the stratosphere and troposphere in a changing climate, Nature, 410, 799–802, https://doi.org/10.1038/35071047, 2001.

Butchart, N., Scaife, A. A., Bourqui, M., de Grandpre, J., Hare, S. H. E., Kettleborough, J., Langematz, U., Manzini, E., Sassi, F., Shibata, K., Shindell, D., and Sigmond, M.: Simulations of anthropogenic change in the strength of the Brewer-Dobson circulation, Clim. Dyn., 27, 727–741, https://doi.org/10.1007/s00382-006-0162-4, 2006.

Butchart, N., Cionni, I., Eyring, V., Shepherd, T., Waugh, D., Akiyoshi, H., Austin, J., Brühl, C., Chipperfield, M., Cordero, E., Dameris, M., Deckert, R., Dhomse, S., Frith, S., Garcia, R., Gettelman, A., Giorgetta, M., Kinnison, D., Li, F., Mancini, E., McLandress, C., Pawson, S., Pitari, G., Plummer,

D., Rozanov, E., Sassi, F., Scinocca, J., Shibata, K., Steil, B., and Tian, W.: Chemistry-climate model simulations of 21st century stratospheric climate and circulation changes, J. Climate, 23, 5349–5374, https://doi.org/10.1175/2010JCL13404.1, 2010.

Butler, A. H. and Polvani, L. M.: El Niño, La Niña, and stratospheric sudden warmings: A reevaluation in light of the observational record, Geophys. Res. Lett., 38, https://doi.org/10.1029/2011GL048084, 2011.

Calvert, J. G.: Glossary of atmospheric chemistry terms (Recommendations 1990), vol. 62(11), pp. 2167–2219, De Gruyter, https://doi.org/10.1351/pac199062112167, 1990.

Chang, P. and Zebiak, S.: Tropical Meteorology and Climate | El Niño and the Southern Oscillation: Theory, in: Encyclopedia of Atmospheric Sciences (Second Edition), edited by North, G. R., Pyle, J., and Zhang, F., pp. 97–101, Academic Press, Oxford, second edition edn., https://doi.org/10.1016/B978-0-12-382225-3.00149-3, 2015.

Chu, W. P., Chiou, E. W., Larsen, J. C., Thomason, L. W., Rind, D., Buglia, J. J., Oltmans, S., McCormick, M. P., and McMaster, L. M.: Algorithms and sensitivity analyses for Stratospheric Aerosol and Gas Experiment II water vapor retrieval, J. Geophys. Res.-Atmos., 98, 4857–4866, https://doi.org/10.1029/92JD01628, 1993.

Davis, S. M., Hegglin, M. I., Fujiwara, M., Dragani, R., Harada, Y., Kobayashi, C., Long, C., Manney, G. L., Nash, E. R., Potter, G. L., Tegtmeier, S., Wang, T., Wargan, K., and Wright, J. S.: Assessment of upper tropospheric and stratospheric water vapor and ozone in reanalyses as part of S-RIP, Atmospheric Chemistry and Physics, 17, 12 743–12 778, https://doi.org/10.5194/acp-17-12743-2017, 2017.

Dee, D. P., Uppala, S. M., Simmons, A. J., Berrisford, P., Poli, P., Kobayashi, S., Andrae, U., Balmaseda, M. A., Balsamo, G., Bauer, P., Bechtold, P., Beljaars, A. C. M., van de Berg, L., Bidlot, J., Bormann, N., Delsol, C., Dragani, R., Fuentes, M., Geer, A. J., Haimberger, L., Healy, S. B., Hersbach, H., Hólm, E. V., Isaksen, L., Kallberg, P., Koehler, M., Matricardi, M., McNally, A. P., Monge-Sanz, B. M., Morcrette, J.-J., Park, B.-K., Peubey, C., de Rosnay, P., Tavolato, C., ThÃl'paut, J.-N., and Vitart, F.: The ERA-Interim reanalysis: configuration and performance of the data assimilation system, Q. J. R. Meteorol. Soc., 137, 553–597, https://doi.org/10.1002/qj.828, 2011.

Dessler, A. and Zelinka, M.: Climate and climate change | Climate Feedbacks, in: Encyclopedia of Atmospheric Sciences (Second Edition), edited by North, G. R., Pyle, J., and Zhang, F., pp. 18–25, Academic Press, Oxford, second edition edn., https://doi.org/10.1016/B978-0-12-382225-3.00471-0, 2015.

Dessler, A., Schoeberl, M., Wang, T., Davis, S., and Rosenlof, K.: Stratospheric water vapor feedback, Proc. Nat. Acad. Sci., 110, 18 087–18 091, https://doi.org/10.1073/pnas.1310344110, 2013.

Dessler, A. E. and Wong, S.: Estimates of the Water Vapor Climate Feedback during El NiñoâĂŞSouthern Oscillation, J. Climate, 22, 6404–6412, https://doi.org/10.1175/2009JCLI3052.1, 2009.

Dessler, A. E., Weinstock, E. M., Hintsa, E. J., Anderson, J. G., Webster, C. R., May, R. D., Elkins, J. W., and Dutton, G. S.: An examination of the total hydrogen budget of the lower stratosphere, Geophys. Res. Lett., 21, 2563–2566, https://doi.org/10.1029/94GL02283, 1994.

Dessler, A. E., Schoeberl, M. R., Wang, T., Davis, S. M., Rosenlof, K. H., and Vernier, J.-P.: Variations of stratospheric water vapor over the past three decades, J. Geophys. Res.-Atmos., 119, 12 588–12 598, https://doi.org/10.1002/2014JD021712, 2014.

Dickinson, R. E.: Rossby Waves–Long-Period Oscillations of Oceans and Atmospheres, Annual Review of Fluid Mechanics, 10, 159–195, https://doi.org/10.1146/annurev.fl.10.010178.001111, 1978.

Dobson, G. M. B.: Origin and distribution of polyatomic molecules in the atmosphere, Proceedings of the Royal Society of London A: Mathematical, Physical and Engineering Sciences, 236, 187–193, https://doi.org/10.1098/rspa.1956.0127, 1956.

Dobson, G. M. B. and Harrison, D. N.: Measurements of the amount of ozone in the Earth's atmosphere and its relation to other geophysical conditions, Proceedings of the Royal Society of London A: Mathematical, Physical and Engineering Sciences, 110, 660–693, https://doi.org/10.1098/rspa.1926.0040, 1926.

Dobson, G. M. B., Harrison, D. N., and Lawrence, J.: Measurements of the amount of ozone in the Earth's atmosphere and its relation to other geophysical conditions. Part III, Proc. R. Soc. London A, 122, 456–486, https://doi.org/10.1098/rspa.1929.0034, 1929.

Dunkerton, T. J.: On the Mean Meridional Mass Motions of the Stratosphere and Mesosphere, J. Atmos. Sci., 35, 2325–2333, https://doi.org/10.1175/1520-0469(1978)035<2325:OTMMMM>2.0.CO;2, 1978.

Easterbrook, D.: Chapter 9 – Greenhouse Gases, in: Evidence-Based Climate Science (Second Edition), edited by Easterbrook, D., pp. 163–173, Elsevier, https://doi.org/10.1016/B978-0-12-804588-6.00009-4, 2016.

Ebita, A., Kobayashi, S., Ota, Y., Moriya, M., Kumabe, R., Onogi, K., Harada, Y., Yasui, S., Miyaoka, K., Takahashi, K., Kamahori, H., Kobayashi, C., Endo, H., Soma, M., Oikawa, Y., and Ishimizu, T.: The Japanese 55-year Reanalysis "JRA-5": An Interim Report, SOLA, 7, 149–152, https://doi.org/10.2151/sola.2011-038, 2011.

Engel, A., Möbius, T., Bönisch, H., Schmidt, U., Heinz, R., Levin, I., Atlas, E., Aoki, S., Nakazawa, T., Sugawara, S., Moore, F., Hurst, D., Elkins, J., Schauffler, S., Andrews, A., and Boering, K.: Age of stratospheric air unchanged within uncertainties over the past 30 years, Nat. Geosci., 2, 28–31, https://doi.org/10.1038/ngeo388, 2009.

Engel, A., Bönisch, H., Ullrich, M., Sitals, R., Membrive, O., Danis, F., and Crevoisier, C.: Mean age of stratospheric air derived from AirCore observations, Atmos. Chem. Phys., 17, 6825–6838, https://doi.org/10.5194/acp-17-6825-2017, 2017.

Eyring, V., Harris, N. R. P., Rex, M., Shepherd, T. G., Fahey, D. W., Amanatidis, G. T., Austin, J., Chipperfield, M. P., Dameris, M., Forster, P., Graf, H. F., Nagashima, T., Newman, P. A., Pawson, S., Prather, M. J., Pyle, J. A., Salawitch, R. J., Santer, B. D., and Waugh, D. W.: A Strategy for Process-Oriented Validation of Coupled Chemistry-Climate Models, Bull. Am. Meteorol. Soc., 86, 1117–1134, https://doi.org/10.1175/BAMS-86-8-1117, 2005.

Fischer, H., Birk, M., Blom, C., Carli, B., Carlotti, M., von Clarmann, T., Delbouille, L., Dudhia, A., Ehhalt, D., Endemann, M., Flaud, J. M., Gessner, R., Kleinert, A., Koopmann, R., Langen, J., López-Puertas, M., Mosner, P., Nett, H., Oelhaf, H., Perron, G., Remedios, J., Ridolfi, M., Stiller, G., , and Zander, R.: MIPAS: An instrument for atmospheric and climate resaerch, Atmos. Chem. Phys., 8, https://doi.org/10.5194/acp-8-2151-2008, 2008.

Flury, T., Wu, D. L., and Read, W. G.: Variability in the speed of the Brewer-Dobson circulation as observed by Aura/MLS, Atmos. Chem. Phys., 13, 4563–4575, https://doi.org/10.5194/acp-13-4563-2013, 2013.

Folkins, I. and Martin, R. V.: The vertical structure of tropical convection and its impact on the budget of water vapor and ozone, J. Atmos. Chem., 62, 1560–1573, https://doi.org/10.1175/JAS3407.1, 2005.

Forster, P. and Shine, K. P.: Stratospheric water vapour change as possible contributor to observed stratospheric cooling, Geophys. Res. Lett., 26, 3309–3312, https://doi.org/10.1029/1999GL010487, 1999.

Forster, P. and Shine, K. P.: Assessing the climate impact of trends in stratospheric water vapor, Geophys. Res. Lett., 29, 1086, https://doi.org/10.1029/2001GL013909, 2002.

Frank, F., Jöckel, P., Gromov, S., and Dameris, M.: Investigating the yield of H_2O and H_2 from methane oxidation in the stratosphere, Atmos. Chem. Phys., 18, 9955–9973, https://doi.org/10.5194/acp-18-9955-2018, 2018.

Fueglistaler, S.: Stepwise changes in stratospheric water vapor?, J. Geophys. Res.-Atmos., 117, https://doi.org/10.1029/2012JD017582, 2012.

Fueglistaler, S. and Haynes, P. H.: Control of interannual and longer-term variability of stratospheric water vapor, J. Geophys. Res., 110, D24108, https://doi.org/10.1029/2005JD006019, 2005.

Fueglistaler, S., Wernli, H., and Peter, T.: Tropical troposphere-to-stratosphere transport inferred from trajectory calculations, J. Geophys. Res., 109, D03108, https://doi.org/10.1029/2003JD004069, 2004.

Fueglistaler, S., Bonazzola, M., Haynes, P. H., and Peter, T.: Stratospheric water vapor predicted from the Lagrangian temperature history of air entering the stratosphere in the tropics, J. Geophys. Res., 110, D08107, https://doi.org/10.1029/2004JD005516, 2005.

Fueglistaler, S., Dessler, A. E., Dunkerton, T. J., Folkins, I., Fu, Q., and Mote, P. W.: Tropical tropopause layer, Rev. Geophys., 47, RG1004, https://doi.org/10.1029/2008RG000267, 2009.

Fueglistaler, S., Liu, Y., Flannaghan, T., Haynes, P., Dee, D., Read, W., Remsberg, E., Thomason, L., Hurst, D., Lanzante, J., and Bernath, P.: The relation between atmospheric humidity and temperature trends for stratospheric water, J. Geophys. Res., 118, 1052–1074, https://doi.org/10.1002/jgrd.50157, 2013.

Garcia, R. R. and Randel, W. J.: Acceleration of Brewer-Dobson circulation due to increase in greenhouse gases, J. Atmos. Sci., 65, 2731–2739, https://doi.org/10.1175/2008JAS2712.1, 2008.

Garcia, R. R., Randel, W. J., and Kinnison, D. E.: On the Determination of Age of Air Trends from Atmospheric Trace Species, J. Atmos. Sci., 68, 139–154, https://doi.org/10.1175/2010JAS3527.1, 2011.

Garfinkel, C. I., Aquila, V., Waugh, D. W., and Oman, L. D.: Time-varying changes in the simulated structure of the Brewer–Dobson Circulation, Atmos. Chem. Phys., 17, 1313–1327, https://doi.org/10.5194/acp-17-1313-2017, 2017.

Garny, H., Birner, T., Bönisch, H., and Bunzel, F.: The effects of mixing on Age of Air, J. Geophys. Res., 119, 7015–7034, https://doi.org/10.1002/2013JD021417, 2014.

Gastineau, G., Li, L., and Le Treut, H.: The Hadley and Walker Circulation Changes in Global Warming Conditions Described by Idealized Atmospheric Simulations, J. Climate, 22, 3993–4013, https://doi.org/10.1175/2009JCLI2794.1, 2009.

Gerber, E. P., Butler, A., Calvo, N., Charlton-Perez, A., Giorgetta, M., Manzini, E., Perlwitz, J., Polvani, L. M., Sassi, F., Scaife, A. A., Shaw, T. A., Son, S.-W., and Watanabe, S.: Assessing and Understanding the Impact of Stratospheric Dynamics and Variability on the Earth System, Bull. Amer. Meteor. Soc., 93, 845–859, https://doi.org/10.1175/BAMS-D-11-00145.1, 2012.

Gettelman, A., Hegglin, M. I., Son, S.-W., Birner, J. K. M. F. T., Kremser, S., Rex, M., Añel, J. A., Akiyoshi, H., Austin, J., Bekki, S., Braesicke, P., Brühl, C., Butchart, N., Chipperfield, M., Dameris, M., Dhomse, S., Garny, H., Hardiman, S., Jöckel, P., Kinnison, D., Lamarque, J. F., Mancini, E., Marchand, M., Michou, M., Morgenstern, O., Pawson, S., Pitari, G., Plummer, D. A., Pyle, J., Rozanov, E., Scinocca, J., Shepherd, T. G., Shibata, K., Smale, D., Teyssedre, H., and Tian, W.: Multi-model Assessment of the Upper Troposphere and Lower Stratosphere: Tropics and Global Trends, J. Geophys. Res., 115, D00M08, https://doi.org/10.1029/2009JD013638, 2010.

Gettelman, A., Hoor, P., Pan, L. L., Randel, W. J., Hegglin, M. I., and Birner, T.: The extratropical upper troposphere and lower stratosphere, Rev. Geophys., 49, RG3003, https://doi.org/10.1029/2011RG000355, 2011.

Giorgetta, M. A. and Bengtsson, L.: Potential role of the quasi-biennial oscillation in the stratosphere-troposphere exchange as found in water vapor in general circulation model experiments, J. Geophys. Res.-Atmos., 104, 6003–6019, https://doi.org/10.1029/1998JD200112, 1999.

Glanville, A. A. and Birner, T.: Role of vertical and horizontal mixing in the tape recorder signal near the tropical tropopause, Atmos. Chem. Phys., 17, 4337–4353, https://doi.org/10.5194/acp-17-4337-2017, 2017.

Grotjahn, R.: General circulation of the atmosphere | Mean Characteristics, in: Encyclopedia of Atmospheric Sciences (Second Edition), edited by North, G. R., Pyle, J., and Zhang, F., pp. 73–89, Academic Press, Oxford, second edition edn., https://doi.org/10.1016/B978-0-12-382225-3.00154-7, 2015.

Hall, E. G., Jordan, A. F., Hurst, D. F., Oltmans, S. J., Vömel, H., Kühnreich, B., and Ebert, V.: Advancements, measurement uncertainties, and recent comparisons of the NOAA frost point hygrometer, Atmos. Meas. Tech., 9, 4295–4310, https://doi.org/10.5194/amt-9-4295-2016, 2016.

Hall, T. M. and Plumb, R. A.: Age as a diagnostic of stratospheric transport, J. Geophys. Res., 99, 1059–1070, https://doi.org/10.1029/93JD03192, 1994.

Hall, T. M. and Waugh, D. W.: Timescales for the stratospheric circulation derived from tracers, J. Geophys. Res.-Atmos., 102, 8991–9001, https://doi.org/10.1029/96JD03713, 1997.

Harries, J.: Stratospheric chemistry topics | Hydrogen Budget, in: Encyclopedia of Atmospheric Sciences (Second Edition), edited by North, G. R., Pyle, J., and Zhang, F., pp. 238–241, Academic Press, Oxford, second edition edn., https://doi.org/https://doi.org/10.1016/B978-0-12-382225-3.00388-1, 2015.

Hartmann, D., Klein Tank, A., Rusticucci, M., Alexander, L., Brönnimann, S., Charabi, Y., Dentener, F., Dlugokencky, E., Easterling, D., Kaplan, A., Soden, B., Thorne, P., Wild, M., and Zhai, P.: Observations: Atmosphere and surface, in: Climate Change 2013 the Physical Science Basis: Working Group I Contribution to the Fifth Assessment Report of the Intergovernmental Panel on Climate Change, pp. 159–254, Cambridge University Press, https://doi.org/10.1017/CBO9781107415324.008, 2013.

Hauck, M., Fritsch, F., Garny, H., and Engel, A.: Deriving stratospheric age of air spectra using an idealized set of chemically active trace gases, Atmos. Chem. Phys., 19, 5269–5291, https://doi.org/10.5194/acp-19-5269-2019, 2019.

Haynes, P. and Anglade, J.: The vertical scale cascade in atmospheric tracers due to large-scale differential advection, J. Atmos. Sci., 54, 1121–1136, https://doi.org/10.1175/1520-0469(1997)054<1121:TVSCIA>2.0.CO;2, 1997.

Haynes, P. H., Marks, C. J., McIntyre, M. E., Shepherd, T. G., and Shine, K. P.: On the "downward control" of extratropical diabatic circulations by eddy-induced mean zonal forces., J. Atmos. Sci., 48, 651–678, 1991.

Hegglin, M. I., Brunner, D., Wernli, H., Schwierz, C., Martius, O., Hoor, P., Fischer, H., Spelten, N., Schiller, C., Krebsbach, M., Parchatka, U., Weers, U., Staehelin, J., and Peter, T.: Tracing troposphere-to-stratosphere transport above a mid-latitude deep convective system, Atmos. Chem. Phys., 4, 741–756, https://doi.org/10.5194/acp-4-741-2004, 2004.

Hegglin, M. I., Boone, C. D., Manney, G. L., Shepherd, T. G., Walker, K. A., Bernath, P. F., Daffer, W. H., Hoor, P., and Schiller, C.: Validation of ACE-FTS satellite data in the upper troposphere/lower stratosphere (UTLS) using non-coincident measurements, Atmos. Chem. Phys., 8, 1483–1499, https://doi.org/10.5194/acp-8-1483-2008, 2008.

Hegglin, M. I., Plummer, D. A., Shepherd, T. G., Scinocca, J. F., Anderson, J., Froidevaux, L., Funke, B., Hurst, D., Rozanov, A., Urban, J., von Clarmann, T., A.Walker, K., Wang, H. J., Tegtmeier, S., and Weigel, K.: Vertical structure of stratospheric water vapour trends derived from merged satellite data, Nat. Geosci., 7, 768–776, https://doi.org/10.1038/NGEO2236, 2014.

Held, I. M. and Soden, B. J.: Water Vapor Feedback and Global Warming, Ann. Rev. Energy Environ., 25, 441–475, https://doi.org/10.1146/annurev.energy.25.1.441, 2000.

Hoinka, K. P.: The tropopause: discovery, definition and demarcation, Meteorol. Z., 6, 281–303, https://doi.org/10.1127/metz/6/1997/281, 1997.

Holton, J.: Stratosphere-troposphere exchange | Global Aspects, pp. 2137–2143, Elsevier, https://doi.org/10.1016/B0-12-227090-8/00394-8, 2003.

Holton, J.: An Introduction to Dynamic Meteorology, An Introduction to Dynamic Meteorology, Elsevier Academic Press, Burlington, MA, 2004.

Holton, J. R.: Meridional Distribution of Stratospheric Trace Constituents, J. Atmos. Sci., 43, 1238–1242, https://doi.org/10.1175/1520-0469(1986)043<1238:MDOSTC>2.0.CO;2, 1986.

Holton, J. R. and Gettelman, A.: Horizontal transport and the dehydration of the stratosphere, Geophys. Res. Lett., 28, 2799–2802, 2001.

Holton, J. R., Haynes, P., McIntyre, M. E., Douglass, A. R., Rood, R. B., and Pfister, L.: Stratosphere-troposphere exchange, Rev. Geophys., 33, 403–439, https://doi.org/10.1029/95RG02097, 1995.

Holzer, M. and Hall, T. M.: Transit-time and tracer-age distributions in geophysical flows, J. Atmos. Sci., 57, 3539–3558, https://doi.org/10.1175/1520-0469(2000)057<3539:TTATAD>2.0.CO;2, 2000.

Hoor, P., Wernli, H., Hegglin, M. I., and Boenisch, H.: Transport timescales and tracer properties in the extratropical UTLS, Atmos. Chem. Phys., 10, 7929–7944, https://doi.org/10.5194/acp-10-7929-2010, 2010.

Hoppe, C. M., Hoffmann, L., Konopka, P., Grooß, J.-U., Ploeger, F., Günther, G., Jöckel, P., and Müller, R.: The implementation of the CLaMS Lagrangian transport core into the chemistry climate model EMAC 2.40.1: application on age of air and transport of long-lived trace species, Geosci. Model Dev., 7, 2639–2651, https://doi.org/10.5194/gmd-7-2639-2014, 2014.

Hori, K., Teed, R., and Jones, C.: The dynamics of magnetic Rossby waves in spherical dynamo simulations: A signature of strong-field dynamos?, Physics of the Earth and Planetary Interiors, 276, 68–85, https://doi.org/10.1016/j.pepi.2017.07.008, 2018.

Hoskins, B. J.: Towards a PV-θ view of the general circulation, Tellus A: Dynamic Meteorology and Oceanography, 43, 27–36, https://doi.org/10.3402/tellusa.v43i4.11936, 1991.

Hurst, D. F., Button, G. S., Romashkin, P. A., Wamsley, P. R., Moore, F. L., Elkins, L. W., Hintsa, E. J., and Weinstock, E. M.: Closure of the total hydrogen budget of the Northern Hemisphere extratropical lower stratosphere, J. Geophys. Res., 104, 8191–8200, https://doi.org/10.1029/1998JD100092, 1999.

Hurst, D. F., Oltmans, S. J., Vömel, H., Rosenlof, K. H., Davis, S. M., Ray, E. A., Hall, E. G., and Jordan, A. F.: Stratospheric water vapor trends over Boulder, Colorado: Analysis of the 30 year Boulder record, J. Geophys. Res., 116, D02306, https://doi.org/10.1029/2010JD015065, 2011.

James, R., Bonazzola, M., Legras, B., Surbled, K., and Fueglistaler, S.: Water vapor transport and dehydration above convective outflow during Asian monsoon, Geophys. Res. Lett., 35, L20810, https://doi.org/10.1029/2008GL035441, 2008.

Jensen, E. and Pfister, L.: Transport and freeze-drying in the tropical tropopause layer, J. Geophys. Res., 109, https://doi.org/10.1029/2003JD004022, 2004.

Jensen, E., Pfister, L., Bui, T., Weinheimer, A., Weinstock, E., Smith, J., Pittman, J., Baumgardner, D., Lawson, P., and McGill, M. J.: Formation of a tropopause cirrus layer observed over Florida during CRYSTAL-FACE, J. Geophys. Res.-Atmos., 110, https://doi.org/10.1029/2004JD004671, d03208, 2005.

Jensen, E. J., Pfister, L., and Bui, T. P.: Physical processes controlling ice concentrations in cold cirrus near the tropical tropopause, J. Geophys. Res.-Atmos., 117, D11205, https://doi.org/10.1029/2011JD017319, 2012.

Jones, R. L., Pyle, J. A., Harries, J. E., Zavody, A. M., Russell III, J. M., and Gille, J. C.: The water vapour budget of the stratosphere studied using LIMS and SAMS satellite data, Q. J. R. Meteorol. Soc., 112, 1127–1143, https://doi.org/10.1002/qj.49711247412, 1986.

Kang, S. and Ahn, J.-B.: Global energy and water balances in the latest reanalyses, Asia-Pac. J. Atmos. Sci., 51, 293–302, https://doi.org/10.1007/s13143-015-0079-0, 2015.

Kaufmann, S., Voigt, C., Jurkat, T., Thornberry, T., Fahey, D. W., Gao, R.-S., Schlage, R., Schäuble, D., and Zöger, M.: The airborne mass spectrometer AIMS – Part 1: AIMS-H_2O for UTLS water vapor measurements, Atmos. Meas. Tech., 9, 939–953, https://doi.org/10.5194/amt-9-939-2016, 2016.

Khosrawi, F., Grooß, J.-U., Müller, R., Konopka, P., Kouker, W., Ruhnke, R., Reddmann, T., and Riese, M.: Intercomparison between Lagrangian and Eulerian simulation of the development of mid-latitude streamers as observed by CRISTA, Atmos. Chem. Phys., 5, 85–95, https://doi.org/10.5194/acp-5-85-2005, 2005.

Kim, J.-E. and Alexander, M. J.: Direct impacts of waves on tropical cold point tropopause temperature, Geophys. Res. Lett., 42, 1584–1592, https://doi.org/10.1002/2014GL062737, 2015.

Kindel, B. C., Pilewskie, P., Schmidt, K. S., Thornberry, T., Rollins, A., and Bui, T.: Upper-troposphere and lower-stratosphere water vapor retrievals from the 1400 and 1900 nm water vapor bands, Atmos. Meas. Tech., 8, 1147–1156, https://doi.org/10.5194/amt-8-1147-2015, 2015.

Kobayashi, S., Ota, Y., Harada, Y., Ebita, A., Moriya, M., Onoda, H., Onogi, K., Kamahori, H., Kobayashi, C., Endo, H., Miyaoka, K., and Takahashi, K.: The JRA-55 Reanalysis: General Specifications and Basic Characteristics, Meteor. Soc. Japan, 93, 5–48, https://doi.org/10.2151/jmsj.2015-001, 2015.

Konopka, P. and Pan, L. L.: On the mixing-driven formation of the Extratropical Transition Layer (ExTL), J. Geophys. Res., 117, D18301, https://doi.org/10.1029/2012JD017876, 2012.

Konopka, P., Grooß, J. U., Günther, G., McKenna, D. S., Müller, R., Elkins, J. W., Fahey, D., and Popp, P.: Weak impact of mixing on chlorine deactivation during SOLVE/THESEO2000: Lagrangian modeling (CLaMS) versus ER-2 in situ observations., J. Geophys. Res., 108, 8324, https://doi.org/10.1029/2001JD000876, 2003.

Konopka, P., Steinhorst, H.-M., Grooß, J.-U., Günther, G., Müller, R., Elkins, J. W., Jost, H.-J., Richard, E., Schmidt, U., Toon, G., and McKenna, D. S.: Mixing and Ozone Loss in the 1999-2000 Arctic Vortex: Simulations with the 3-dimensional Chemical Lagrangian Model of the Stratosphere (CLaMS), J. Geophys. Res., 109, D02315, https://doi.org/10.1029/2003JD003792, 2004.

Konopka, P., Günther, G., McKenna, D. S., Müller, R., Offermann, D., Spang, R., and Riese, M.: How homogeneous and isotropic is stratospheric mixing? Comparison of CRISTA-1 observations with transport studies based on the Chemical Lagrangian Model of the Stratosphere (CLaMS), Q. J. R. Meteorol. Soc., 131, 565–579, https://doi.org/10.1256/qj.04.47, 2005.

Konopka, P., Günther, G., Müller, R., dos Santos, F. H. S., Schiller, C., Ravegnani, F., Ulanovsky, A., Schlager, H., Volk, C. M., Viciani, S., Pan, L. L., McKenna, D.-S., and Riese, M.: Contribution of mixing to upward transport across the tropical tropopause layer (TTL), Atmos. Chem. Phys., 7, 3285–3308, 2007.

Konopka, P., Ploeger, F., and Müller, R.: Entropy- and static stability-based Lagrangian model grids, in: Geophysical Monograph Series: Lagrangian Modeling of the Atmosphere, edited by Lin, J., vol. 200, pp. 99–109, American Geophysical Union, https://doi.org/10.1029/2012GM001253, 2012.

Kremser, S., Wohltmann, I., Rex, M., Langematz, U., Dameris, M., and Kunze, M.: Water vapour transport in the tropical tropopause region in coupled Chemistry-Climate Models and ERA-40 reanalysis data, Atmos. Chem. Phys., 9, 2679–2694, https://doi.org/10.5194/acp-9-2679-2009, 2009.

Kunz, A., Müller, R., Homonnai, V., Jánosi, I., Hurst, D., Rap, A., Forster, P., Rohrer, F., Spelten, N., and Riese, M.: Extending water vapor trend observations over Boulder into the tropopause region: trend uncertainties and resulting radiative forcing, J. Geophys. Res., 118, 11 269–11 284, https://doi.org/10.1002/jgrd.50831, 2013.

Kushner, P. J., Held, I. M., and Delworth, T. L.: Southern Hemisphere Atmospheric Circulation Response to Global Warming, J. Climate, 14, 2238–2249, https://doi.org/10.1175/1520-0442(2001)014<0001:SHACRT>2.0.CO;2, 2001.

Lau, K.-M. and Yang, S.: Tropical meteoroogy and climate | Walker Circulation, in: Encyclopedia of Atmospheric Sciences (Second Edition), edited by North, G. R., Pyle, J., and Zhang, F., pp. 177–181, Academic Press, Oxford, second edition edn., https://doi.org/10.1016/B978-0-12-382225-3.00450-3, 2015.

Laube, J. C., Engel, A., Bönisch, H., Möbius, T., Sturges, W. T., Braß, M., and Röckmann, T.: Fractional release factors of long-lived halogenated organic compounds in the tropical stratosphere, Atmospheric Chemistry and Physics, 10, 1093–1103, https://doi.org/10.5194/acp-10-1093-2010, 2010.

Laube, J. C., Keil, A., Bönisch, H., Engel, A., Röckmann, T., Volk, C. M., and Sturges, W. T.: Observation-based assessment of stratospheric fractional release, lifetimes, and ozone depletion potentials of ten important source gases, Atmos. Chem. Phys., 13, 2779–2791, https://doi.org/10.5194/acp-13-2779-2013, 2013.

LeTexier, H., Solomon, S., and Garcia, R. R.: The role of molecular hydrogen and methane oxidation in the water vapour budget of the stratosphere, Q. J. R. Meteorol. Soc., 114, 281–295, https://doi.org/10.1002/qj.49711448002, 1988.

Li, F., Austin, J., and Wilson, J.: The Strength of the Brewer-Dobson Circulation in a Changing Climate: Coupled Chemistry-Climate Model Simulations, J. Climate, 21, 40–57, https://doi.org/10.1175/2007JCLI1663.1, 2008.

Liu, S., Fueglistaler, S., and Haynes, P.: Advection–condensation paradigm for stratospheric water vapor, J. Geophys. Res., 115, D24307, https://doi.org/10.1029/2010JD014352, 2011.

Livesey, N. J., Read, W. G., Wagner, P. A., Froidevaux, L., Lambert, A., Manney, G. L., Valle, L. F. M., Pumphrey, H. C., Santee, M. L., Schwart, M. J., Wang, S., Fuller, R. A., Jarnot, R. F., Knosp, B. W., and Martinez, E.: Earth Observing System, Aura Microwave Limb Sounder (MLS): Version 4.2x Level 2 data quality and description document, Technical report, Jet Propulsion Laboratory, D-33509, 2017.

Lossow, S., Hurst, D. F., Rosenlof, K. H., Stiller, G. P., von Clarmann, T., Brinkop, S., Dameris, M., Jöckel, P., Kinnison, D. E., Plieninger, J., Plummer, D. A., Ploeger, F., Read, W. G., Remsberg, E. E., Russell, J. M., and Tao, M.: Trend differences in lower stratospheric water vapour between Boulder and the zonal mean and their role in understanding fundamental observational discrepancies, Atmos. Chem. Phys., 18, 8331–8351, https://doi.org/10.5194/acp-18-8331-2018, 2018.

Mahowald, N. M., Plumb, R. A., Rasch, P. J., del Corral, J., and Sassi, F.: Stratospheric transport in a three-dimensional isentropic coordinate model, J. Geophys. Res., 107, 4254, https://doi.org/10.1029/2001JD001313, 2002.

Manney, G. L. and Hegglin, M. I.: Seasonal and Regional Variations of Long-Term Changes in Upper-Tropospheric Jets from Reanalyses, J. Climate, 31, 423–448, https://doi.org/10.1175/JCLI-D-17-0303.1, 2018.

Manney, G. L., Hegglin, M. I., Lawrence, Z. D., Wargan, K., Millán, L. F., Schwartz, M. J., Santee, M. L., Lambert, A., Pawson, S., Knosp, B. W., Fuller, R. A., and Daffer, W. H.: Reanalysis comparisons of upper tropospheric–lower stratospheric jets and multiple tropopauses, Atmos. Chem. Phys., 17, 11 541–11 566, https://doi.org/10.5194/acp-17-11541-2017, 2017.

Marti, J. and Mauersberger, K.: A survey and new measurements of ice vapor pressure temperatures between 170 and 250 K, Geophys. Res. Lett., 20, 363–366, https://doi.org/10.1029/93GL00105, 1993.

Maycock, A. C., Shine, K. P., and Joshi, M. M.: The temperature response to stratospheric water vapour changes, Q. J. R. Meteorol. Soc., 137, 1070–1082, https://doi.org/10.1002/qj.822, 2011.

Maycock, A. C., Joshi, M. M., Shine, K. P., and Scaife, A. A.: The Circulation Response to Idealized Changes in Stratospheric Water Vapor, J. Climate, 26, 545–561, https://doi.org/10.1175/JCLI-D-12-00155.1, 2013.

McCormick, M. P.: Sage II: An overview, J. Adv. Space Res., 7, 219–226, https://doi.org/10.1016/0273-1177(87)90151-7, 1987.

McIntyre, M. E. and Norton, W. A.: Potential vorticity inversion on a hemisphere, J. Atmos. Sci., 57, 1214–1235, https://doi.org/10.1175/1520-0469(2000)057<1214:PVIOAH>2.0.CO;2, 2000.

McIntyre, M. E. and Palmer, T. N.: The "surf zone" in the stratosphere, J. Atmos. Terr. Phys., 46, 825–849, https://doi.org/10.1016/0021-9169(84)90063-1, 1984.

McKenna, D. S., Konopka, P., Grooß, J.-U., Günther, G., Müller, R., Spang, R., Offermann, D., and Orsolini, Y.: A new Chemical Lagrangian Model of the Stratosphere (CLaMS): 1. Formulation of advection and mixing, J. Geophys. Res., 107, 4309, https://doi.org/10.1029/2000JD000114, 2002a.

McKenna, D. S., Grooß, J.-U., Günther, G., Konopka, P., Müller, R., Carver, G., and Sasano, Y.: A new Chemical Lagrangian Model of the Stratosphere (CLaMS): 2. Formulation of chemistry scheme and initialization, J. Geophys. Res., 107, 4256, https://doi.org/10.1029/2000JD000113, 2002b.

Mote, P. W., Rosenlof, K. H., Holton, J. R., Harwood, R. S., and Waters, J. W.: Seasonal variations of water vapor in the tropical lower stratosphere, Geophys. Res. Lett., 22, 1093–1096, https://doi.org/10.1029/95GL01234, 1995.

Mote, P. W., Rosenlof, K. H., McIntyre, M. E., Carr, E. S., Gille, J. G., Holton, J. R., Kinnersley, J. S., Pumphrey, H. C., Russell III, J. M., and Waters, J. W.: An atmospheric tape recorder: The imprint of tropical tropopause temperatures on stratospheric water vapor, J. Geophys. Res., 101, 3989–4006, 1996.

Mote, P. W., Dunkerton, T. J., McIntyre, M. E., Ray, E. A., Haynes, P. H., and Russell III, J. M.: Vertical velocity, vertical diffusion, and dilution by midlatitude air in the tropical lower stratosphere, J. Geophys. Res., 103, 8651–8666, 1998.

Müller, R., Kunz, A., Hurst, D. F., Rolf, C., Krämer, M., and Riese, M.: The need for accurate long-term water vapor measurements in the upper troposphere and lower stratosphere with global coverage, Earth's Future, 4, 25–32, https://doi.org/10.1002/2015EF000321, 2016.

Müller, R., Grooß, J.-U., Zafar, A. M., Robrecht, S., and Lehmann, R.: The maintenance of elevated active chlorine levels in the Antarctic lower stratosphere through HCl null-cycles, Atmos. Chem. Phys., 18, 2985–2997, https://doi.org/10.5194/acp-18-2985-2018, 2018.

Murgatroyd, R. J. and Singleton, F.: Possible meridional circulations in the stratosphere and mesosphere, Q. J. R. Meteorol. Soc., 87, 125–135, https://doi.org/10.1002/qj.49708737202, 1961.

Neis, P., Smit, H. G. J., Krämer, M., Spelten, N., and Petzold, A.: Evaluation of the MOZAIC Capacitive Hygrometer during the airborne field study CIRRUS-III, Atmos. Meas. Tech., 8, 1233–1243, https://doi.org/10.5194/amt-8-1233-2015, 2015.

Neu, J. L. and Plumb, R. A.: Age of air in a “leaky pipe” model of stratospheric transport, J. Geophys. Res.-Atmos., 104, 19 243–19 255, https://doi.org/10.1029/1999JD900251, 1999.

Newell, R. E.: Transfer through the tropopause and within the stratosphere, Q. J. R. Meteorol. Soc., 89, 167–204, https://doi.org/10.1002/qj.49708938002, 1963.

Newman, P. A., Daniel, J. S., Waugh, D. W., and Nash, E. R.: A new formulation of equivalent effective stratospheric chlorine (EESC), Atmos. Chem. Phys., 7, 4537–4552, https://doi.org/10.5194/acp-7-4537-2007, 2007.

Norton, W.: Tropical wave driving of the annual cycle in tropical tropopause temperatures. Part II: Model results, J. Atmos. Sci., 63, 1420–1431, 2006.

Nowack, P. J., Luke, A. N., Maycock, A. C., Braesicke, P., Gregory, J. M., Joshi, M. M., Osprey, A., and Pyle, J. A.: A large ozone-circulation feedback and its implications for global warming assessments, Nat. Clim. Change, 5, 41–45, https://doi.org/10.1038/nclimate2451, 2015.

Nowack, P. J., Braesicke, P., Luke Abraham, N., and Pyle, J. A.: On the role of ozone feedback in the ENSO amplitude response under global warming, Geophys. Res. Lett., 44, 3858–3866, https://doi.org/10.1002/2016GL072418, 2017.

Oberländer-Hayn, S., Gerber, E. P., Abalichin, J., Akiyoshi, H., Kerschbaumer, A., Kubin, A., Kunze, M., Langematz, U., Meul, S., Michou, M., Morgenstern, O., and Oman, L. D.: Is the Brewer-Dobson circulation increasing or moving upward?, Geophys. Res. Lett., 43, 1772–1779, https://doi.org/10.1002/2015GL067545, 2016.

Oltmans, S. J. and Hofmann, D. J.: Increase in lower-stratospheric water vapor at a mid-latitude northern hemisphere site from 1981 to 1994, Nature, 374, 146–149, https://doi.org/10.1038/374146a010.1038/374146a0, 1995.

Orsolini, Y. J., Manney, G. L., Angel, A., Ovarlez, J., Claud, C., and Coy, L.: Layering in stratospheric profiles of long-lived trace species: Balloon-borne observations and modeling, J. Geophys. Res., 103, 5815–5825, https://doi.org/10.1029/97JD03131, 1998.

Ostermöller, J., Bönisch, H., Jöckel, P., and Engel, A.: A new time-independent formulation of fractional release, Atmos. Chem. Phys., 17, 3785–3797, https://doi.org/10.5194/acp-17-3785-2017, 2017.

Palchetti, L., Bianchini, G., Carli, B., Cortesi, U., and Del Bianco, S.: Measurement of the water vapour vertical profile and of the Earth’s outgoing far infrared flux, Atmos. Chem. Phys., 8, 2885–2894, https://doi.org/10.5194/acp-8-2885-2008, 2008.

Pan, L. L., Solomon, S., Randel, W., Lamarque, J.-F., Hess, P., Gille, J., Chiou, E.-W., and McCormick, M. P.: Hemispheric asymmetries and seasonal variations of the lowermost stratospheric water vapor and ozone derived from SAGE II data, J. Geophys. Res., 102, https://doi.org/10.1029/97JD02778, 1997.

Pawson, S., Kodera, K., Hamilton, K., Shepherd, T. G., Beagley, S. R., Boville, B. A., Farrara, J. D., Fairlie, T. D. A., Kitoh, A., Lahoz, W. A., Langematz, U., Manzini, E., Rind, D. H., Scaife, A. A., Shibata, K., Simon, P., Swinbank, R., Takacs, L., Wilson, R. J., Al-Saadi, J. A., Amodei, M., Chiba, M., Coy, L., de GrandprÃl', J., Eckman, R. S., Fiorino, M., Grose, W. L., Koide, H., Koshyk, J. N., Li, D., Lerner, J., Mahlman, J. D., McFarlane, N. A., Mechoso, C. R., Molod, A., O’Neill, A., Pierce, R. B., Randel, W. J., Rood, R. B., and Wu, F.: The GCM-Reality Intercomparison Project for SPARC

(GRIPS): Scientific Issues and Initial Results, Bull. Am. Meteorol. Soc., 81, 781–796, https://doi.org/10.1175/1520-0477(2000)081<0781:TGIPFS>2.3.CO;2, 2000.

Pierrehumbert, R. T. and Rocca, R.: Evidence for control of Atlantic subtropical humidity by large scale advection, Geophys. Res. Lett., 25, 4537–4540, https://doi.org/10.1029/1998GL900203, 1998.

Platzman, G. W.: The Rossby wave, Q. J. R. Meteorol. Soc., 94, 225–248, https://doi.org/10.1002/qj.49709440102, 1968.

Ploeger, F. and Birner, T.: Seasonal and inter-annual variability of lower stratospheric age of air spectra, Atmos. Chem. Phys., 16, 10 195–10 213, https://doi.org/10.5194/acp-16-10195-2016, 2016.

Ploeger, F., Konopka, P., Günther, G., Grooß, J.-U., and Müller, R.: Impact of the vertical velocity scheme on modeling transport across the tropical tropopause layer, J. Geophys. Res., 115, D03301, https://doi.org/10.1029/2009JD012023, 2010.

Ploeger, F., Konopka, P., Müller, R., Fueglistaler, S., Schmidt, T., Manners, J. C., Grooß, J.-U., Günther, G., Forster, P. M., and Riese, M.: Horizontal transport affecting trace gas seasonality in the Tropical Tropopause Layer (TTL), J. Geophys. Res., 117, D09303, https://doi.org/10.1029/2011JD017267, 2012.

Ploeger, F., Günther, G., Konopka, P., Fueglistaler, S., Müller, R., Hoppe, C., Kunz, A., Spang, R., Grooß, J.-U., and Riese, M.: Horizontal water vapor transport in the lower stratosphere from subtropics to high latitudes during boreal summer, J. Geophys. Res., 118, 8111–8127, https://doi.org/10.1002/jgrd.50636, 2013.

Ploeger, F., Abalos, M., Birner, T., Konopka, P., Legras, B., Müller, R., and Riese, M.: Quantifying the effects of mixing and residual circulation on trends of stratospheric mean age of air, Geophys. Res. Lett., 42, 2047–2054, https://doi.org/10.1002/2014GL062927, 2015a.

Ploeger, F., Riese, M., Haenel, F., Konopka, P., Müller, R., and Stiller, G.: Variability of stratospheric mean age of air and of the local effects of residual circulation and eddy mixing, J. Geophys. Res., 120, 716–733, https://doi.org/10.1002/2014JD022468, 2015b.

Plumb, R. A.: A "tropical pipe" model of stratospheric transport, J. Geophys. Res.-Atmos., 101, 3957–3972, https://doi.org/10.1029/95JD03002, 1996.

Plumb, R. A.: Stratospheric transport, J. Meteorol. Soc. Japan. Ser. II, 80, 793–809, https://doi.org/10.2151/jmsj.80.793, 2002.

Plumb, R. A. and Ko, M. K. W.: Interrelationships between mixing ratios of long-lived stratospheric constituents, J. Geophys. Res., 97, 10 145–10 156, https://doi.org/10.1029/92JD00450, 1992.

Podglajen, A. and Ploeger, F.: Retrieving the age of air spectrum from tracers: principle and method, Atmos. Chem. Phys., 19, 1767–1783, https://doi.org/10.5194/acp-19-1767-2019, 2019.

Podglajen, A., Bui, T. P., Dean-Day, J. M., Pfister, L., Jensen, E. J., Alexander, M. J., Hertzog, A., Kärcher, B., Plougonven, R., and Randel, W. J.: Small-Scale Wind Fluctuations in the Tropical Tropopause Layer from Aircraft Measurements: Occurrence, Nature, and Impact on Vertical Mixing, J. Atmos. Sci., 74, 3847–3869, https://doi.org/10.1175/JAS-D-17-0010.1, 2017.

Pommrich, R., Müller, R., Grooß, J.-U., Konopka, P., Ploeger, F., Vogel, B., Tao, M., Hoppe, C. M., Günther, G., Spelten, N., Hoffmann, L., Pumphrey, H.-C., Viciani, S., D'Amato, F., Volk, C. M., Hoor, P., Schlager, H., and Riese, M.: Tropical troposphere to stratosphere transport of carbon monoxide and long-lived trace species in the Chemical Lagrangian Model of the Stratosphere (CLaMS), Geosci. Model Dev., 7, 2895–2916, https://doi.org/10.5194/gmd-7-2895-2014, 2014.

Poshyvailo, L., Müller, R., Konopka, P., Günther, G., Riese, M., Podglajen, A., and Ploeger, F.: Sensitivities of modelled water vapour in the lower stratosphere: temperature uncertainty, effects of horizontal transport and small-scale mixing, Atmos. Chem. Phys., 18, 8505–8527, https://doi.org/10.5194/acp-18-8505-2018, 2018.

Ramanathan, V., Cicerone, R. J., Singh, H. B., and Kiehl, J. T.: Trace gas trends and their potential role in climate change, J. Geophys. Res.-Atmos., 90, 5547–5566, https://doi.org/10.1029/JD090iD03p05547, 1985.

Randel, W. and Jensen, E.: Physical processes in the tropical tropopause layer and their role in a changing climate, Nat. Geosci., 6, 169–176, https://doi.org/10.1038/ngeo1733, 2013.

Randel, W. J. and Park, M.: Deep convective influence on the Asian summer monsoon anticyclone and associated tracer variability observed with Atmospheric Infrared Sounder (AIRS), J. Geophys. Res., 111, D12314, https://doi.org/10.1029/2005JD006490, 2006.

Randel, W. J. and Park, M.: Diagnosing Observed Stratospheric Water Vapor Relationships to the Cold Point Tropical Tropopause, J. Geophys. Res.-Atmos., 124, 7018–7033, https://doi.org/10.1029/2019JD030648, 2019.

Randel, W. J., Wu, F., Russell, J. M., Roche, A., and Waters, J. W.: Seasonal cycles and QBO variations in stratospheric CH_4 and H_2O observed in UARS HALOE data, J. Atmos. Sci., 55, 163–185, 1998.

Randel, W. J., Wu, F., Gettelman, A., Russell, J., Zawodny, J., and Oltmans, S.: Seasonal variation of water vapor in the lower stratosphere observed in Halogen Occultation Experiment data, J. Geophys. Res., 106, 14 313–14 325, https://doi.org/10.1029/2001JD900048, 2001.

Randel, W. J., Wu, F., Vömel, H., Nedoluha, G. E., and Forster, P.: Decreases in stratospheric water vapor after 2001: Links to changes in the tropical tropopause and the Brewer-Dobson circulation, J. Geophys. Res.-Atmos., 111, D12312, https://doi.org/10.1029/2005JD006744, 2006.

Raspollini, P., Belotti, C., Burgess, A., Carli, B., Carlotti, M., Ceccherini, S., Dinelli, B. M., Dudhia, A., Flaud, J.-M., Funke, B., Höpfner, M., López-Puertas, M., Payne, V., Piccolo, C., Remedios, J. J., Ridolfi, M., and Spang, R.: MIPAS level 2 operational analysis, Atmos. Chem. Phys., 6, 5605–5630, https://doi.org/10.5194/acp-6-5605-2006, 2006.

Ray, E. A., Moore, F. L., Rosenlof, K. H., Davis, S. M., Boenisch, H., Morgenstern, O., Smale, D., Rozanov, E., Hegglin, M., Pitari, G., Mancini, E., Braesicke, P., Butchart, N., Hardiman, S., Li, F., Shibata, K., and Plummer, D. A.: Evidence for changes in stratospheric transport and mixing over the past three decades based on multiple data sets and tropical leaky pipe analysis, J. Geophys. Res., 115, https://doi.org/10.1029/2010JD014206, 2010.

Ray, E. A., Moore, F. L., Rosenlof, K. H., Davis, S. M., Sweeney, C., Tans, P., Wang, T., Elkins, J. W., Boenisch, H., Engel, A., Sugawara, S., Nakazawa, T., and Aoki, S.: Improving stratospheric transport trend analysis based on SF_6 and CO_2 measurements, J. Geophys. Res., 119, 14 110–14 128, 2014.

Remsberg, E. E.: Methane as a diagnostic tracer of changes in the Brewer-Dobson circulation of the stratosphere, Atmos. Chem. Phys., 15, 3739–3754, https://doi.org/10.5194/acp-15-3739-2015, 2015.

Riese, M., Ploeger, F., Rap, A., Vogel, B., Konopka, P., Dameris, M., and Forster, P.: Impact of uncertainties in atmospheric mixing on simulated UTLS composition and related radiative effects, J. Geophys. Res., 117, D16305, https://doi.org/10.1029/2012JD017751, 2012.

Rind, D., Chiou, E.-W., Chu, W., Oltmans, S., Lerner, J., Larsen, J., McCormick, M. P., and McMaster, L.: Overview of the Stratospheric Aerosol and Gas Experiment II water vapor observations: Method, validation, and data characteristics, J. Geophys. Res.-Atmos., 98, 4835–4856, https://doi.org/10.1029/92JD01174, 1993.

Röckmann, T., Grooß, J.-U., and Müller, R.: The impact of anthropogenic chlorine emissions, stratospheric ozone change and chemical feedbacks on stratospheric water, Atmos. Chem. Phys., 4, 693–699, https://doi.org/10.5194/acp-4-693-2004, 2004.

Rodgers, C. D.: Inverse methods for atmospheric sounding: theory and practice, vol. 2 of *Series on atmospheric, oceanic and planetary physics*, World Scientific, Singapore, 2000.

Rohs, S., Schiller, C., Riese, M., Engel, A., Schmidt, U., Wetter, T., Levin, I., Nakazawa, T., and Aoki, S.: Long-term changes of methane and hydrogen in the stratosphere in the period 1978-2003 and their impact on the abundance of stratospheric water vapor, J. Geophys. Res., 111, D14315, https://doi.org/10.1029/2005JD006877, 2006.

Rolf, C., Vogel, B., Hoor, P., Afchine, A., Günther, G., Krämer, M., Müller, R., Müller, S., Spelten, N., and Riese, M.: Water vapor increase in the lower stratosphere of the Northern Hemisphere due to the Asian monsoon anticyclone observed during the TACTS/ESMVal campaigns, Atmos. Chem. Phys., 18, 2973–2983, https://doi.org/10.5194/acp-18-2973-2018, 2018.

Rollins, A. W., Thornberry, T. D., Gao, R. S., Smith, J. B., Sayres, D. S., Sargent, M. R., Schiller, C., Krämer, M., Spelten, N., Hurst, D. F., Jordan, A. F., Hall, E. G., VÃűmel, H., Diskin, G. S., Podolske, J. R., Christensen, L. E., Rosenlof, K. H., Jensen, E. J., and Fahey, D. W.: Evaluation of UT/LS hygrometer accuracy by intercomparison during the NASA MACPEX mission, J. Geophys. Res.-Atmos., 119, 1915–1935, https://doi.org/10.1002/2013JD020817, 2014.

Rosenlof, K., Oltmans, S., Kley, D., Russell, J., Chiou, E.-W., Chu, W., Johnson, D., Kelly, K., Michelsen, H., Nedoluha, G., et al.: Stratospheric water vapor increases over the past half-century, Geophys. Res. Lett., 28, 1195–1198, https://doi.org/10.1029/2000GL012502, 2001.

Rosenlof, K. H.: Seasonal cycle of the residual mean meridional circulation in the stratosphere, J. Geophys. Res.-Atmos., 100, 5173 – 5191, https://doi.org/10.1029/94JD03122, 1995.

Rosenlof, K. H. and Reid, G. C.: Trends in the temperature and water vapor content of the tropical lower stratosphere: Sea surface connection, jgr, 113, https://doi.org/10.1029/2007JD009109, 2008.

Rosenlof, K. H., Tuck, A. F., Kelly, K. K., Russell III, J. M., and McCormick, M. P.: Hemispheric asymmetries in the water vapor and inferences about transport in the lower stratosphere, J. Geophys. Res., 102, 13 213–13 234, https://doi.org/{10.1029/97JD00873}, 1997.

Rossby, C. G.: Relation between variations in the intensity of the zonal circulation of the atmosphere and the displacements of the semipermanent centers of action, Journal of the Marine Research, 2, 38–55, 1939.

Röth, E.-P. and Ehhalt, D. H.: A simple formulation of the CH_2O photolysis quantum yields, Atmos. Chem. Phys., 15, 7195–7202, https://doi.org/10.5194/acp-15-7195-2015, 2015.

Roulleau, M. and Poc, M. M.: A Frost-Point Hygrometer for Horizontal Soundings of the Lower Stratosphere, J. Appl. Meteorol., 17, 803–811, https://doi.org/10.1175/1520-0450(1978)017<0803:AFPHFH>2.0.CO;2, 1978.

Russell III, J. M.: Overview of the halogen occultation experiment, in: Remote Sensing of Atmospheric Chemistry, vol. 1491, pp. 110–116, International Society for Optics and Photonics, 1991.

Russell III, J. M., Gordley, L. L., Park, J. H., Drayson, S. R., Hesketh, W. D., Cicerone, R. J., Tuck, A. F., Frederick, J. E., Harries, J. E., and Crutzen, P. J.: The Halogen Occultation Experiment, J. Geophys. Res., 98, 10 777–10 797, https://doi.org/10.1029/93JD00799, 1993.

Russo, M. R., Marecal, V., C. R. Hoyle and, J. A., Chemel, C., Chipperfield, M. P., Dessens, O., Feng, W., Hosking, J. S., Telford, P. J., Wild, O., Yang, X., , and Pyle, J. A.: Representation of tropical deep convection in atmospheric models (Part 1): Meteorology and comparison with satellite observations, Atmos. Chem. Phys., 11, 2765–2786, 2011.

Salby, M. L.: Fundamentals of Atmospheric Physics, International Geophysics, Academic Press, 1996.

Samadi, s., Sagareswar, G., and Tajiki, M.: Comparison of General Circulation Models: methodology for selecting the best GCM in Kermanshah Synoptic Station, Iran, Int. J. of Global Warming, 2, 347–365, 2010.

Schiller, C., Grooß, J.-U., Konopka, P., Plöger, F., Silva dos Santos, F. H., and Spelten, N.: Hydration and dehydration at the tropical tropopause, Atmos. Chem. Phys., 9, 9647–9660, https://doi.org/10.5194/acp-9-9647-2009, 2009.

Schlager, H., Grewe, V., and Roiger, A.: Chemical Composition of the Atmosphere, in: Atmospheric Physics: Background - Methods - Trends, pp. 17–35, Springer, https://doi.org/10.1007/978-3-642-30183-4_2, 2012.

Schoeberl, M. R.: Extratropical stratosphere-troposphere mass exchange, J. Geophys. Res.-Atmos., 109, https://doi.org/10.1029/2004JD004525, 2004.

Schoeberl, M. R. and Dessler, A. E.: Dehydration of the stratosphere, Atmos. Chem. and Phys., 11, 8433–8446, https://doi.org/10.5194/acp-11-8433-2011, 2011.

Schoeberl, M. R., Sparling, L. C., Jackman, C. H., and Fleming, E. L.: A Lagrangian view of stratospheric trace gas distributions, J. Geophys. Res., 105, 1537–1552, https://doi.org/10.1029/1999JD900787, 2000.

Schoeberl, M. R., Douglass, A. R., Polansky, B., Boone, C., Walker, K. A., and Bernath, P.: Estimation of stratospheric age spectrum from chemical tracers, J. Geophys. Res.-Atmos., 110, https://doi.org/10.1029/2005JD006125, 2005.

Schoeberl, M. R., Dessler, A. E., and Wang, T.: Modeling upper tropospheric and lower stratospheric water vapor anomalies, Atmos. Chem. Phys., 13, 7783–7793, https://doi.org/10.5194/acp-13-7783-2013, 2013.

Schoeberl, M. R., Dessler, A. E., Wang, T., Avery, M. A., and Jensen, E. J.: Cloud formation, convection, and stratospheric dehydration, Earth Space Sci., 1, 1–17, https://doi.org/10.1002/2014EA000014, 2014.

Schumann, U.: Atmospheric Physics: Background – Methods – Trends, Research Topics in Aerospace, Springer Berlin Heidelberg, 2012.

Seviour, W. J. M., Butchart, N., and Hardiman, S. C.: The Brewer-Dobson circulation inferred form ERA-Interim, Q. J. R. Meteorol. Soc., 138, 878–888, https://doi.org/10.1002/qj.966, 2012.

Sherwood, S. C., Roca, R., Weckwerth, T. M., and Andronova, N. G.: Tropospheric water vapor, convection, and climate, Rev. Geophys., 48, RG2001, https://doi.org/10.1029/2009RG000301, 2010.

Shindell, D. T.: Climate and ozone response to increased stratospheric water vapor, Geophys. Res. Lett., 28, 1551–1554, https://doi.org/10.1029/1999GL011197, 2001.

Sigmond, M., Siegmund, P. C., Manzini, E., and Kelder, H.: A Simulation of the Separate Climate Effects of Middle-Atmospheric and Tropospheric CO2 Doubling, J. Climate, 17, 2352–2367, https://doi.org/10.1175/1520-0442(2004)017<2352:ASOTSC>2.0.CO;2, 2004.

Smith, J.: Chemistry of the atmosphere | Observations for Chemistry (In Situ): Water Vapor Sondes, in: Encyclopedia of Atmospheric Sciences (Second Edition), edited by North, G. R., Pyle, J., and Zhang, F., pp. 387–400, Academic Press, Oxford, second edition edn., https://doi.org/https://doi.org/10.1016/B978-0-12-382225-3.00268-1, 2015.

Solomon, S. and Albritton, D. L.: Time-dependent ozone depletion potentials for short- and long-term forecasts, Nature, 357, 33–37, https://doi.org/10.1038/357033a0, 1992.

Solomon, S., Rosenlof, K., Portmann, R., Daniel, J., Davis, S., Sanford, T., and Plattner, G.-K.: Contributions of stratospheric water vapor to decadal changes in the rate of global warming, Science, 327, 1219–1223, https://doi.org/10.1126/science.1182488, 2010.

Solomon, S., Daniel, J. S., Neely, R. R., Vernier, J.-P., Dutton, E. G., and Thomason, L. W.: The Persistently Variable "Background" Stratospheric Aerosol Layer and Global Climate Change, Science, 333, 866–870, https://doi.org/10.1126/science.1206027, 2011.

Stenke, A., Dameris, M., Grewe, V., and Garny, H.: Implications of Lagrangian transport for coupled chemistry-climate simulations, Atmos. Chem. Phys., 9, 5489–5504, https://doi.org/10.5194/acp-9-5489-2009, 2008.

Stiller, G. P., von Clarmann, T., Haenel, F., Funke, B., Glatthor, N., Grabowski, U., Kellmann, S., Kiefer, M., Linden, A., Lossow, S., and López-Puertas, M.: Observed temporal evolution of global mean age of stratospheric air for the 2002 to 2010 period, Atmos. Chem. Phys., 12, 3311–3331, https://doi.org/10.5194/acp-12-3311-2012, 2012.

Stocker, T. F., Qin, D., Plattner, G.-K., Tignor, M., Allen, S. K., Boschung, J., Nauels, A., Xia, Y., Bex, V., and Midgley, P. M., eds.: Climate Change 2013: The Physical Science Basis. Contribution of Working Group I to the Fifth Assessment Report of the Intergovernmental Panel on Climate Change, Cambridge University Press, Cambridge, UK and New York, NY, USA, 2013.

Strunk, M., Engel, A., Schmidt, U., Volk, C. M., Wetter, T., Levin, I., and Glatzel-Mattheier, H.: CO2 and SF6 as sratospheric age trancers: consistency and the effect of mesospheric SF6 - loss, Geophys. Res. Lett., 27, 341–344, https://doi.org/10.1029/1999GL011044, 2000.

Tao, M., Konopka, P., Ploeger, F., Riese, M., Müller, R., and Volk, C.: Impact of stratospheric major warmings and the quasi-biennial oscillation on the variability of stratospheric water vapor, Geophys. Res. Lett., 42, 4599–4607, https://doi.org/10.1002/2015GL064443, 2015.

Thomason, L. W., Poole, L. R., and Deshler, T.: A global climatoloy of stratospheric aerosol surface area density deduced from Stratospheric Aerosol and Gas Experiment II measurements: 1984-1994, J. Geophys. Res., 102, 8967–8976, https://doi.org/10.1029/96JD02962, 1997.

Tompkins, A. M., Gierens, K., and Rädel, G.: Ice supersaturation in the ECMWF Integrated Forecast System., Q. J. R. Meteorol. Soc., 133, 53–63, https://doi.org/10.1002/qj.14, 2007.

Ueyama, R., Jensen, E. J., Pfister, L., Diskin, G. S., Bui, T. P., and Dean-Day, J. M.: Dehydration in the tropical tropopause layer: A case study for model evaluation using aircraft observations, J. Geophys. Res.-Atmos., 119, 5299–5316, https://doi.org/10.1002/2013JD021381, 2014.

Ueyama, R., Jensen, E. J., Pfister, L., and Kim, J.-E.: Dynamical, convective, and microphysical control on wintertime distributions of water vapor and clouds in the tropical tropopause layer, J. Geophys. Res.-Atmos., 120, 10 483–10 500, https://doi.org/10.1002/2015JD023318, 2015.

Viggiano, A. A.: In situ mass spectrometry and ion chemistry in the stratosphere and troposphere, Mass Spectrometry Reviews, 12, 115–137, https://doi.org/10.1002/mas.1280120203, 1993.

Vogel, B., Günther, G., Müller, R., Grooß, J.-U., Afchine, A., Bozem, H., Hoor, P., Krämer, M., Müller, S., Riese, M., Rolf, C., Spelten, N., Stiller, G. P., Ungermann, J., and Zahn, A.: Long-range transport pathways of tropospheric source gases originating in Asia into the northern lower stratosphere during the Asian monsoon season 2012, Atmos. Chem. Phys., 16, 15 301–15 325, https://doi.org/10.5194/acp-16-15301-2016, 2016.

Volk, C. M., Elkins, J. W., Fahey, D. W., Salawitch, R. J., Dutton, G. S., Gilligan, J. M., Proffitt, M. H., Loewenstein, M., Podolske, J. R., Minschwaner, K., Margitan, J. J., and Chan, K. R.: Quantifying transport between the tropical and mid-latitude lower stratosphere, Science, 272, 1763–1768, https://doi.org/10.1126/science.272.5269.1763, 1996.

Volk, C. M., Elkins, J. W., Fahey, D. W., Dutton, G. S., Gilligan, J. M., Loewenstein, M., Podolske, J. R., Chan, K. R., and Gunson, M. R.: Evaluation of source gas lifetimes from stratospheric observations, J. Geophys. Res.-Atmos., 102, 25 543–25 564, https://doi.org/10.1029/97JD02215, 1997.

von Clarmann, T. and Stiller, G.: Das Michelson Interferometer für Passive Atmosphärische Sondierung (MIPAS) auf dem Umweltforschungssarelliten ENVISAT, Nachrichten, Institut für Meteorologie und Klimaforschung AtmosphärischeSpurenstoffe und Fernerkundung am Forschungszentrum Karlsruhe, 2003.

Šácha, P., Eichinger, R., Garny, H., Pišoft, P., Dietmüller, S., de la Torre, L., Plummer, D. A., Jöckel, P., Morgenstern, O., Zeng, G., Butchart, N., and Añel, J. A.: Extratropical age of air trends and causative factors in climate projection simulations, Atmos. Chem. Phys., 19, 7627–7647, https://doi.org/10.5194/acp-19-7627-2019, 2019.

Wallace, J. and Hobbs, P.: Atmospheric Science: An Introductory Survey, International Geophysics, Elsevier Science, 2006.

Wang, T., Dessler, A. E., Schoeberl, M. R., Randel, W. J., and Kim, J.-E.: The impact of temperature vertical structure on trajectory modeling of stratospheric water vapor, Atmos. Chem. Phys., 15, 3517–3526, https://doi.org/10.5194/acp-15-3517-2015, 2015.

Waters, J., Froidevaux, L., Jarnot, R., Read, W., Pickett, H., Harwood, R., Cofield, R., Filipiak, M., Flower, D., Livesey, N., Manney, G., Pumphrey, H., Santee, M., Siegel, P., and Wu, D.: Earth Observing System (EOS) Microwave Limb Sounder (MLS). An overview of the EOS MLS experiment, Technical report, Jet Propulsion Laboratory, D-15745, 2004.

Waters, J. W., Read, W. G., Froidevaux, L., Jarnot, R. F., Cofield, R. E., Flower, D. A., Lau, G. K., Pickett, H. M., Santee, M. L., Wu, D. L., Boyles, M. A., Burke, J. R., Lay, R. R., Loo, M. S., Livesey, N. J., Lungu, T. A., Manney, G. L., Nakamura, L. L., Perun, V. S., Ridenoure, B. P., Shippony, Z., Siegel, P. H., Thurstans, R. P., Harwood, R. S., Pumphrey, H. C., and Filipiak, M. J.: The UARS and EOS Microwave Limb Sounder (MLS) Experiments, J. Atmos. Sci., 56, 194–218, https://doi.org/10.1175/1520-0469(1999)056<0194:TUAEML>2.0.CO;2, 1999.

Waters, J. W., Froidevaux, L., Harwood, R. S., Jarnot, R. F., Pickett, H. M., Read, W. G., Siegel, P. H., Cofield, R. E., Filipiak, M. J., Flower, D. A., Holden, J. R., Lau, G. K., Livesey, N. J., Manney, G. L., Pumphrey, H. C., Santee, M. L., Wu, D. L., Cuddy, D. T., Lay, R. R., Loo, M. S., Perun, V. S., Schwartz, M. J., Stek, P. C., Thurstans, R. P., Boyles, M. A., Chandra, S., Chavez, M. C., Chen, G.-S., Chudasama, B. V., Dodge, R., Fuller, R. A., Girard, M. A., Jiang, J. H., Jiang, Y., Knosp, B. W., LaBelle, R. C., Lam, J. C., Lee, K. A., Miller, D., Oswald, J. E., Patel, N. C., Pukala, D. M., Quintero, O., Scaff, D. M., Snyder, W. V., Tope, M. C., Wagner, P. A., and Walch, M. J.: The Earth Observing System Microwave Limb Sounder (EOS MLS) on the Aura satellite, IEEE Trans. Geosci. Remote Sens., 44, 1075–1092, 2006.

Waugh, D. W. and Hall, T. M.: Age of stratospheric air: theory, observations, and models, Rev. Geophys., 40, 1–27, https://doi.org/10.1029/2000RG000101, 2002.

Webster, C. R., May, R. D., Trimble, C. A., Chave, R. G., and Kendall, J.: Aircraft (ER-2)laser infrared absorption spectrometer (ALIAS) for in situ atmospheric measurements of HCl, N_2O, CH_4, NO_2, and HNO_3, Appl. Opt., 33, 454–472, https://doi.org/10.1364/AO.33.000454, 1994.

Weinstock, E. M., Smith, J. B., Sayres, D. S., Pittman, J. V., Spackman, J. R., Hintsa, E. J., Hanisco, T. F., Moyer, E. J., St. Clair, J. M., Sargent, M. R., and Anderson, J. G.: Validation of the Harvard Lyman-Îś in situ water vapor instrument: Implications for the mechanisms that control stratospheric water vapor, J. Geophys. Res.-Atmos., 114, https://doi.org/10.1029/2009JD012427, 2009.

Willett, H. C. and Sanders, F.: Chapter II - Adiabatic Processes and the Vertical Stability of the Atmosphere, in: Descriptive Meteorology (Second Edition), edited by Willett, H. C. and Sanders, F., pp. 14–37, Academic Press, second edition edn., https://doi.org/https://doi.org/10.1016/B978-1-4832-3165-5.50006-7, 1959.

WMO: Scientific assessment of ozone depletion: 2018, Global Ozone Research and Monitoring Project – Report No. 58, Geneva, Switzerland, 2018.

Wright, J. S., Fu, R., Fueglistaler, S., Liu, Y. S., and Zhang, Y.: The influence of summertime convection over Southeast Asia on water vapor in the tropical stratosphere, J. Geophys. Res., 116, D12302, https://doi.org/10.1029/2010JD015416, 2011.

Yano, J.-I. and Plant, R.: Interactions between Shallow and Deep Convection under a Finite Departure from Convective Quasi Equilibrium, J. Atmos. Sci., 69, 3463–3470, https://doi.org/10.1175/JAS-D-12-0108.1, 2012.

Yin, J. H.: A consistent poleward shift of the storm tracks in simulations of 21st century climate, Geophys. Res. Lett., 32, https://doi.org/10.1029/2005GL023684, 2005.

Zöger, M., Afchine, A., Eicke, N., Gerhards, M.-T., Klein, E., McKenna, D. S., Mörschel, U., Schmidt, U., Tan, V., Tuitjer, F., Woyke, T., and Schiller, C.: Fast in situ hygrometers: A new family of balloon-borne and airborne Lyman-α photofragment fluorescence hygrometers, J. Geophys. Res.-Atmos., 104, 1807–1816, https://doi.org/10.1029/1998JD100025, 1999.

Afterword

If I would have known how much effort is needed to complete a Ph.D., I most probably would have never started mine! Very often, we are already scared beforehand, and we end up never doing what we actually want. Because others told us so, especially when it comes from a figure of authority... I was dreaming about a Ph.D. since my childhood, and I am very thankful that one more wish became true in my life!

Thus, if you have a dream: follow it – without caring much about the obstacles you might stumble upon on your way. During your Ph.D., you can think that it is too hard, sometimes even boring, and, maybe, that is not your path, to become a scientist. But when you ask yourself whether you want to deal with Science, and if at least the smallest part of you answers “yes”... Follow it!

Science is the greatest achievement of mankind; it opens our eyes, from day to day, to a lot of things about the world where we live. If you have a curious personality with some creativity, you will always find your own niche in Science. And even if you do not find it right away, you can always create your own!

To do a Ph.D. – not the easiest way to go, but, on the other hand, it is definitely the way to grow! It is a huge work on yourself, including struggling and excitement, disappointment and joy. A Ph.D. is a path to get to know yourself better, and to understand your true wishes, and, at the same time, to contribute to global scientific development. Maybe it is not your highest mountain yet, and your highest Everest is still far ahead, you will definitely be proud of yourself after finishing your Ph.D

Band / Volume 490
Micromechanical Characterization of Ceramic Solid Electrolytes for Electrochemical Storage Devices
J. F. Nonemacher (2020), xv, 131 pp
ISBN: 978-3-95806-461-4

Band / Volume 491
Nanoscale investigation of high temperature oxidation mechanisms of high-Cr ferritic steels
A. Vayyala (2020), xix, 105 pp
ISBN: 978-3-95806-467-6

Band / Volume 492
Electrolyte development for a SOFC operating at low temperature
J. Zhang (2020), vi, 121 pp
ISBN: 978-3-95806-471-3

Band / Volume 493
Modeling and Simulation of Polymer Electrolyte Fuel Cells
S. Zhang (2020), 4, xii, 214 pp
ISBN: 978-3-95806-472-0

Band / Volume 494
Ab initio perspective on hydrogenated amorphous silicon for thin-film and heterojunction photovoltaics
P. Czaja (2020), 107 pp
ISBN: 978-3-95806-474-4

Band / Volume 495
Measurements of Atmospheric OH and HO_2 Radicals by Laser-Induced Fluorescence on the HALO Aircraft during the OMO-ASIA 2015 Campaign
C. Künstler (2020), 156 pp
ISBN: 978-3-95806-477-5

Band / Volume 496
Tomographic observations of gravity waves with the infrared limb imager GLORIA
I. Krisch (2020), vii, 187 pp
ISBN: 978-3-95806-481-2

Band / Volume 497
Aquisition of temporally and spatially highly resolved data sets of relevant trace substances for model development and model evaluation purposes using a mobile measuring laboratory
D. Klemp, R. Wegener, R. Dubus, U. Javed (2020), 110 pp
ISBN: 978-3-95806-465-2

Band / Volume 498
Charakterisierung des Werkstoffverhaltens während des Kosinterns einer neuartigen, inert gestützten Festoxidbrennstoffzelle
F. Grimm (2020), ix, 168 pp
ISBN: 978-3-95806-482-9

Band / Volume 499
WEGE FÜR DIE ENERGIEWENDE
Kosteneffiziente und klimagerechte Transformationsstrategien für das deutsche Energiesystem bis zum Jahr 2050
M. Robinius et al (2020), VIII, 141 pp
ISBN: 978-3-95806-483-6

Band / Volume 500
Mechanical Behavior of Solid Electrolyte Materials for Lithium-ion Batteries
G. Yan (2020), x, 139 pp
ISBN: 978-3-95806-484-3

Band / Volume 501
Retrieval of atmospheric quantities from remote sensing measurements of nightglow emissions in the MLT region
Q. Chen (2020), 208 pp
ISBN: 978-3-95806-485-0

Band / Volume 502
Auswirkungen der Energiewende auf das deutsche Gastransportsystem
B. Gillessen (2020), XVII, 186
ISBN: 978-3-95806-487-4

Band / Volume 503
Lagrangian Simulation of Stratospheric Water Vapour: Impact of Large-Scale Circulation and Small-Scale Transport Processes
L. Poshyvailo (2020), 126 pp
ISBN: 978-3-95806-488-1

Energie & Umwelt / Energy & Environment
Band / Volume 503
ISBN 978-3-95806-488-1

Mitglied der Helmholtz-Gemeinschaft

JÜLICH
Forschungszentrum